

UNIVERSITÉ DU QUÉBEC EN ABITIBI-TEMISCAMINGUE

CARACTÉRISATION DU BRUIT ÉLECTROMAGNÉTIQUE DANS LES
TUNNELS MINIERS PROFONDS ET APPLICATION DE LA MÉTHODE DE
DÉBRUITAGE

THÈSE
PRESENTÉE
COMME EXIGENCE PARTIELLE
DU DOCTORAT EN SCIENCES DE L'ENVIRONNEMENT

PAR
XUEPING DAI

MARS 2019



BIBLIOTHÈQUE

Cégep de l'Abitibi-Témiscamingue
Université du Québec en Abitibi-Témiscamingue

Mise en garde

La bibliothèque du Cégep de l'Abitibi-Témiscamingue et de l'Université du Québec en Abitibi-Témiscamingue a obtenu l'autorisation de l'auteur de ce document afin de diffuser, dans un but non lucratif, une copie de son œuvre dans Depositum, site d'archives numériques, gratuit et accessible à tous.

L'auteur conserve néanmoins ses droits de propriété intellectuelle, dont son droit d'auteur, sur cette œuvre. Il est donc interdit de reproduire ou de publier en totalité ou en partie ce document sans l'autorisation de l'auteur.

Warning

The library of the Cégep de l'Abitibi-Témiscamingue and the Université du Québec en Abitibi-Témiscamingue obtained the permission of the author to use a copy of this document for non-profit purposes in order to put it in the open archives Depositum, which is free and accessible to all.

The author retains ownership of the copyright on this document. Neither the whole document, nor substantial extracts from it, may be printed or otherwise reproduced without the author's permission.

UNIVERSITÉ DU QUÉBEC EN ABITIBI-TEMISCAMINGUE

CHARACTERIZATION OF EM NOISE IN DEEP MINING TUNNELS AND
APPLICATION OF DENOISING METHOD

THESIS PRESENTED IN PARTIAL FULFILLMENT OF THE REQUIREMENTS
FOR THE DEGREE OF DOCTOR OF PHILOSOPHY IN ENVIRONMENTAL
SCIENCES

BY
XUEPING DAI

MARCH 2019

ACKNOWLEDGMENTS

There are a large number of people I would like to thank for their generous support.

Firstly, I would like to express my sincere gratitude to my supervisor Prof. Lizhen Cheng for the continuous support of my Ph.D. study and related research, for her patience, guidance, and encouragement. Not only does she guide me in research, but she also teaches me how to become a better person. I cannot ask for a better mentor than her.

Besides my supervisor, I would like to thank the vice-supervisor of my thesis: Prof. Jean-Claude Mareschal from the Université du Québec à Montréal (UQAM), and Prof. Daniel Lemire from the TÉLUQ University, for their insightful suggestions and encouragement. Questions they posed have largely widened my research from various perspectives.

I would like to thank the FRQNT (le Fonds de Recherche du Québec–Nature et Technologies) and our industry partners (Abitibi Geophysique Inc., Agnico Eagle Ltd.) for financial support. I would particularly thank Jonathan Collins and Pierre Bérubé of Abitibi Geophysique for their precious advice from a practical point of view.

I would like also give special thanks to the committee members of my PhD dissertation: president, Dr. Fiona Ann Darbyshire, external examiner Dr. Bernard Giroux, and internal examiner Dr. Mourad Nedil. Thanks for their time and their valuable comments that make improvement of my thesis.

Last but not least, I would like to thank my family, my parents, my brother, my sister, and my girlfriend for supporting me spiritually throughout this doctoral project and my life in general. I also thank my colleagues and all personnel at UQAT for their generous help whenever I need.

TABLE OF CONTENTS

LIST OF FIGURES	viii
LIST OF TABLES	xiii
RÉSUMÉ	xiv
ABSTRACT	xv
CHAPTER I GENERAL INTRODUCTION	1
1.1 Background	1
1.2 Introduction of the BHTEM systems	2
1.3 Objectives of research	5
1.4 Thesis outline	6
CHAPTER II METHODS AND THEORY	7
2.1 Wavelet transform	7
2.1.1 Continuous wavelet transform (CWT).....	8
2.1.2 Discrete wavelet transform (DWT).....	13
2.1.3 Selection of a wavelet	16
2.2 Complementary methods	18
2.2.1 Curve fitting technique (CFT).....	19
2.2.2 Correlation analysis and stacking.....	23
2.2.3 Stacking.....	26
CHAPTER III CHARACTERISATION OF EM NOISES IN DEEP MINING TUNNELS	28
3.1 Introduction	28
3.2 A brief description of LaRonde Mine	29

3.3	Geological setting of LaRonde Mine	31
3.4	Data acquisition.....	32
	3.4.1 Zonge Electromagnetic Network (ZEN) receiver	32
	3.4.2 Sites of recordings.....	34
	3.4.3 Recorded signals	35
3.5	Recorded time series	36
3.6	Data analysis	39
	3.6.1 Analysis with the Fourier transform	39
	3.6.2 Analysis with the CWT.....	46
3.7	Conclusion	52
CHAPTER IV DENOISING THE BHEM DATA WITH DISCRETE WAVELET TRANSFORM BASED METHOD.....		53
4.1	Introduction.....	53
4.2	Using the DWT to denoise BHEM data	55
	4.2.1 Strategy of applying the DWT to BHEM data	55
	4.2.2 Choice of suitable wavelet and decomposition level	57
4.3	Method validation	60
	4.3.1 Application of DWT on synthetic data	60
	4.3.2 Application on field data.....	65
CHAPTER V GENERAL CONCLUSION		75
APPENDIX I RESULTS OF CHANNEL 2 (EY) AND CHANNEL 3 (HX).....		78
I.1	Results of acquisition site #1.....	78
I.2	Results of acquisition site #2.....	80
I.3	Results of acquisition site #3.....	82
I.4	Results of acquisition site #4.....	84
I.5	Results of acquisition site #5.....	86
APPENDIX II MATLAB PROGRAMS FOR ANALYZING DATA COLLECTED IN GALLERIES AT THE LARONDE MINE.....		88
II.1	Main MATLAB program: LaRondeDataAnaly.m.....	88

II.2	Functions	91
II.2.1	Get_data.m	91
II.2.2	readZ3D.m	92
II.2.3	helperCWTTTimeFreqVector.m	103
II.2.4	parsing.m	103
II.2.5	Fourier.m	104
APPENDIX III MATLAB PROGRAMS FOR VALIDATING THE DENOISING METHOD ON SYNTHETIC AND FIELD DATA.....		105
III.1	Main MATLAB program: ValidationOnSyntheticData.m	105
III.2	Main MATLAB program: ValidationOnFieldData.m	109
III.3	Functions	114
III.3.1	DWTDenoise.m	114
III.3.2	CurveFitting.m	115
III.3.3	PeaksAndValleys.m	116
III.3.4	CorrelationAnaly.m.....	116
REFERENCES.....		119

LIST OF FIGURES

Figure		page
1.1	Geoelectric cross section illustrating the application of the BHTEM in exploring deep targets (adapted from Dyck, 1981).	4
1.2	The three components (A , U , V) recorded by the sensor. A —parallel to the trajectory of the borehole (coaxial component), U —in the same vertical plane as A and perpendicular to A , V —perpendicular to A and U in a right-hand coordinate system.....	5
2.1	Resolution difference in time between the STFT (left) and the WT (right): (a) uniform tiling; (b) scale adaptive tiling.....	9
2.2	Stationary signal s_1 (a) and non-stationary signal s_2 (b) in the time domain.	11
2.3	Frequency representations of s_1 and s_2 by using the FT.	12
2.4	Spectrograms obtained by applying the STFT and WT on signals s_1 and s_2	13
2.5	Implementation of the DWT in terms of filter banks (the downward arrow indicates down-sampling by a factor of two) (Percival and Walden, 2006).....	15
2.6	A signal is decomposed to level 3 with the DWT.....	16
2.7	Definition of the prominence of a peak. Vertical arrows indicate the prominence of the peak. (source: https://commons.wikimedia.org/wiki/File:Prominence_definition.svg).....	21
2.8	Perturbations exist in the result of denoising with the DWT	22
2.9	Peaks/valleys located in the DWT denoised signal.....	23
2.10	Comparison between the DWT denoised result and DWT+CFT processed result.....	23

2.11	Basic principles of measurement of the TEM method. The red line indicates the current in the transmitter loop, and the blue line shows the signal recorded by the sensor.	24
2.12	Schematic diagram illustrating the process of replacing distorted transient with interpolation.	26
3.1	Geological map and location of the LaRonde mine (Source : modified from interactive carte of SIGEOM, MERNQ, http://sigeom.mines.gouv.qc.ca/signet/classes/I1108_afchCarteIntr) ..	30
3.2	Composite longitudinal section of the LaRonde mine (Source : https://www.agnicoeagle.com/English/operations-and-development-projects/operations/laronde/maps-and-surveys/default.aspx).	31
3.3	The Zonge Electromagnetic Network (ZEN) receiver (Source: Zonge International Inc.).	33
3.4	Locations of the five data acquisition sites (scale: 1:2000).	35
3.5	The current in the conveyor varies with time.	36
3.6	Electric components (E_x and E_y) from five acquisition sites. From top to bottom: site #1, site #2, site #3, site #4, and site #5.	37
3.7	Magnetic components (H_x and H_y) from five acquisition sites. From top to bottom: site #1, site #2, site #3, site #4, and site #5.	38
3.8	FT results of the two segments of the electric field component E_x and the magnetic component H_y at site #1.	40
3.9	FT results of the two segments of the electric field component E_x and the magnetic component H_y at site #2.	41
3.10	FT results of the two segments of the electric field component E_x and the magnetic component H_y at site #3.	42
3.11	FT results of the two segments of the electric field component E_x and the magnetic component H_y at site #4.	43

3.12	FT results of the two segments of the electric field component Ex and the magnetic component Hy at site #5.	44
3.13	Average spectra and variance of the electric field component Ex (left column) and the magnetic component Hy (right column) at site #2 (blue line is the average spectrum of segments from quiet period of time; red line is the average spectrum of segments from quiet period of time).	46
3.14	Time-frequency representation of the two segments of the electric field component Ex and the magnetic component Hy from site #1.	47
3.15	Time-frequency representation of the two segments of the electric field component Ex and the magnetic component Hy from site #2.	48
3.16	Time-frequency representation of the two segments of the electric field component Ex and the magnetic component Hy from site #3.	49
3.17	Time-frequency representation of the two segments of the electric field component Ex and the magnetic component Hy from site #4.	50
3.18	Time-frequency representation of the two segments of the electric field component Ex and the magnetic component Hy from site #5.	51
4.1	Comparison of hard and soft thresholding techniques (Nagendra et al., 2013).	56
4.2	Comparison of the original signal and the reconstructed signals.	57
4.3	The 3D model used to generate synthetic data.	59
4.4	The BHEM noise-free signal (a) generated by Loki from the model in Figure 4.3 and the corresponding noisy signal (b).	59
4.5	Three types of noise added to synthetic data. From top to bottom: random noise, sferics, and noise from the power line (50 and 60 Hz).	60
4.6	The synthetic noisy signals (a) and (c) at different noise level, the SNR after the DWT is increased from 30 dB to 52 dB (b), and from 25 dB to 47 dB (d), respectively.	61

4.7	The synthetic noisy signal (a) and the result obtained from the DWT (b). In this case the SNR is increased from 20 dB to 40 dB. Slight perturbations appear in the DWT processed result.	62
4.8	The synthetic noisy signal (a) and the result obtained from the DWT (b). In this case the SNR is increased from 15 dB to 35 dB. As the noise level increases, the perturbation in the DWT processed result becomes more severe.	62
4.9	Comparison of denoising results before and after curve fitting.	63
4.10	Relative error curves, (a) the error curve of the noisy signal, (b) the error curve of the denoised signal when only DWT is used, (c) the error curve of the denoised signal after DWT and CFT.	64
4.11	Raw data of component-A. (a) Original raw data, (b) denoised raw data, (c) denoised raw data with distortion corrected.	67
4.12	Stacked on-time signals for component-A.	68
4.13	Stacked off-time signals for component-A.	68
4.14	Raw data of component-U. (a) Original raw data, (b) denoised raw data, (c) denoised raw data with distortion corrected.	69
4.15	Stacked off-time signals for component-U.	70
4.16	Stacked off-time signals for component-U.	71
4.17	Raw data of component-V. (a) Original raw data, (b) denoised raw data, (c) denoised raw data with distortion corrected.	72
4.18	Stacked on-time signals for component-V.	73
4.19	Stacked off-time signals for component-V.	73
I.1	FT results of the two segments of the electric field component E_y and the magnetic component H_x at site #1.	78
I.2	Time-frequency representation of the two segments of the electric field component E_y and the magnetic component H_x from site #1.	79
I.3	FT results of the two segments of the electric field component E_y and the magnetic component H_x at site #2.	80

I.4	Time-frequency representation of the two segments of the electric field component E_y and the magnetic component H_x from site #2.....	81
I.5	FT results of the two segments of the electric field component E_y and the magnetic component H_x at site #3.....	82
I.6	Time-frequency representation of the two segments of the electric field component E_y and the magnetic component H_x from site #3.....	83
I.7	FT results of the two segments of the electric field component E_y and the magnetic component H_x at site #4.....	84
I.8	Time-frequency representation of the two segments of the electric field component E_y and the magnetic component H_x from site #4.....	85
I.9	FT results of the two segments of the electric field component E_y and the magnetic component H_x at site #5.....	86
I.10	Time-frequency representation of the two segments of the electric field component E_y and the magnetic component H_x from site #5.....	87

LIST OF TABLES

Table		Page
2.1	Pearson coefficients between five transients.	25
3.1	Description of all recording sites. The five sites are all located in the tunnels at 3000m depth.	34
4.1	Applying different wavelets on a noisy signal with an SNR of 15dB with a decomposition level of 10.	58
4.2	Trying different decomposition levels on a noisy signal with an SNR of 15dB.	58
4.3	Values of MSE and SNR of different signals.	64

RÉSUMÉ

Comme les ressources minérales superficielles sont presque épuisées, les mines existantes rencontrent des difficultés pour maintenir leur production. Une solution relativement économique consiste à trouver des corps minéralisés à proximité des propriétés minières. Ces corps sont souvent hors de la capacité de détection des méthodes de prospection conventionnelles de surface en raison de leur taille ou de leur profondeur. Les trous de forage et les galeries des mines fournissent d'excellents chemins d'accès pour les méthodes d'exploration en profondeur. Le but de ce projet est d'aider l'industrie minière à résoudre les problèmes rencontrés lors de l'exploration en profondeur.

La méthode électromagnétique transitoire (TEM) dans les galeries pourrait aider l'industrie minière à atteindre les objectifs d'extension en profondeur. L'un des défis pour effectuer des mesures TEM dans les galeries est l'espace restreint, qui nous force à utiliser de petites boucles d'émetteur. Par conséquent, les signaux sont plus affectés par le bruit. Dans ce projet, nous avons caractérisé les sources de bruit potentielles dans un environnement minier profond. Ceci facilitera le traitement des données et améliorera la précision de l'interprétation des données électromagnétiques.

La méthode électromagnétique transitoire en forage est devenue une pratique omniprésente dans l'exploration en profondeur grâce à sa capacité à détecter des cibles dans un rayon de plusieurs centaines de mètres autour du forage. Une combinaison des mesures dans les galeries et dans les trous de forage, permet de chercher des informations géologiques en trois dimensions. Afin d'améliorer le rapport signal sur bruit des signaux électromagnétiques mesurés, nous avons développé une méthodologie de débruitage en utilisant les fonctions de la transformée en ondelettes discrète dans la boîte à outils d'ondelettes de Matlab. Les résultats ont démontré que l'application de la transformée en ondelettes discrète seule peut effectivement réduire le niveau de bruit, mais dans certains cas, une méthode supplémentaire est nécessaire pour éliminer les résidus de petites perturbations. Ensuite, une méthode d'ajustement de courbe, plus d'analyse de corrélation se sont ajoutées dans la procédure de traitement de données.

Mots clés : méthode électromagnétique transitoire en forage, bruit électromagnétique, débruitage en utilisant la transformée en ondelettes discrète, tunnels miniers souterrains profonds.

ABSTRACT

As shallow located mineral resources are exhausting, existing mines face difficulties to maintain productions. One relatively cost-efficient solution is to find ore bodies near the mining properties. These ore bodies are often out of the detection capability of conventional ground prospecting methods due to the size of the ore bodies or their depth. Existing boreholes and tunnels at mining sites provide excellent access paths to deep exploration targets. This project is created to help the mining industry to solve problems encountered in deep exploration.

In the project, we characterized potential noise sources for EM measurements in tunnels. The TEM method in tunnels is a potential way to help the mining industry on its deep extension. One of the challenges to carry out TEM measurements in tunnels is the limited space, which forces to use small transmitter loops. Consequently, signals are more vulnerable to noises. Characterizing EM noise sources in tunnels will certainly help facilitate data processing and improve interpretation of EM data accurately.

The borehole transient electromagnetic (BHTEM) method has become pervasive in the deep exploration for its ability to detect targets around the borehole in a range up to hundreds of meters. The present PhD research focuses on improving the signal-to-noise ratio of electromagnetic signals measured in boreholes. We have developed a denoising methodology using functions of discrete wavelet transform in the Wavelet toolbox. The results demonstrated that the application of the discrete wavelet transform alone can effectively reduce the noise level, but in some cases an additional method is needed to remove the small disturbance residues. As a result, a curve fitting method plus correlation analysis was added in the data processing procedure.

Key words: borehole transient electromagnetic method, EM noise, denoising with discrete wavelet transform, deep underground mining tunnels.

CHAPTER I

GENERAL INTRODUCTION

1.1 Background

Natural resources provide essential basic materials for the modernization and the development of human society. After centuries' exploration and exploitation, the discovery of new resources becomes more difficult and mining development requires deep exploration. Despite innovations in exploration methods and improvements in data interpretation techniques, the average cost of the discovery of an economic mineral deposit has surged in the past decades. One way to reduce expenditures of the exploration is to find new ore bodies close to constructed infrastructure, and to increase the ability to delineate resources in three dimensions. Under this circumstance, the borehole transient electromagnetic method (BHTEM) has attracted the attention of exploration geophysicists for its effective cost performance. Compared with surface geophysical methods and borehole logging, the BHTEM has two major advantages. First because the sensor is placed in the borehole, measurements are less affected by overburden and shallow uneconomic conductors, and in most cases, the sensor is located closer to deep targets. Secondly, in the BHTEM measurement, one or multiple large transmitter loops are laid out near the collar of the borehole, which ensures a strong primary field to couple with the conductor (ore body). In addition, the range of influence of the BHTEM field around the borehole or, the detection distance in three dimensions increases significantly

with the advancement of technology, such as the appearance of three-component sensor and more advanced ADCs (24-bit, 36-bit). With these features, the BHTEM has the ability to detect deep and small conductors, in a range of hundreds of meters around or below the borehole, which are generally out of the detection capability of surface techniques.

With the advantage in detecting deep conductors, the BHTEM has developed into an essential tool in the deep exploration for massive sulphide deposits (Lamontagne and Milkereit, 2007). In 1978, the Corporation Falconbridge Copper discovered a small off-hole copper sulphide ore body at a depth of 950 m using borehole transient EM method (Crone, 1986). In 1981, the Corporation Falconbridge Copper again using the BHTEM method detected a massive sulphide, copper, zinc deposit at a depth of 1266m in the Noranda area of Quebec, Canada (Crone, 1986). King (1996) introduced the application of the BHTEM method to detect and define nickel-copper deposits in Sudbury Igneous Complex using the UTEM (University of Toronto EM) system, which is a large loop, step response system with the ability to detect conductors up to 300m away from the borehole at a depth up to 3000m. In a mining area with a large number of boreholes, well-to-well electromagnetic measurement can help more accurately estimate mineral reserves. As targets based on earlier exploration strategy became exhausted in the Mount Isa Mine, which is an underground mine in Australia, the BHTEM method has been used as a part of a new exploration strategy to find further resources (Fallon *et al.*, 1996).

1.2 Introduction of the BHTEM systems

One of the first application of the electromagnetic method to borehole was introduced in the thesis of Noakes (1951). The method is designed to detect massive sulfide deposits which are a certain distance away from the borehole. Since then numerous borehole electromagnetic systems have been developed. Crone Geophysics & Exploration built the first three-component commercial borehole electromagnetic

system in 1991 (PEM), consisting of two probes (one for the z component and one for x and y components). The Geonics BH43 system combines all three components into a single probe in 1994. Both systems measure components sequentially. In 2005, Lamontagne Géophysique ltée launched the UTEM system and EMIT's DigiAtlantis system (ElectroMagnetic Imaging Technology) appeared in 2010. The latter two use a fluxgate probe that measures the time derivative of the three magnetic components simultaneously. Recently, the ARMIT system represents a new generation of technology (Abitibi Royal Melbourne Institute of Technology) and it relies on a new sensor developed exclusively for Abitibi Geophysics by the team of Dr. James Macnae of the Royal Melbourne Institute of Technology. The novelty of the ARMIT system is that it simultaneously measures the time derivative of the secondary magnetic field B (dB/dt) and the secondary magnetic field (B). This latter possibility is innovative and sought around the world. This EM probe offers increased sensitivity to the entire spectrum of geological conductors that can be found in nature.

In a typical BHTEM configuration, shown in Figure 1.1, there are a large transmitter loop, a winch and a receiver on the surface, and a sensor connected with the receiver through a cable, is lowered in the borehole.

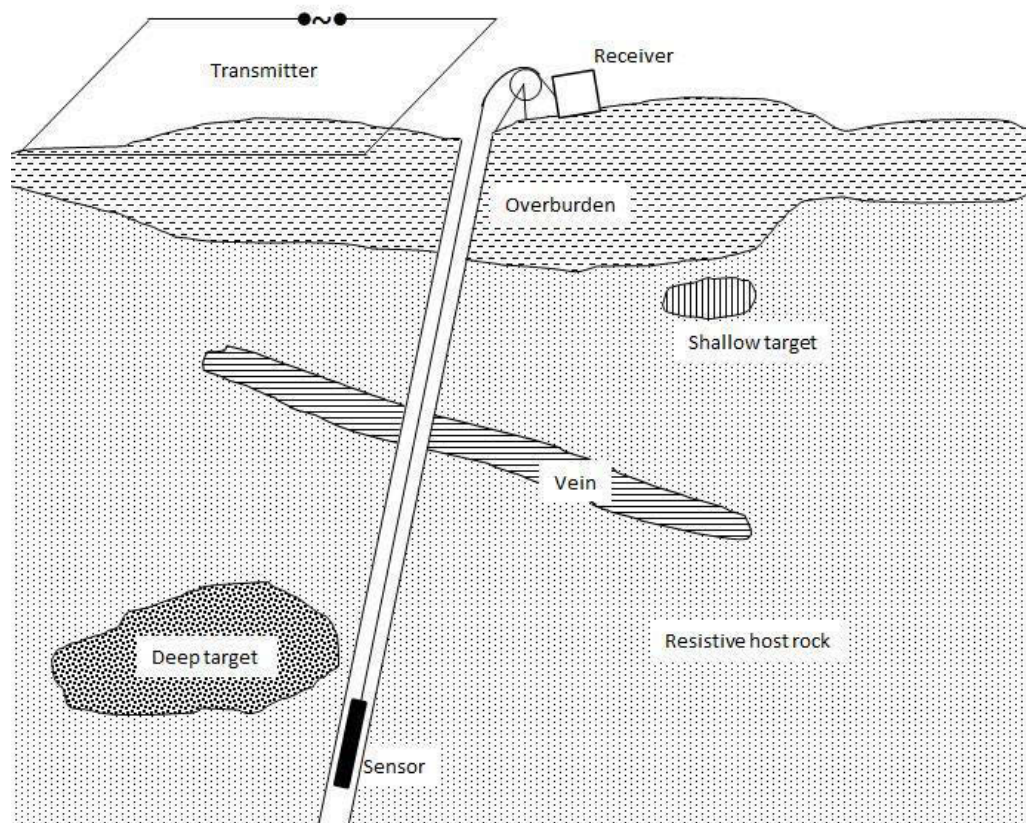


Figure 1.1 Geoelectric cross section illustrating the application of the BHTEM in exploring deep targets (adapted from Dyck, 1981).

The basic principles of the BHTEM are the same as surface time domain EM. A strong direct current is injected into the transmitter loop for a certain time until all turn-on transients have vanished, giving the primary electric field; then, the current through the transmitter loop is cut off, and the primary electric field has been changed abruptly. According to Faraday's law, the abrupt change will induce eddy currents in nearby conductors, because of ohmic losses these eddy currents dissipate gradually. The dissipation of these eddy currents, in turn, induces a decaying magnetic field which is the secondary magnetic field. It is the magnetic induction B or its time rate dB/dt of the secondary magnetic field recorded by the receiver. At present all systems effectively perform 3-axis component measurements, one axial component (A) and two transverse components (U and V), as shown in Figure 1.2.

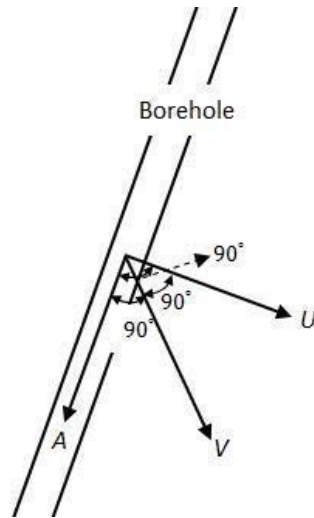


Figure 1.2 The three components (*A*, *U*, *V*) recorded by the sensor. *A*—parallel to the trajectory of the borehole (coaxial component), *U*—in the same vertical plane as *A* and perpendicular to *A*, *V*—perpendicular to *A* and *U* in a right-hand coordinate system.

The BHTEM method shares the same principle with other TEM methods (airborne TEM, and ground TEM), however, challenges exist in processing BHTEM data because of the noise. Apart from common noises encountered airborne TEM and ground TEM, such as motion induced noise, cultural noise and sferics (Macnae *et al.*, 1984), the hostile environment in a borehole, especially in deep holes, there are some additional sources of noise as thermal noise at high temperature, flowing liquid in well, and the rotation of the sensor. These problems of BHTEM motivate us to develop an effective and efficient denoising method for BHTEM data.

1.3 Objectives of research

With the financial support of FRQNT (Fonds de recherche, Nature et Technologies du Québec), the main goal of this Ph.D. research is to develop an efficient denoising tool dedicated to BHTEM measurement for deep mine exploration. The research has been carried out in close collaboration with Abitibi Geophysics Inc. Therefore, our work is focused on providing an effective and easy to use tool for field geophysicists

to improve data quality, thus improve the accuracy of interpretation. Three specific objectives have been accomplished through this research:

- a) As everything can give an electromagnetic signal in response to an induced electromagnetic field, identify the main sources of noise in a typical deep mine environment is one of the objectives of this Ph.D. study.
- b) The second specific objective is to develop new noise elimination algorithms. A strategy for improving BHTEM data quality has been developed. The strategy involves denoise raw data by a discrete wavelet transform; moreover, distorted transients are identified by correlation analysis, and then these distorted transients are corrected.
- c) Develop an interface for denoising BHTEM raw data in the Matlab environment, in order to transfer the denoising tool to the industrial partner.

1.4 Thesis outline

This thesis has been divided into five chapters of which Chapter I is the general introduction.

Chapter II summarizes the theory of the signal processing methods used in the frame of this Ph.D. research.

Chapter III describes briefly on the data acquisition in tunnels of a deep mine. As an effort to investigate influences of the environment on EM measurements, the recordings are analyzed using both the Fourier and the wavelet transform integrating information from seismic records, blasting, fluctuation in powerlines.

Chapter IV focus on the development of a new denoising method for BHTEM data based on DWT. Results of using the method to denoise synthetic and field BHTEM data are presented in detail.

Chapter V draws conclusions and gives some recommendations for future work.

CHAPTER II

METHODS AND THEORY

2.1 Wavelet transform

Basic concepts and theory of the wavelet transform (WT) described in this section mainly refer to Daubechies (1992), Chui (1992), Mallat (1999), Percival and Walden (2006).

The wavelet transform (WT) has often been compared with the Fourier transform (FT) and can be considered as an improved, localized equivalent of it. They share the same principle, which is that all signals can be decomposed into a superposition of functions, called basis functions. These basis functions possess certain properties: simple, harmonic, symmetry, orthogonal. Therefore, the process of analysis based on the decomposition is simplified. After the processing, the signal can be reconstructed through a process called inverse transformation (IWT, and IFT). In the case of FT, the signal is decomposed into an integral or sum of trigonometric functions with different frequencies. Each trigonometric function represents a frequency component of the original signal. This facilitates the analysis of a signal in the frequency domain. It shows how much of the signal lies within a specific frequency, however, this is at the cost of time information. In other words, it does not tell us when an event occurs in the signal. The WT remedies the deficiency of the FT by changing the basis function from trigonometric- functions to mother wavelets, which are a waveform of limited duration, zero average value, and nonzero norm. The advantage of using wavelets as

the basis functions is that it enables one to study features of the signal locally with a detail matched to their scale (Kumar and Foufoula-Georgiou, 1994). In other words, the WT allows analyzing a time series at different scales without sacrificing time resolution.

2.1.1 Continuous wavelet transform (CWT)

Using FT to analyze the frequency content of a time series, the basis function is explicitly defined as the trigonometric function, which has an infinite duration as defined in equation (2.1).

$$\mathcal{F}f(\omega) = \frac{1}{\sqrt{2\pi}} \int_{-\infty}^{\infty} f(t)e^{-i\omega t} dt. \quad (2.1)$$

The selection of trigonometric function as the basis function results in an inherent limitation of the FT: it provides high resolution in frequency without offering any time information about the signal. If the signal is stationary, which means the frequency content of the signal does not change over time, the FT would be a good choice. For non-stationary signals, whose frequency content changes over time, the FT does not provide enough information to characterize the signal.

In order to provide time-localized information in the frequency domain, a windowing function is added to the Fourier transform (Gabor, 1946). It is called short-time Fourier transform (STFT):

$$STFTf(\omega, \tau) = \int_{-\infty}^{\infty} f(t)w(t - \tau)e^{-i\omega t} dt. \quad (2.2)$$

The introduction of the windowing function, $w(t)$, splits the signal that changes with time into small segments, and it assumes the signal is stationary in each segment. This technique has remedied the deficiency of the FT to a certain degree. However, once $w(t)$ is chosen, the size of the window is fixed. This is the main disadvantage of the STFT in dealing with non-stationary processes, which requires varying window size to give reasonable resolution for both time- and frequency-localized events. This

is what exactly wavelet transform provides. The WT uses a wide window for low-frequency events and a narrow window for high-frequency contents. Figure 2.1 illustrates the time resolution difference as frequencies ascend for the Fourier transform and the wavelet transform. For the FT, the resolution is uniform for all frequencies. However, in the WT, the time resolution increases with the increase of the frequency.

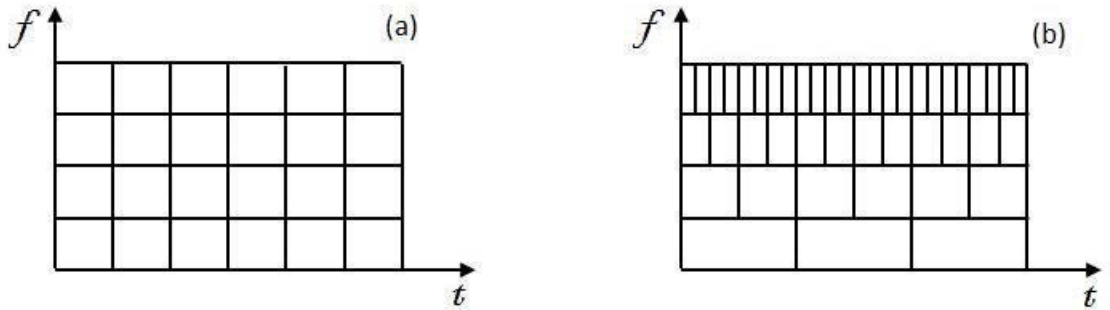


Figure 2.1 Resolution difference in time between the STFT (left) and the WT (right): (a) uniform tiling; (b) scale adaptive tiling.

The continuous wavelet transform (CWT) of a time series with finite energy is defined as:

$$CWF(a, b) = \int_{-\infty}^{\infty} f(t)\psi_{a,b}(t)dt. \quad (2.3)$$

Here a and b are scale and translation parameters. The function $\psi_{a,b}(t)$ is called the mother wavelet, which does not have a general formulation, but must meet the following two conditions:

$$\int_{-\infty}^{\infty} \psi(t)dt = 0, \quad (2.4)$$

$$C_{\psi} = \int_{-\infty}^0 \frac{|\mathcal{F}\psi(\omega)|^2}{\omega} d\omega = \int_0^{\infty} \frac{|\mathcal{F}\psi(\omega)|^2}{\omega} d\omega < \infty. \quad (2.5)$$

The symbol \mathcal{F} indicates the Fourier transform. The most important operation implemented in equation (2.3) is scaling and translating a mother wavelet with the help of the scale and translation parameters (a and b , respectively). A wavelet family

has wavelets of the same shape, but various dilation levels and positions defined as below:

$$\psi_{a,b}(t) = \frac{1}{\sqrt{a}} \psi\left(\frac{t-b}{a}\right) \quad a, b \in R; a > 0. \quad (2.6)$$

After the CWT, a set of coefficients is obtained. Processes, such as removing certain frequency contents from the signal, can be operated on these coefficients. Since the transform is isometric, i.e. it preserves the energy of the signal, the transformation is reversible. The reverse continuous wavelet transform (iCWT) is defined as:

$$iCWF(t) = \frac{1}{c_\psi} \int_{-\infty}^{\infty} \int_{-\infty}^{\infty} \frac{1}{a^2} CWF(a, b) \psi_{a,b}(t) da db. \quad (2.7)$$

In order to make a comparison between FT, STFT, and WT, two time series of signals are generated. One is a stationary signal (s_1) and another is a non-stationary signal (s_2). The s_1 is a sinusoid signal consisted of three frequency components: 30Hz, 50Hz, and 80Hz. The non-stationary signal s_2 is composed of two frequency components: 50Hz and 80Hz. Except that the 50Hz component is present everywhere in the signal s_2 , the 80Hz component only occurs between 400ms and 600ms. Figure 2.2 presents the two signals in time domain.

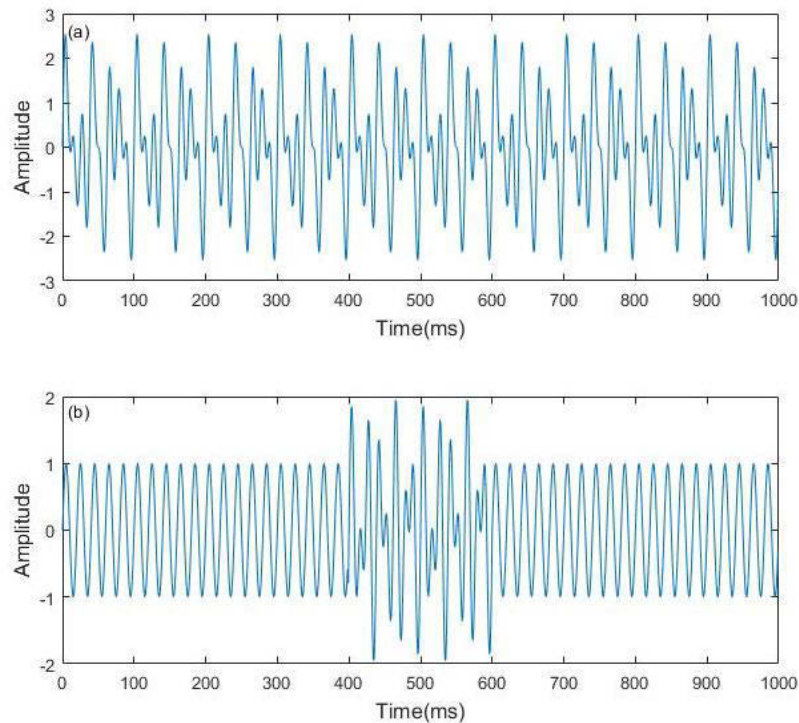


Figure 2.2 Stationary signal s_1 (a) and non-stationary signal s_2 (b) in the time domain.

Those two signals were then processed by three transformations one by one, namely FT, STFT, and WT. Figure 2.3 presents the results of FT for the two signals. In both cases, the frequency components are identified successfully but it fails to show the time-varying features in the non-stationary signal s_2 , because all time information is lost after the transformation. This is a severe weakness of the FT in dealing with non-stationary signals. To overcome this weakness the STFT and WT are available. In Figure 2.4, we can see for the stationary signal both the STFT and WT have correctly detected the three frequency components in the signal; however, the STFT gives uniform resolution for all frequency components, because the resolution is pre-decided by the selection of the window size. Comparatively, the WT offers different resolution for different frequencies. Moreover, the WT provides much better time precision for non-stationary signals than the STFT.

These results (Figure 2.4) show that the WT is much better than the other two methods, especially for non-stationary signals. In reality, geophysical signals are often non-stationary.

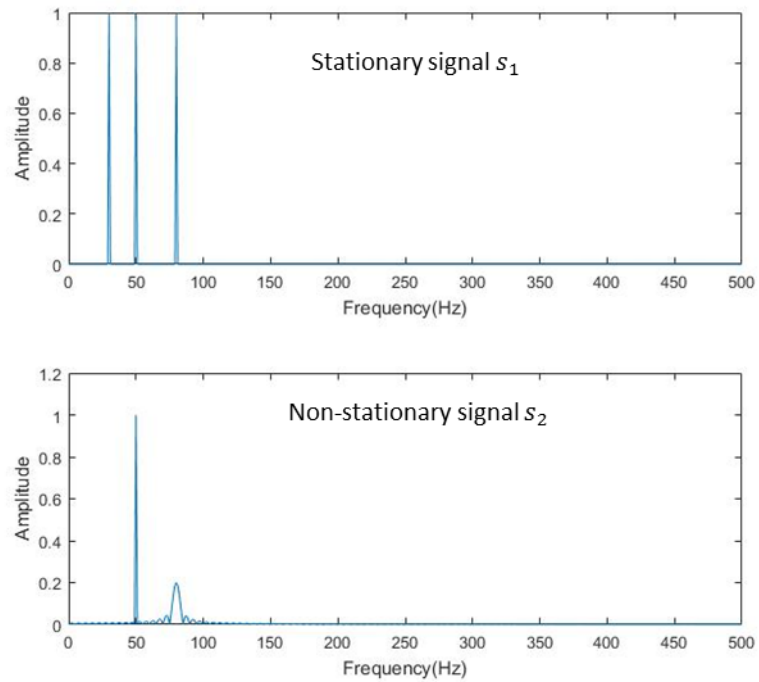


Figure 2.3 Frequency representations of s_1 and s_2 by using the FT.

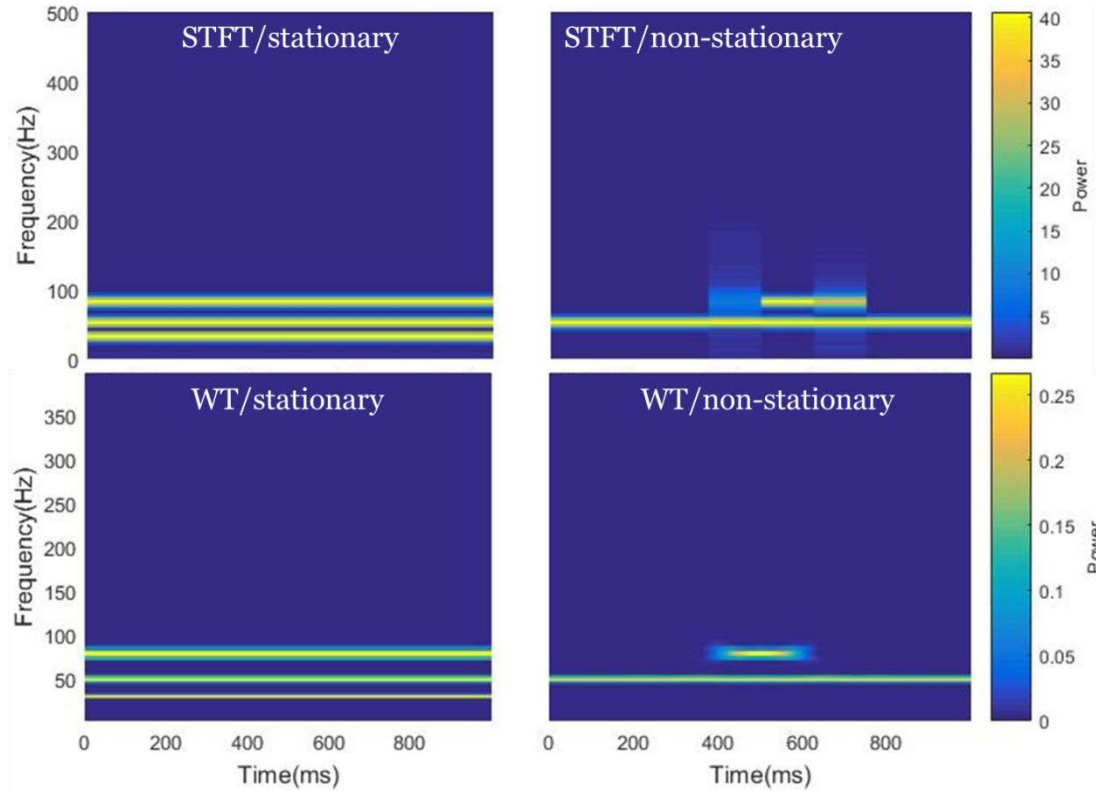


Figure 2.4 Spectrograms obtained by applying the STFT and WT on signals s_1 and s_2 .

2.1.2 Discrete wavelet transform (DWT)

Since the scale and translation parameters (a , b) are continuous, information provided by the CWT is highly redundant, which makes the CWT computationally inefficient. It is used usually for analytic purposes. To reduce the redundancy, parameters a and b are discretized, and often use dyadic values as below:

$$a = 2^j; b = k \cdot a = k \cdot 2^j \quad j, k \in \mathbb{Z}. \quad (2.8)$$

Where j is called the decomposition level, which controls the dilation; k controls the translation. Substitute equation (2.8) into equation (2.6), the wavelet family becomes:

$$\psi_{j,k}(t) = \frac{1}{\sqrt{2^j}} \psi\left(\frac{t-k \cdot 2^j}{2^j}\right). \quad (2.9)$$

Therefore, the DWT of a time series function $f(t)$ is:

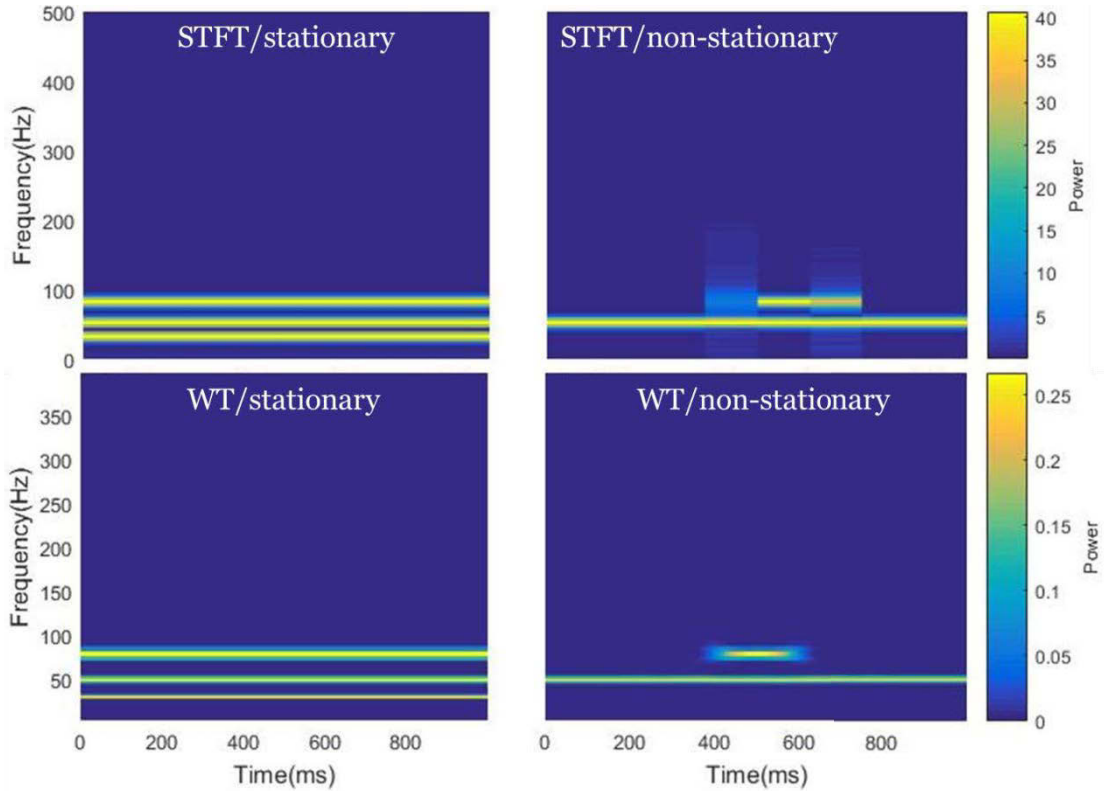


Figure 2.4 Spectrograms obtained by applying the STFT and WT on signals s_1 and s_2 .

2.1.2 Discrete wavelet transform (DWT)

Since the scale and translation parameters (a , b) are continuous, information provided by the CWT is highly redundant, which makes the CWT computationally inefficient. It is used usually for analytic purposes. To reduce the redundancy, parameters a and b are discretized, and often use dyadic values as below:

$$a = 2^j; b = k \cdot a = k \cdot 2^j \quad j, k \in \mathbb{Z}. \quad (2.8)$$

Where j is called the decomposition level, which controls the dilation; k controls the translation. Substitute equation (2.8) into equation (2.6), the wavelet family becomes:

$$\psi_{j,k}(t) = \frac{1}{\sqrt{2^j}} \psi\left(\frac{t-k \cdot 2^j}{2^j}\right). \quad (2.9)$$

Therefore, the DWT of a time series function $f(t)$ is:

$$DWf(j, k) = \int_{-\infty}^{\infty} f(t) \cdot \psi_{j,k}(t) dt = \langle f, \psi_{j,k} \rangle. \quad (2.10)$$

In DWT, the wavelet is selected to form an orthonormal basis for functions with finite energy. This implies that all such functions can be approximated by a linear combination of the wavelets (Kumar and Foufoula-Georgiou, 1994):

$$f(t) = \sum_{j=-\infty}^{\infty} \sum_{k=-\infty}^{\infty} \langle f, \psi_{j,k} \rangle \psi_{j,k}(t). \quad (2.11)$$

The two indices j and k indicate scale and position, respectively. Hence, DWT has the time-scale, or time-frequency, localization ability.

Defining J as the decomposition level, the equation (2.11) can be broken into two parts:

$$f(t) = \sum_{j=-\infty}^J \sum_{k=-\infty}^{\infty} \langle f, \psi_{j,k} \rangle \psi_{j,k}(t) + \sum_{j=J+1}^{\infty} \sum_{k=-\infty}^{\infty} \langle f, \psi_{j,k} \rangle \psi_{j,k}(t). \quad (2.12)$$

The first part is called details of the function. The second part is called the approximate of the function.

To simplify the process the scale function $\phi_{j,k}(t)$ is introduced, and it can be defined analogically to the wavelet function $\psi_{j,k}(t)$ in equation 2.9:

$$\phi_{j,k}(t) = \frac{1}{\sqrt{2^j}} \phi\left(\frac{t-k \cdot 2^j}{2^j}\right). \quad (2.13)$$

Details on finding the scale functions can be found in Mallat (1989). With the scale function, the second sum on the right side of the equation (2.12) can be rewritten as:

$$\sum_{j=J+1}^{\infty} \sum_{k=-\infty}^{\infty} \langle f, \psi_{j,k} \rangle \psi_{j,k}(t) = \sum_{k=-\infty}^{\infty} \langle f, \phi_{J,k} \rangle \phi_{J,k}(t). \quad (2.14)$$

Therefore:

$$f(t) = \sum_{j=-\infty}^J \sum_{k=-\infty}^{\infty} \langle f, \psi_{j,k} \rangle \psi_{j,k}(t) + \sum_{k=-\infty}^{\infty} \langle f, \phi_{J,k} \rangle \phi_{J,k}(t). \quad (2.15)$$

As a result of DWT, the signal is decomposed into detail ($D_{j,k}$) and approximate ($A_{j,k}$) coefficients at level j and time k , and they are defined in equation (2.16).

$$\begin{aligned} D_{j,k} &\equiv \int_{-\infty}^{\infty} \langle f, \psi_{j,k} \rangle \psi_{j,k}(t) dt \\ A_{j,k} &\equiv \int_{-\infty}^{\infty} \langle f, \phi_{j,k} \rangle \phi_{j,k}(t) dt \end{aligned} \quad (2.16)$$

Please note that the equation (2.16) is used to calculate coefficients of single scale decomposition. To calculate wavelet coefficients for a certain decomposition level, multiple scale decomposition mechanism must be used. Figure 2.5 illustrates the DWT process for multiple decomposition levels:

1. At first, the signal is fed to a highpass filter and a lowpass filter producing the level one detail coefficients and approximation coefficients, respectively.
2. The detail coefficients are kept unchanged; the approximation coefficients are fed to another highpass filter and another lowpass filter producing level two detail coefficients and approximation coefficients. This process is repeated until the desired decomposition level is reached.
3. The decomposition process is a down-sampling process by a factor of two. To reconstruct the signal the coefficients are upsampled.

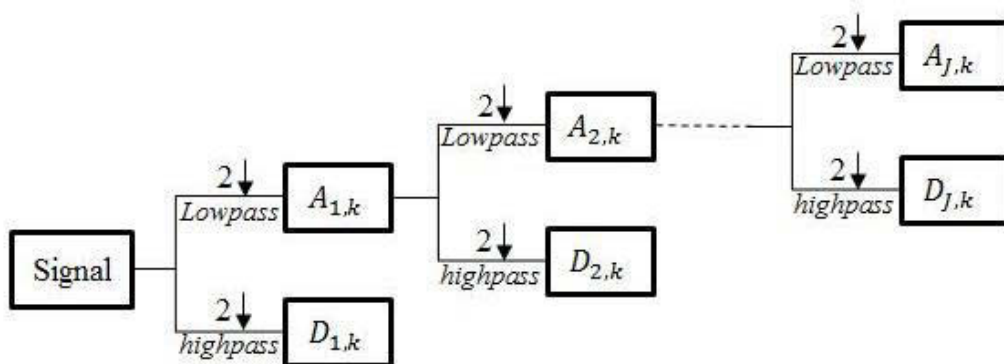


Figure 2.5 Implementation of the DWT in terms of filter banks (the downward arrow indicates down-sampling by a factor of two) (Percival and Walden, 2006).

Figure 2.6 is an example showing a signal is decomposed to level 3 with the DWT, which we can summarize as below.

- a) Detail coefficients (cD_i) store high-frequency features of the signal; and approximation coefficients (cA_i) show low-frequency components of the signal.
- b) Higher decomposition level means larger scale value; features extracted from the signal or the approximation coefficients of the previous level to the detail coefficients have lower frequencies, and vice-versa.

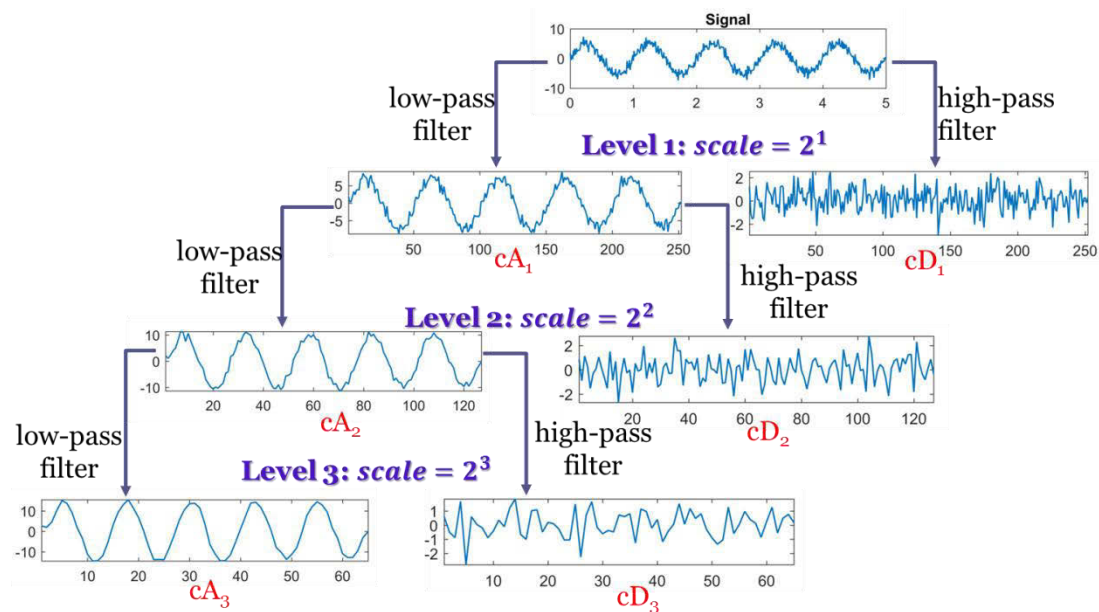


Figure 2.6 A signal is decomposed to level 3 with the DWT.

2.1.3 Selection of a wavelet

There is a number of wavelet families, such as Haar, Daubechies, Symlets, Coiflets, Biorthogonal, Meyer, Gaussian, Mexican hat, Morlet, Shannon, Frequency B-Spline, Complex Morlet and Fejer-Korovkin wavelets (see wavlet Toolbox of MATLAB). Users have to decide first which wavelet is suitable for their application: CWT or DWT. If the goal of the application is to perform a detailed time-frequency analysis,

then the CWT is a good choice; however, if the application is about general denoising, compressing, or feature detecting, DWT is superior to CWT (<https://www.mathworks.com/help/wavelet/gs/continuous-and-discrete-wavelet-transforms.html>). As already mentioned, the CWT provides a highly redundant representation of a signal, the cost of computing and storage of CWT coefficients is much greater than for the DWT. A detailed comparison between the CWT and the DWT can be found in the documentation of wavelet transform in Matlab.

Unfortunately, there is no straightforward method to choose an appropriate wavelet. In fact, the characteristics of the signal and the purpose of the application influence which wavelet should be used. We summarized some general rules from the documentation of the wavelet toolbox in Matlab:

- a) In time-frequency analysis, analytic wavelets, such as generalized Morse wavelet, analytic Morlet wavelet, and bump wavelet, are a good choice.
- b) If the application requires preserving the energy of the signal, an orthogonal wavelet must be used, because orthogonal transforms preserve energy. In this case, wavelets like coiffet, daubechies, and haar are a good choice.
- c) Although orthogonal wavelets are most commonly used, the wavelet's orthogonality restricts the type of decomposition and reconstruction filters. Non-orthogonal transforms, on the contrary, have fewer restrictions on the type of filters; therefore, filters with finer frequency resolution are available (Fargues *et al.*, 1997). So if a high resolution in the frequency domain is needed for the application, non-orthogonal wavelets can be considered.
- d) To detect features, the support, which indicates the non-zero interval of a wavelet, must be chosen accordingly: small support for closely spaced features. Wavelets with large support can be used if features in the signal are sparsely spaced.

- e) In case of compression, consider using biorthogonal wavelets. Biorthogonal wavelets are symmetric and have linear phases. They have two pairs of scaling function-wavelet: one pair is for analysis, and the other one is for synthesis. This feature of biorthogonal wavelets is very useful in compressing an object.
- f) If the application is to denoise signals, orthogonal wavelets are a good candidate. An orthogonal transform preserves energy and does not color white noise.

Although the choice of basic wavelet types can be guided by these guidelines, there is no concrete criterion for us to choose a specific wavelet for a specific application. Proceeding by trials and errors is the only way. We tried a lot of wavelets in our study, such as the harr wavelet, the daubechies wavelet family, and the symlet wavelet family. Finally the ‘sym5’ wavelet of the symlet wavelet family is chosen in our study (details are discussed in Chapter IV).

2.2 Complementary methods

Our denoising method development begins with synthetic signals and known noise. After using DWT to process the synthetic signal, in some cases we have observed that there are still residual perturbations remained. Since in a time-domain geophysical survey, as borehole transient electromagnetic measurement (BHTEM), the secondary magnetic field (B) and/or its time rate (dB/dt) is recorded after the primary electric field disappeared, the decay of the secondary magnetic field is often estimated by an exponential function (Equation 2.17) (Nabighian and Macnae, 1991). The importance is that the decay time constant is reverse to the exponential decay constant. Larger decay constant (small time constant) makes the transient signal vanish much more rapidly than small decay constant (large time constant); and the time constant is one of important characteristics used in the mineral exploration to discriminating good or bad conductor. A stable decay can ensure a good estimation of

the time constant. Therefore, the residual perturbation in the signal can lead to misinterpretation of data. In order to further improve the data quality, we introduce a curve fitting method dedicated to simple data sets, perhaps mostly for theoretical tests purposes.

For a practical time domain electromagnetic (TEM) survey, the measurement is often repeated many times at each survey point. The correlation method is therefore further developed to eliminate residual random noises. Those two methods are described below.

2.2.1 Curve fitting technique (CFT)

Although the induced polarization (IP) effect is always present in all electromagnetic (EM) surveys when polarizable minerals, such as clays, massive and disseminated sulphides, are present; however, the IP signal is low and completely overlapped with the inductive effect. In addition, Smith and West (1989) pointed out that the in-loop EM system is the optimal configuration to excite the airborne IP response including negative transients in mid to late times over resistive grounds, from bodies of modest chargeability under condition of layered structure or homogenous half space. The fact that the most of borehole EM surveys use out-off loop EM system, and whole space and highly inhomogeneous milieu are involved. It is impossible to characterize the IP effect in borehole EM (personal communication with senior geophysicists of companies), therefore, we ignore IP effect on exponential transient decay model in this study. We apply the exponential function below as our model to implement the fitting process to reduce the residual perturbation after DWT process.

$$s(t) = \alpha e^{-t/\tau}, \quad (2.17)$$

where α and τ are parameters to be determined. They denote the gain parameter and the time constant of the conductor, respectively. They are calculated according to the linear least-squares criterion. Take the natural logarithm of both sides of Equation (2.17), we got:

$$\ln s(t) = \ln \alpha + \frac{1}{-\tau} t. \quad (2.18)$$

Let $y = \ln s(t)$, $p_1 = \ln \alpha$, and $p_2 = \frac{1}{-\tau}$, then we have

$$y = p_1 + p_2 t. \quad (2.19)$$

Suppose \tilde{y} is the fitted data, then the residual of the i^{th} ($i=1,2,3,\dots,n$) data is defined as

$$r_i = y_i - \tilde{y}_i = y_i - (p_1 + p_2 t_i). \quad (2.20)$$

Sum the square of residuals of all data, we got

$$S = \sum_{i=1}^n r_i^2 = \sum_{i=1}^n (y_i - (p_1 + p_2 t_i))^2. \quad (2.21)$$

Because the purpose of the least-square process is to minimize S , the parameters to be determined are solutions of the equation set formed by differentiating the Equation (2.21) with respect to each parameter, and setting the result to zero:

$$\begin{aligned} \frac{\partial S}{\partial p_1} &= -2 \sum_{i=1}^n x_i (y_i - (p_1 x_i + p_2)) = 0 \\ \frac{\partial S}{\partial p_2} &= -2 \sum_{i=1}^n (y_i - (p_1 x_i + p_2)) = 0 \end{aligned} \quad (2.22)$$

Solve equation set (2.22):

$$\begin{aligned} p_1 &= \frac{n \sum_{i=1}^n x_i y_i - \sum_{i=1}^n x_i \sum_{i=1}^n y_i}{n \sum_{i=1}^n x_i^2} \\ p_2 &= \frac{1}{n} (\sum_{i=1}^n y_i - p_1 \sum_{i=1}^n x_i) \end{aligned} \quad (2.23)$$

Therefore we get the two unknown parameters in Equation (2.17):

$$\begin{aligned} \alpha &= e^{p_1} \\ \tau &= -\frac{1}{p_2} \end{aligned} \quad (2.24)$$

To constrain the fitting result, perturbed segments in the data are identified and excluded from the fitting process. These segments are determined through the following steps:

1. Find extrema. The perturbation of signal represents local peaks or valleys in the data. The first step is to determine the location of these extremes on the decay curve.
2. The width of each peak and valley is then estimated by its half-prominence. The prominence of a peak measures how much the peak stands out due to its intrinsic height and its location relative to other peaks (Source: Matlab). All these parameters can be easily obtained by using the built-in function *findpeaks* in Matlab. Figure 2.7 explains how to decide the prominence of a peak.

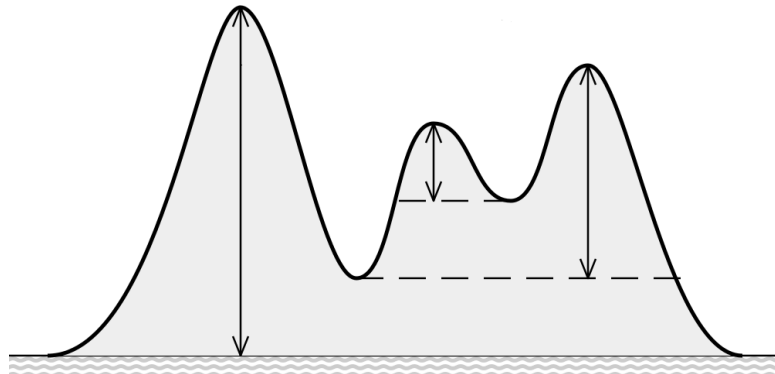


Figure 2.7 Definition of the prominence of a peak. Vertical arrows indicate the prominence of the peak. (source: https://commons.wikimedia.org/wiki/File:Prominence_definition.svg)

3. Exclude points from the fitting process. Points fall within the range of half-prominence of the peak are considered as being contaminated by residuals, thereby excluded from the fitting process and replaced later by values from the fitting result.

The following example shows how this method is implemented. Figure 2.8 presents the result of denoising with the DWT, but perturbations caused by noise residuals still exist in the result. In order to use the fitting method, we first find out the peaks/valleys in the denoised signal as shown in Figure 2.9. the width of these peaks/valleys can be estimated with the help of half-prominence. To reduce their impact on the fitting result, points fall in range of half-prominence around the peak/valley are excluded from the fitting process. Figure 2.10 shows the CFT smoothes the perturbations caused by noise residuals effectively.

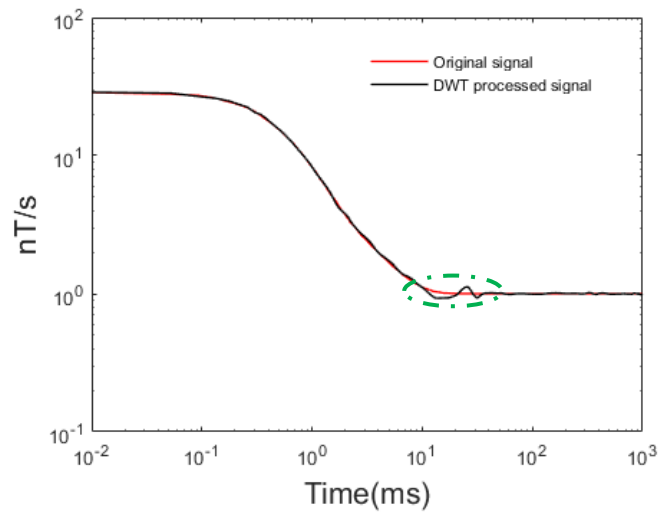


Figure 2.8 Perturbations exist in the result of denoising with the DWT

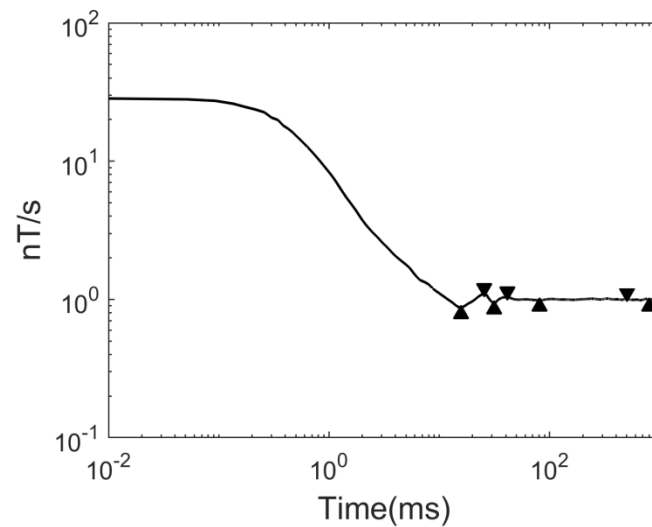


Figure 2.9 Peaks/valleys located in the DWT denoised signal.

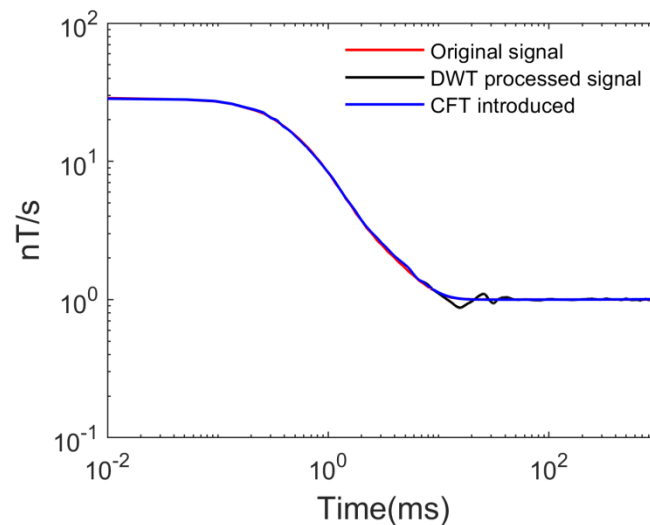


Figure 2.10 Comparison between the DWT denoised result and DWT+CFT processed result.

2.2.2 Correlation analysis and stacking

Generally, in a BHEM field survey, the measurement is repeated many times at each survey point. Then, these measurements are stacked into one record in an effort to eliminate random noise. Since repeated measurements are at the same survey point,

they are basically recording signals from the same source. The response of geological bodies to primary electromagnetic fields will not change in repetitive measurements, but random noises will change. As we mentioned in section 1.3, during the measurement of BHTEM the sensor may rotate and/or vibrate because of the liquid flow or obstacles in the borehole. This rotation and/or vibration will be one type of source of noises to the measurement. Using conventional stacking methods one can reduce random noise, but when there is an acute noise signal, it can skew the neighboring data. This is why we first use DWT method to process the raw data, and then do correlation analysis in order to distinguish the geological response versus noises.

Figure 2.11 illustrates a cycle of recording in TEM method. A cycle includes four transients: two on-time transients and two off-time transients.

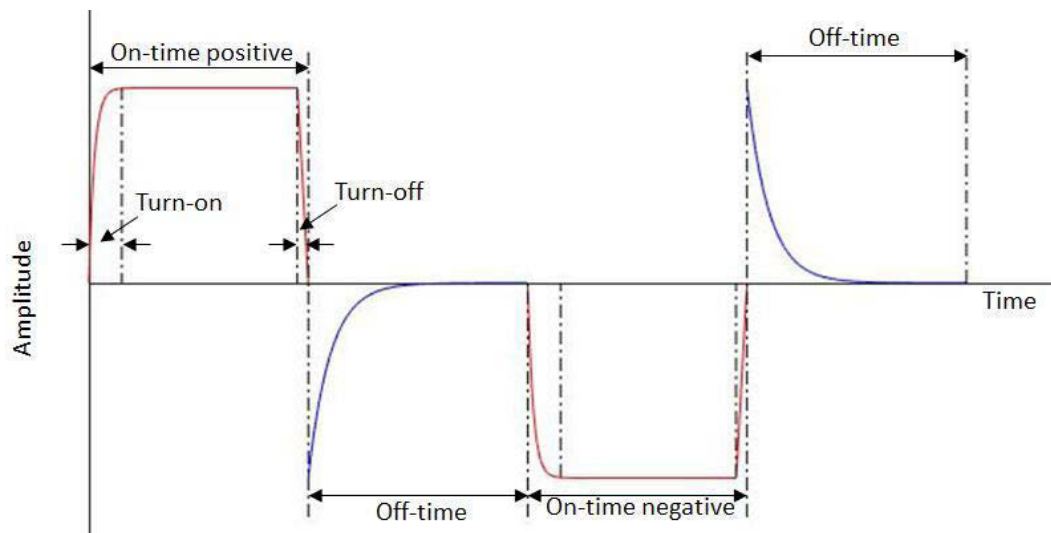


Figure 2.11 Basic principles of measurement of the TEM method. The red line indicates the current in the transmitter loop, and the blue line shows the signal recorded by the sensor.

Based on this recording mechanism, we can use correlation to identify the distorted transients. The Pearson correlation coefficient is chosen because of its invariance, i.e., the coefficient is not affected by separate changes in the two variables in location and

scale. For example, if one variable X is changed to $\alpha X + \beta$, and another variable Y is changed to $\lambda Y + \gamma$, where α , β , λ , and γ are constants, and $\alpha, \lambda > 0$, the correlation coefficient will not be changed. The coefficient between two variables X and Y is calculated by the formula:

$$\rho_{X,Y} = \frac{cov(X,Y)}{\sigma_X \sigma_Y}, \quad (2.18)$$

where, $cov(X, Y)$ calculates the covariance between variables X and Y ; σ_X and σ_Y is the standard deviation of X and Y , respectively.

The correlation coefficient calculated by equation (2.18) ranges from -1 to 1. The value of 1 means there is a perfect linear relationship between the two variables. The value of -1 implies that the two variables still have a linear relationship, but they change in an opposite direction, in other words, one variable decreases as the other one increases. When the correlation coefficient equals to zero, there is no linear correlation between the two variables. For example, if we have a five-transients record, and we compute the Pearson coefficients between them. We will get a diagonal matrix shown in Table 2.1. From these values we can conclude that the transient-2 has a bad correlation with other transients, it must be distorted.

Table 2.1 Pearson coefficients between five transients.

transient	1	2	3	4	5
1	1.00	0.65	0.95	0.94	0.99
2	0.65	1.00	0.68	0.70	0.64
3	0.95	0.68	1.00	0.97	0.98
4	0.94	0.70	0.97	1.00	0.92
5	0.99	0.64	0.98	0.92	1.00

After the distorted transient is identified with the help of correlation analysis, it is replaced by linear interpolation using other transients. Figure 2.12 shows the distorted transient (red line) is replaced by interpolation (dashed blue line). The interpolation is carried out sampling by sampling, i.e., we first take the first sampling of each

transient which is not distorted to do a linear interpolation to get the first sampling to replace the first sampling of the distorted transient. Then we repeat this process on other samplings until the entire distorted transient is replace.

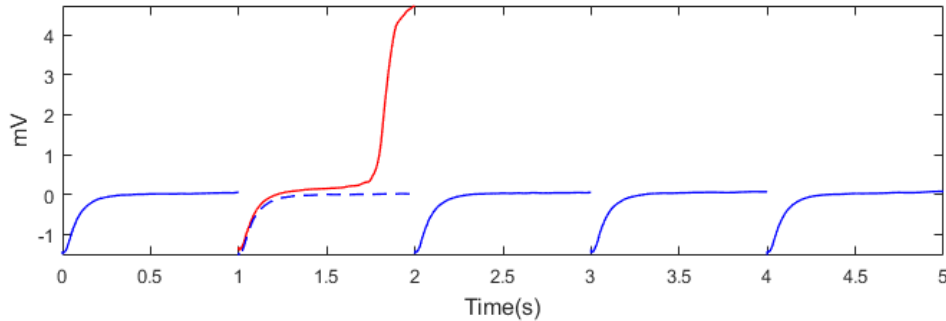


Figure 2.12 Schematic diagram illustrating the process of replacing distorted transient with interpolation.

2.2.3 Stacking

Stacking is a fundamental and essential step in time series of geophysical data processing. The goal of stacking is to improve the signal-to-noise ratio. After decades of development many stacking techniques have been developed. The most simple one is the average stacking method. For each survey point, it adds up all isochronous values and the sum is then divided by the number of values to get the stacked results, as defined by Equation (2.19):

$$A_t = \frac{1}{N} \sum_{k=1}^N a_i. \quad (2.19)$$

A_t is the stacked result of channel time t . And a_i is the sample value of the i^{th} measurement of the corresponding channel. N is the total repeated measurement times. In this stacking method a uniform weight is used for all measurement. This makes the method very easy to understand and to use, but it cannot be used to deal with data with drift. To remove linear drift Mark Halverson developed a method called Halverson stacking in 1960s. Three half periods are engaged each time in the stacking process (Kingman et al., 2004), and weights for these three half periods are:

$\frac{1}{4}, -\frac{1}{2}, \frac{1}{4}$. So, if there are four half periods in the data set, then the weight for each half period can be decided as follows (Kingman et al., 2004):

$$\begin{pmatrix} \frac{1}{4} & -\frac{1}{2} & \frac{1}{4} \\ + & -\frac{1}{4} & \frac{1}{2} & -\frac{1}{4} \end{pmatrix} \cdot \frac{1}{2} = \begin{bmatrix} \frac{1}{8} & -\frac{3}{8} & \frac{3}{8} & -\frac{1}{8} \end{bmatrix}. \quad (2.20)$$

Weights for data set with more half periods can be obtained similarly. A general formula for weights when there are more than four half periods in the data set is below (Kingman et al., 2004):

$$\frac{[1, -3, 4, -4, 4, -4, \dots, 4 \cdot (-1)^{n-3}, 3 \cdot (-1)^{n-2}, 1 \cdot (-1)^{n-1}]}{4 \cdot (n-2)}, \quad (2.21)$$

where, n is the total number of half periods in the data set.

The Halverson stacking method is used in this study. To compare the results stacked from different raw data (original raw data, DWT denoised raw data, and DWT denoised plus distorted transients corrected raw data), we will use Halverson stacking in our study.

CHAPTER III

CHARACTERISATION OF EM NOISES IN DEEP MINING TUNNELS

3.1 Introduction

Every geophysical datum consists of two parts: information related to the target, and all other regarded as noise. Commonly encountered noise sources in EM measurements can be categorized as man-made noise and natural noise.

On surface, man-made noises come mainly from power distribution grid. The frequency of this kind of noise is usually highly stable and its features are easily determined. By contrast, the natural noise is much more complicated and difficult to remove. One major source is sferics, and it is not uniformly distributed throughout the measurement bandwidth but typically concentrated in the high frequency part (Macnae *et al*, 1984). Energy in the 5 Hz – 25k Hz range is primarily due to sferics, which are natural transients generated by lightning discharges; and the natural EM noise below about 6 Hz is mainly of geomagnetic and ionospheric origin. In addition, natural noise fields may change from place to place and from time to time, and therefore are more difficult to handle. Toward the Earth interior but near the surface, the conductive overburden in the survey area has a strong effect on the EM field (Macnae *et al*, 1984). It may greatly weaken the penetration of electromagnetic waves. Deep in underground tunnels, the shielding effect of the rock formation may reduce the noise effects of some electromagnetic fields on the ground; however, due

to the difficulty of entering the underground tunnel, there is a lack of understanding of the noise in such deep environment. Thanks to the financial support of the FRQNT (Fond de Recherche Naturel et Technologies du Québec), our industry partner (LaRonde Mine of Agnico Eagle) allowed us to install 5 electromagnetic signal recorders at 5 places in 3km deep underground tunnels. Those five places represent typical deep mining environment, quiet and noise-concentrated areas (detailed information in Table 3.1). This chapter aims at the characterization of underground recorded EM signals.

3.2 A brief description of LaRonde Mine

At about 47 kilometers east of Rouyn-Noranda City, the LaRonde Mine is an Au-rich volcanogenic massive sulfide (VMS) deposit. The deposit is a huge subvertical tabular of east-west orientation. It was first discovered in 1976 by Dumagami Mines Ltd., and first achieved commercial production in 1988. It is now fully owned by Agnico Eagle Ltd. Among the ten deepest mines in the world, the LaRonde deposit is one of the most important VMS deposits hosted in the Abitibi greenstone belt, and it is the largest Au deposit currently mined in Canada (Mercier-Langevin *et al.*, 2007). The mine has produced more than 5 million ounces of gold along with valuable by-products and still has 2.6 million ounces of gold in proven and 15 million tonnes grading 5.39 grams of gold per tonne probable reserves as of the end of 2017 ([Agnico Eagle website](#)). The production of the mine now mainly comes from deep ore bodies; and the exploration is directed toward great depth and the periphery as shown in Figure 3.2.

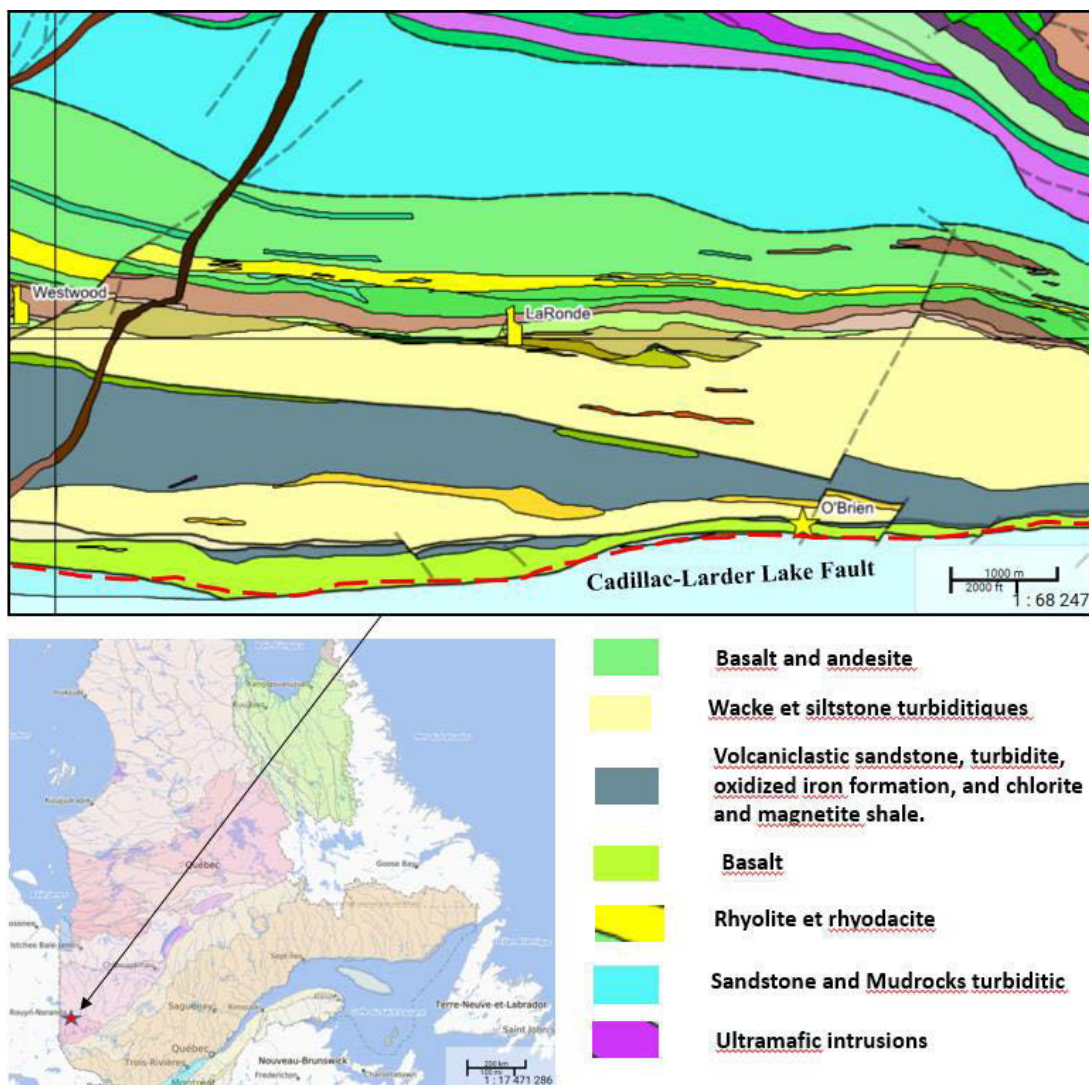


Figure 3.1 Geological map and location of the LaRonde mine (Source : modified from interactive carte of SIGEOM, MERNQ, http://sigeom.mines.gouv.qc.ca/signet/classes/I1108_afchCarteIntr).

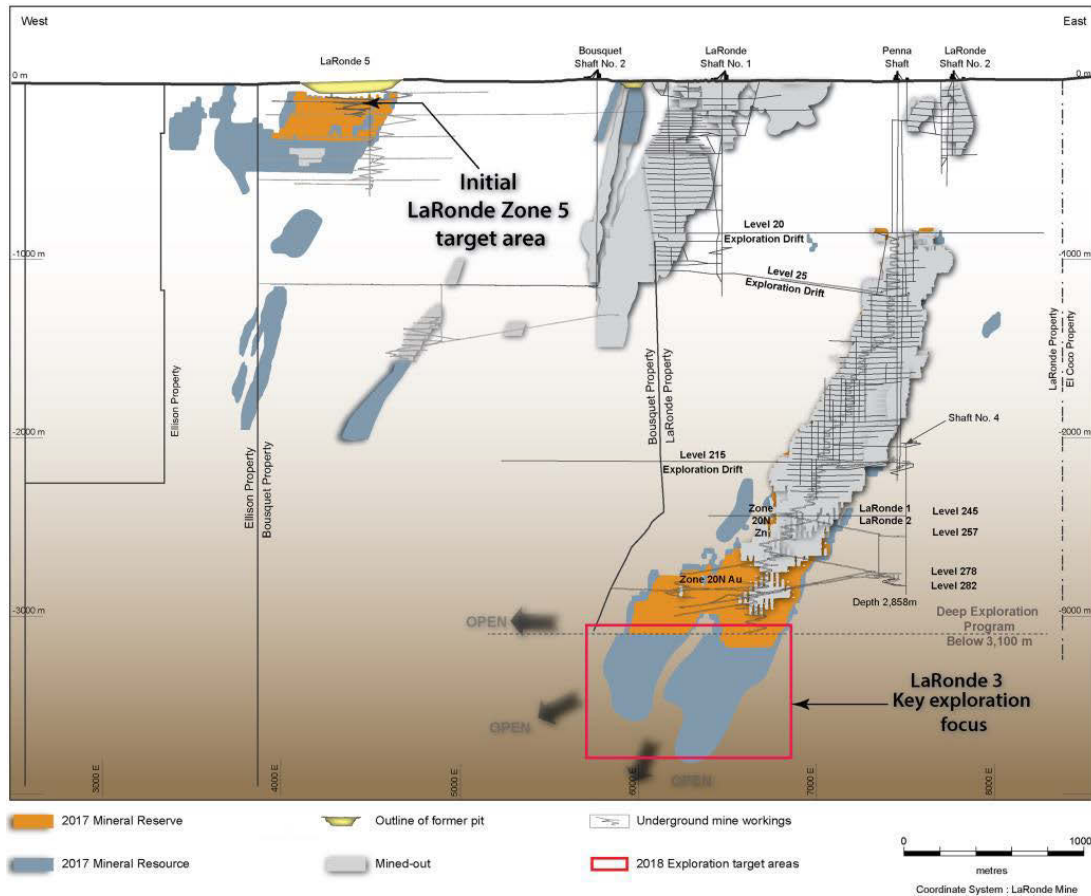


Figure 3.2 Composite longitudinal section of the LaRonde mine (Source : <https://www.agnicoeagle.com/English/operations-and-development-projects/operations/laronde/maps-and-surveys/default.aspx>).

3.3 Geological setting of LaRonde Mine

The LaRonde mine is located near the southern boundary between the Abitibi Sub-province and the Pontiac Sub-province, within the Superior Province of the Canadian Shield (Gosselin, 2005). It is about 4km in the north of an important regional geological structure – the Cadillac-Larder Lake Fault (CLLF), which is indicated as the broken red line in Figure 3.1.

During late Archean orogenesis, accompanied by large-scale north-south compression and dextral transpression tectonic events (Card 1990), the lithological sequences near

the CLLF were sub-verticalized, dipping toward the south. From the north to the south three geological formations around the LaRonde Mine are: (1) the Kewagama Group formed by thick band of interbedded wacke; (2) Blake River Group, which is a volcanic assemblage and the host of all known economic mineralisation of the LaRonde mine; (3) the Cadillac Group which is made up of thick band of wacke interbedded with polytropic schist and minor iron formation (Gosselin, 2005).

The key question for the future development of the LaRonde Mine is: how much economic minerals remain unexploited under the depth of 3km? Where comes out the importance to do some geophysical surveys in order to estimate the mineral potential around known mineralization. Among conventional geophysical methods, the time domain electromagnetic method is widely applied to explore volcanogene massive sulfides minerals. One of the important factors affecting the efficiency of this method is the ratio of the signal to noise. Several potential noise sources could exist in a deep mine, such as Schumann resonance (7.83 Hz) ; VLF (Very low frequency) (3 – 30 kHz); EM field resulted from coupling between machine vibration and EM field (attenuate quickly with distance) ; power lines (between 50 and 60 Hz) and communication cables (high frequency), but we lack of knowledge on them, especially in an active deep mining environment. We therefore decided first to record noises in deep tunnels of the LaRonde mine.

3.4 Data acquisition

3.4.1 Zonge Electromagnetic Network (ZEN) receiver

The device we used to collect data in the tunnels of the LaRonde mine is Zonge Electromagnetic Network (ZEN) receiver (Figure 3.3), which is a product of Zonge International Inc. ZEN receiver is a broadband, high-resolution, and multi-function digital receiver for acquisition of controlled- and natural-source geo-electric and EM data. It has up to 6 channels and it is expandable. The frequency range of the receiver is from DC up to 1024 Hz. The device is small in size ($27 \times 24 \times 13$ cm) and very

light (3Kg with 6 channels, without battery and meter/connection panel) (source :. <http://zonge.com/instruments-home/geophysical-data-acquisition-systems/distributed-em-systems/>). The magnetic sensor we used in this survey is ANT/6 of Zonge International Ltd. The sensor uses feedback amplifier technology and including carefully designed mu-metal cores. It is a multipurpose coil with low noise level: $100 \mu\gamma$ ($100 fT$) per \sqrt{Hz} at 1 Hz, $100 \mu\gamma$ ($100 fT$) per \sqrt{Hz} nominal >1 Hz. The length of the sensor is 91.0 cm, and its diameter is 4.8 cm. The weight of the sensor is around 3.2 kg. The frequency range of the sensor is 0.1—10240 Hz (Source: <http://www.zonge.com/legacy/MagSensors.html>).



Figure 3.3 The Zonge Electromagnetic Network (ZEN) receiver (Source: Zonge International Inc.).

3.4.2 Sites of recordings

With the help from geologists of LaRonde Mine, five representative places have been chosen at 3000 m depth. They are: 1) in a relatively quiet area (site #1); 2) near a conveyor, and under a crusher, which crushes large minerals (site #2); 3) near the massive sulfide mineralization zone and a loading station (site #3); 4) under the power supply center (site #4); and 5) beside a drilling site (site #5). These sites are indicated as circled numbers in Figure 3.4. The characteristics of the sites are summarized in Table 3.1.

Table 3.1 Description of all recording sites. The five sites are all located in the tunnels at 3000m depth.

site	description	Start time (Apr 12, 2018)	End time (Apr 13, 2018)	Total recording time	Sampling rate
1	No mining activity	09:40AM	07:56AM	22h 16m	1024
2	Nearby a mineral conveyor Crusher above	10:11AM	08:22AM	22h 11m	1024
3	Nearby a loading station	10:51AM	08:56AM	22h 05m	1024
4	Under a power station	11:29AM	09:19AM	21h 50m	1024
5	Nearby a drilling site (Less than 50m)	11:47AM	09:49AM	22h 02m	1024

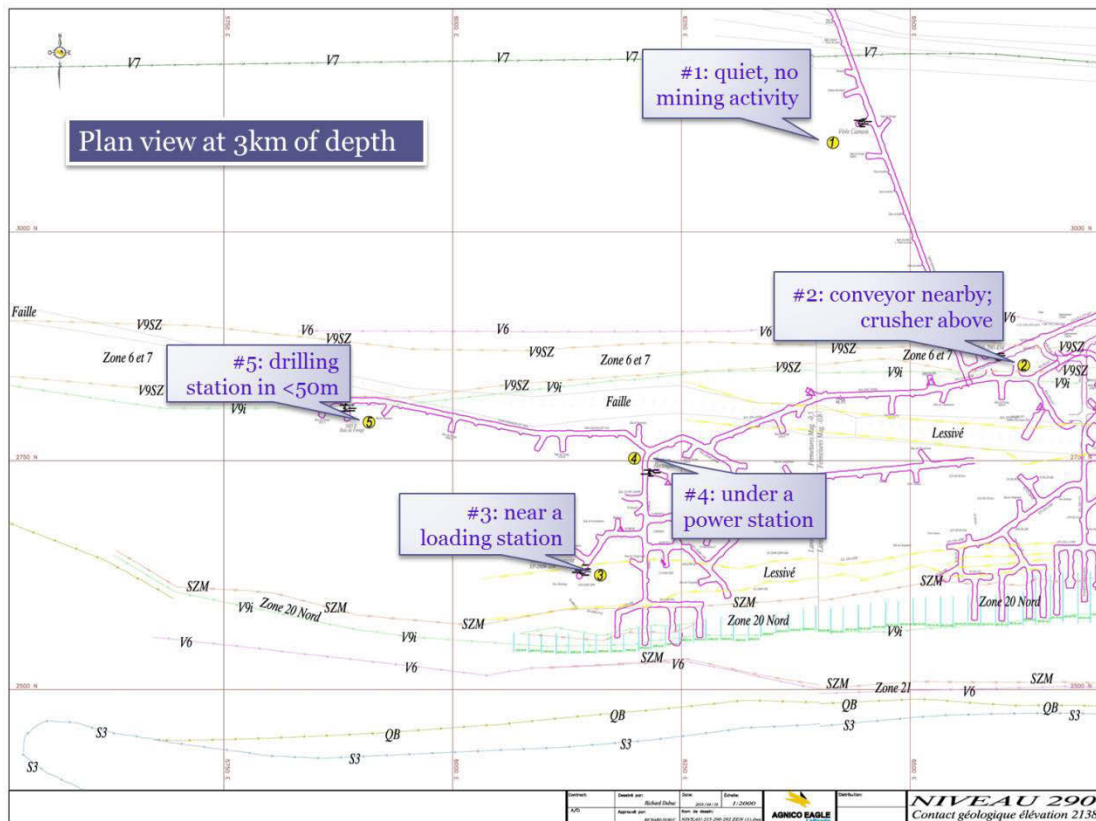


Figure 3.4 Locations of the five data acquisition sites (scale: 1:2000).

3.4.3 Recorded signals

There are 6.11 gigabytes electromagnetic data recorded during more than 22 hours. For better associating changes in the EM signals with underground mining activities, the operation period of mining equipment (drilling, crusher, and conveyor etc.) is considered. Operation hours for the drilling site that is near the data acquisition site #5 are from 08:00:00 to 15:00:00 on April 12, 2018, and from 20:00:00 on April 12, 2018 to 03:00:00 on April 13, 2018. In addition, Figure 3.5 tells the electrical current variations in the conveyor near the data acquisition site #2. All data acquisition sites were blocked for the measurement, therefore no traffic presented at all sites during the period of recording. Two blasting events took place between 17:43:28.992 and 17:43:37.661, 05:19:24.873 and 05:19:34.437. The first blast happened near 380 m above site #2, while the 2nd is 50 m in the East-North of site #2. However, we do not

have GPS signal in the tunnels; therefore, all recordings are not synchronized. Consequently, not only did the five receiver start and end recording at different time, but each channel of a specific receiver had different start and end time. We have not yet found an appropriate way to locate such a short period of time in our recordings. These blasts are thus not considered as a noise source.

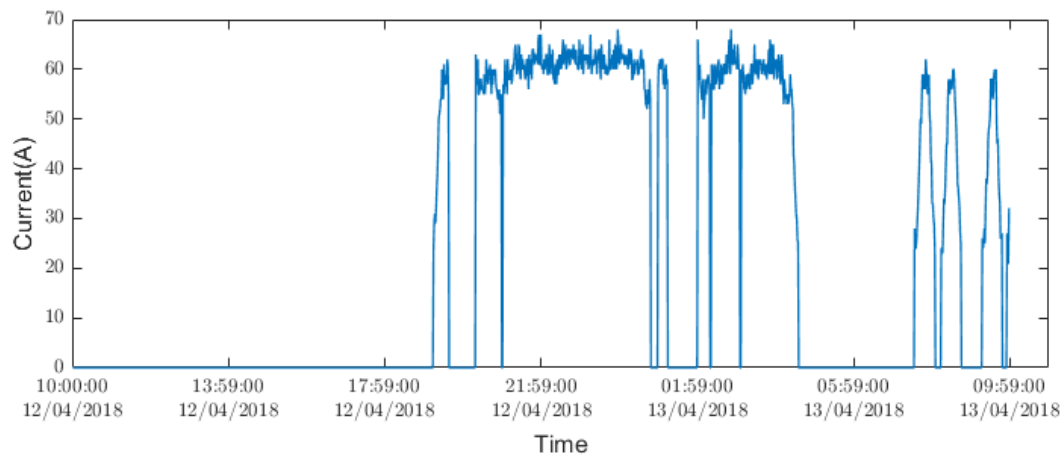


Figure 3.5 The current in the conveyor varies with time.

3.5 Recorded time series

At each site, four components of electromagnetic field are recorded. They are: the horizontal electric field (E_x and E_y), and magnetic field (H_x and H_y).

Figure 3.6 and Figure 3.7 present time series from all acquisition sites. The behavior of the electric components is a bit abnormal. Since noises are not polarizable, which means they are mostly random distributed (Gaussian distribution), the average value should be around zero, like we have observed in magnetic field components (H_x and H_y). In addition, the behavior of the E_x and E_y should be alike, as H_x and H_y , but it is not. The reason of these phenomena is not clear yet, they may caused by the self potential effect, which is usually a result of charge separation in some minerals, or natural flow of the conducting liquid through the rocks. In spite of these unusual

behaviors of E_x and E_y , we will still present analysis results of E_x and H_y in this chapter. But in future works, we will focus on the magnetic field components.

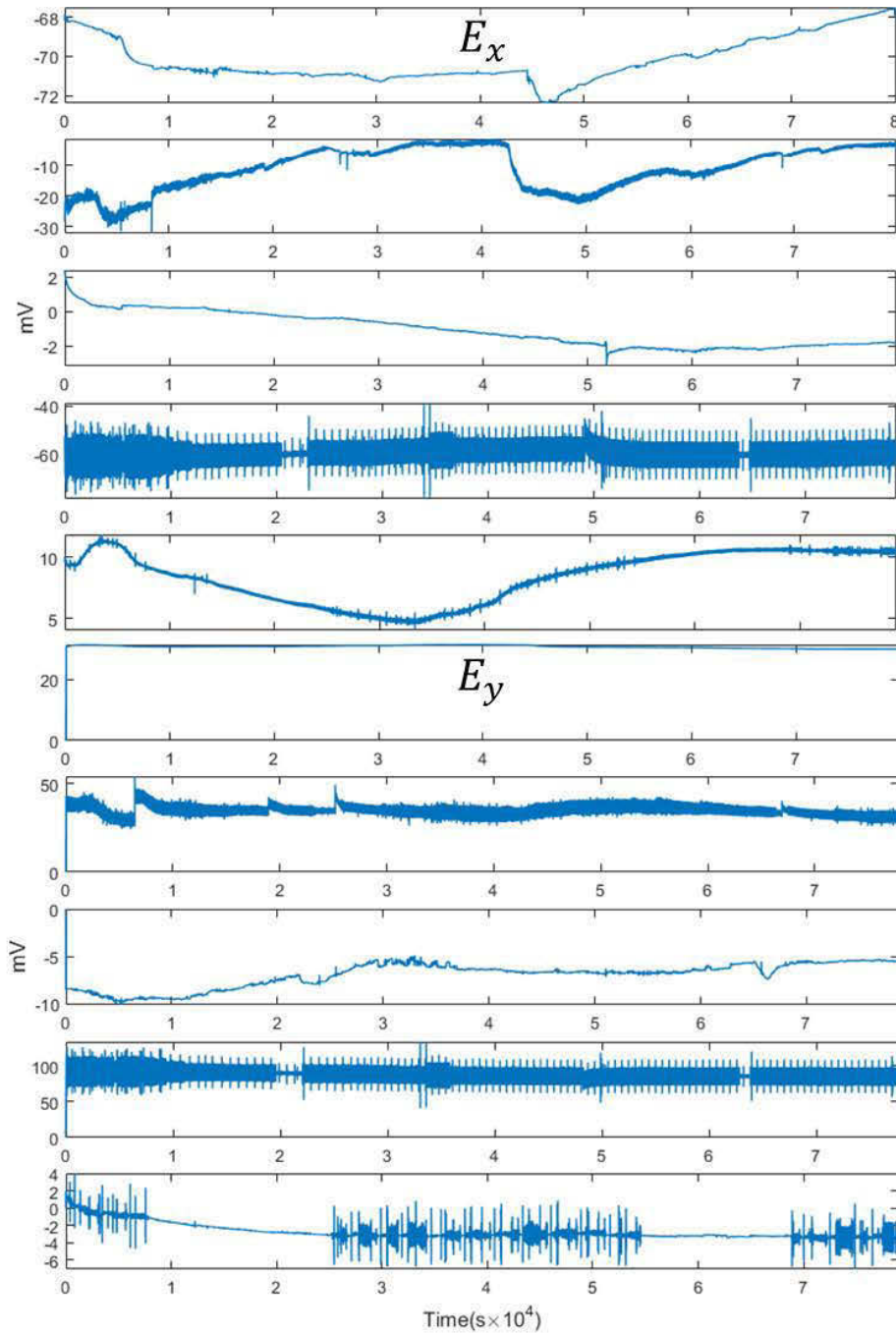


Figure 3.6 Electric components (E_x and E_y) from five acquisition sites. From top to bottom: site #1, site #2, site #3, site #4, and site #5.

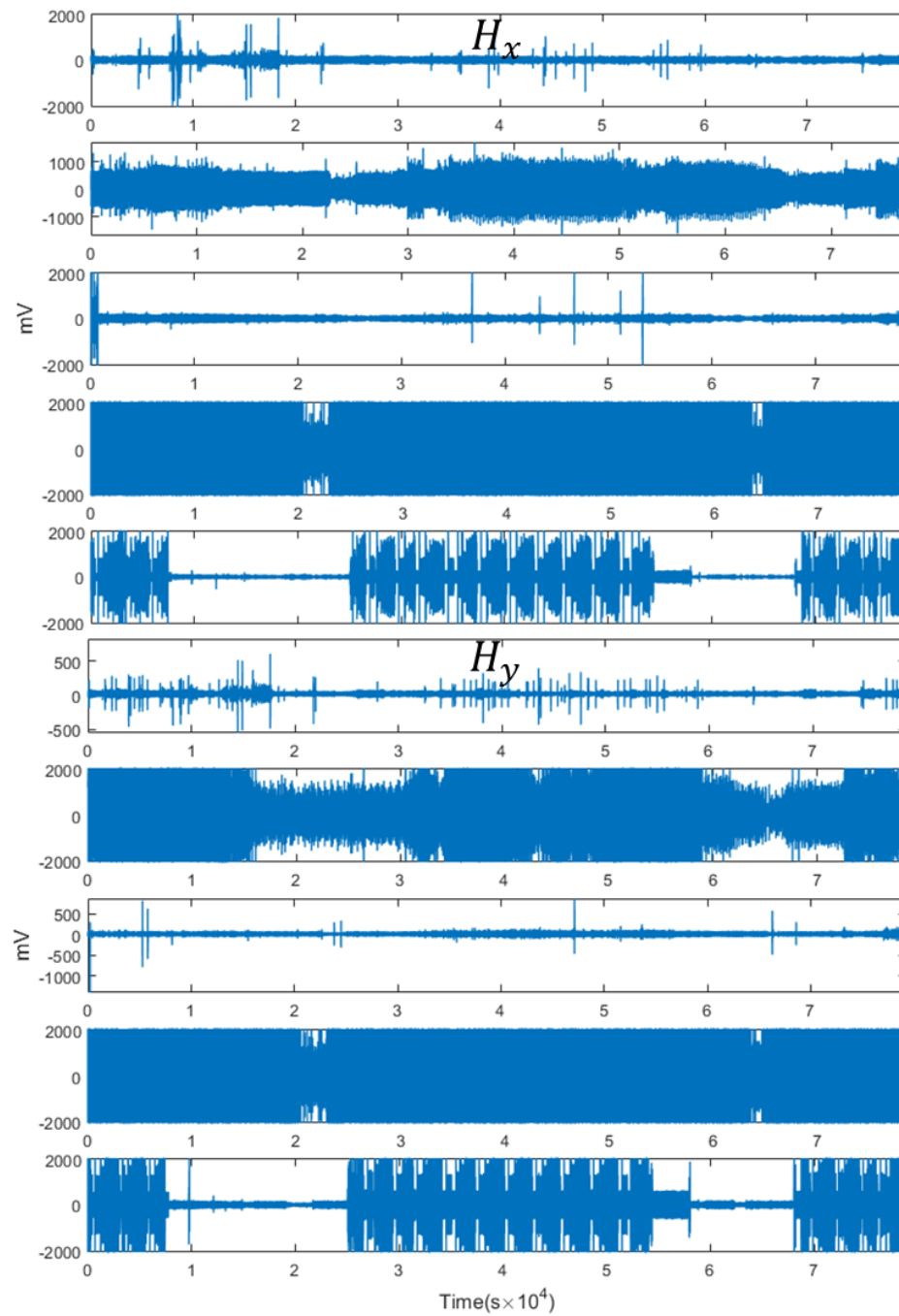


Figure 3. 7 Magnetic components (H_x and H_y) from five acquisition sites. From top to bottom: site #1, site #2, site #3, site #4, and site #5.

3.6 Data analysis

From these time series in Figure 3.6 and Figure 3.7, it is obvious that measurements at different sites suffer from different noises. To better understand these noise, data analyses are carried out using the FT and CWT. The purpose of using the FT to analysis these data is to characterize the frequency bands of noises from the mining activities. We use the CWT in an effort to extract more information about when a specific frequency noise occurs.

The computer used in the present study has a center processor unit of Intel Core i7-3770, 3.40 GHz with 24 GB RAM; the OS is entreprise edition windows 7 of 64 bits; no discrete graphic card. During the analysis with the CWT, we found that when the data volum is bigger than one minute of data (60×1024) the computer crashes easily. Due to limited computer resources and also on consideration of resolutions, two minutes of data are chosen from each recording (Ex and Hy) for following analysis. One minute of data is from the period where no mining related activity was in operation, while the other one minute of data is chosen from the period where mining related activities were present. These two minutes are: from 18:00:00 to 18:01:00 on April 12, 2018 indicating quiet period in terms of EM noise, and from 23:00:00 to 23:01:00 on April 12, 2018 indicating noisy period in terms of EM noise (see Figure 3.5). The latter corresponds to the drilling and crushing periods.

3.6.1 Analysis with the Fourier transform

Results of acquisition site #1: there is no mining machine around, this site is quiet in terms of EM noise.

For Ex, there is no significant difference in the FT results between the quite and noisy segments. But we have observed that the spectra of both segments decrease with frequency. For the magnetic field component Hy, apparent difference can be found in frequency range from 0.5 Hz to 20 Hz (circled out by a green ellipse in Figure 3.8). it

is impossible to guess the cause of this difference without witness. The 60 Hz signal is highlighted in both fields.

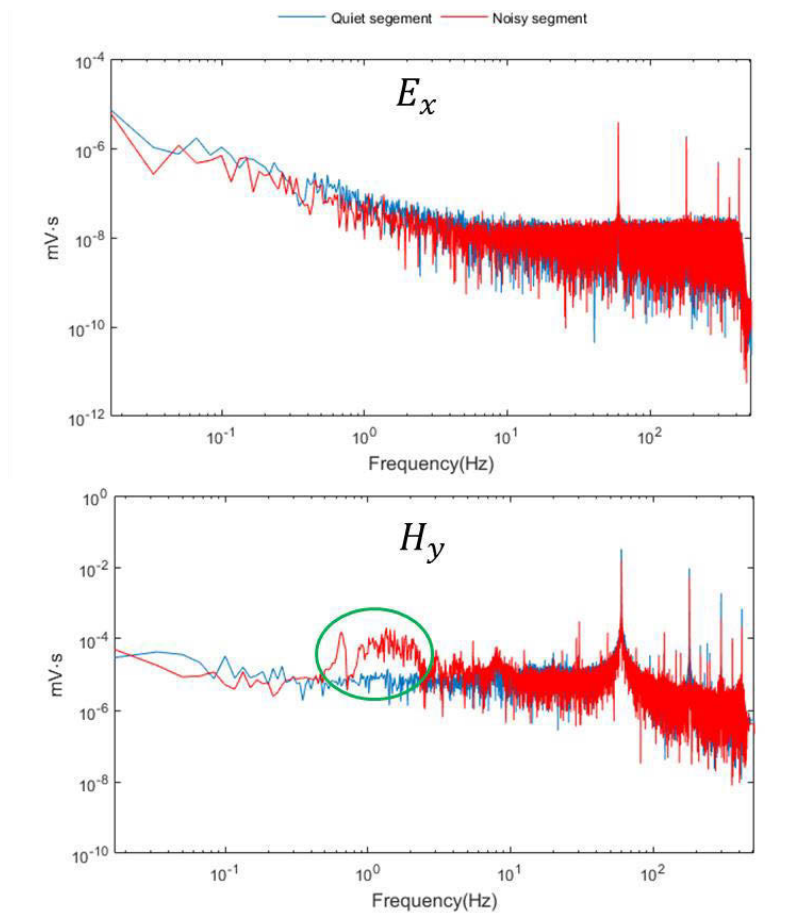


Figure 3.8 FT results of the two segments of the electric field component E_x and the magnetic component H_y at site #1.

Results of acquisition site #2: This site is near to a conveyor; and there is a crusher above. The noise level at this site should be affected by the operating status of the mining machine.

For the electric component E_x , we can see, in Figure 3.9, no matter the machine is operating or not the 60 Hz peak presents. This is understandable, because there is always alternative current of 60 Hz in the power lines no matter the machine is

operating or not. But when the machine is operating, in the spectrum segment of data corresponding to the time when the machine is operating, we observed another peak at around 7 Hz, indicated by the black arrow. And again, the spectra of both segments decrease with frequency. Again, the spectra decrease linear with frequency.

For the magnetic field component, we have not observed apparent difference between the spectra of these two segments of data. But the spectrum amplitude of the noisy segment is slightly bigger than that of the quiet segment. And the 60 Hz peak is detected in both segments.

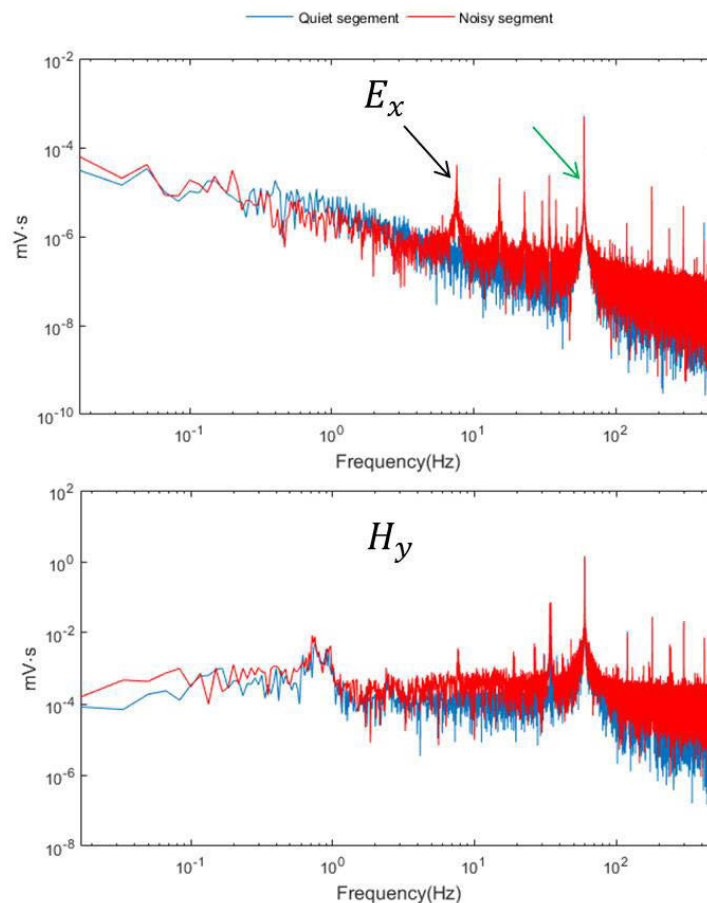


Figure 3.9 FT results of the two segments of the electric field component E_x and the magnetic component H_y at site #2.

Results of acquisition site #3: The environment situation of site #3 is similar to that of the site #1. The 60 Hz peak is detected in both segments of both E_x and H_y (Figure 3.10). The other apparent feature in H_y is the amplitude of the noisy segment is clearly bigger than that of the quiet segment.

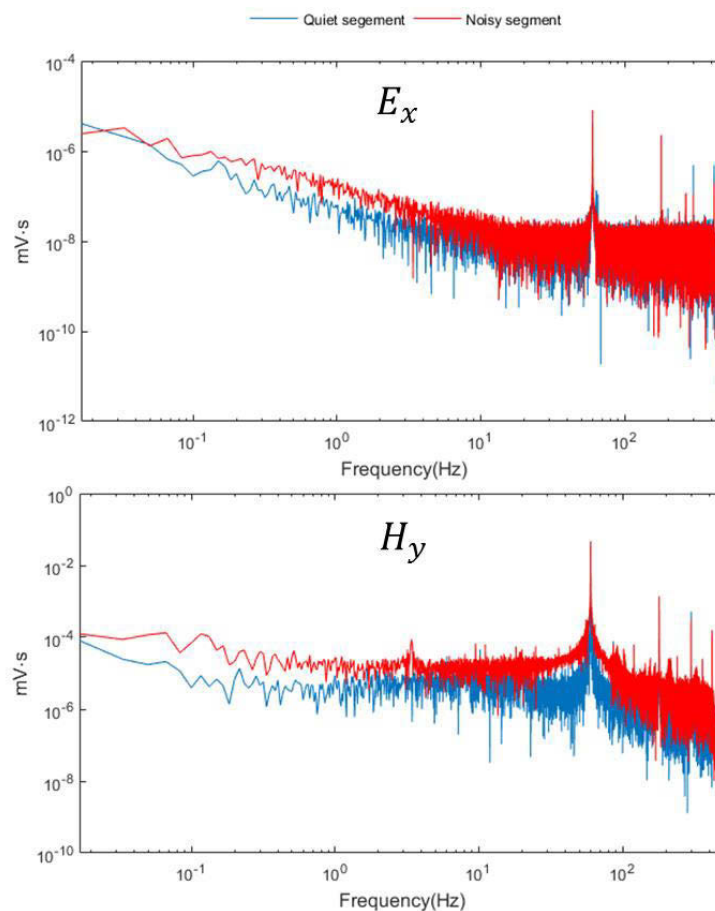


Figure 3.10 FT results of the two segments of the electric field component E_x and the magnetic component H_y at site #3.

The acquisition site #4 is the noisiest site of the five acquisition sites. There is not only a peak at 60 Hz, its amplitude is larger than other sites. Although the power station above the acquisition site is always working, there are differences between the two segments of signal. We speculate that the difference is caused by the change of

the output power of the station. When there is no mining related activity, the mining apparatuses are shutdown; as a result the output power of the station is lower; on the contrary, the mining apparatuses are operating; consequently, the output power of the station is higher. The reason of the abrupt change around 4 Hz in the FT result of the magnetic component H_y of the noisy segment in Figure 3.11 is not clear yet. Neither can any rational speculation be made here.

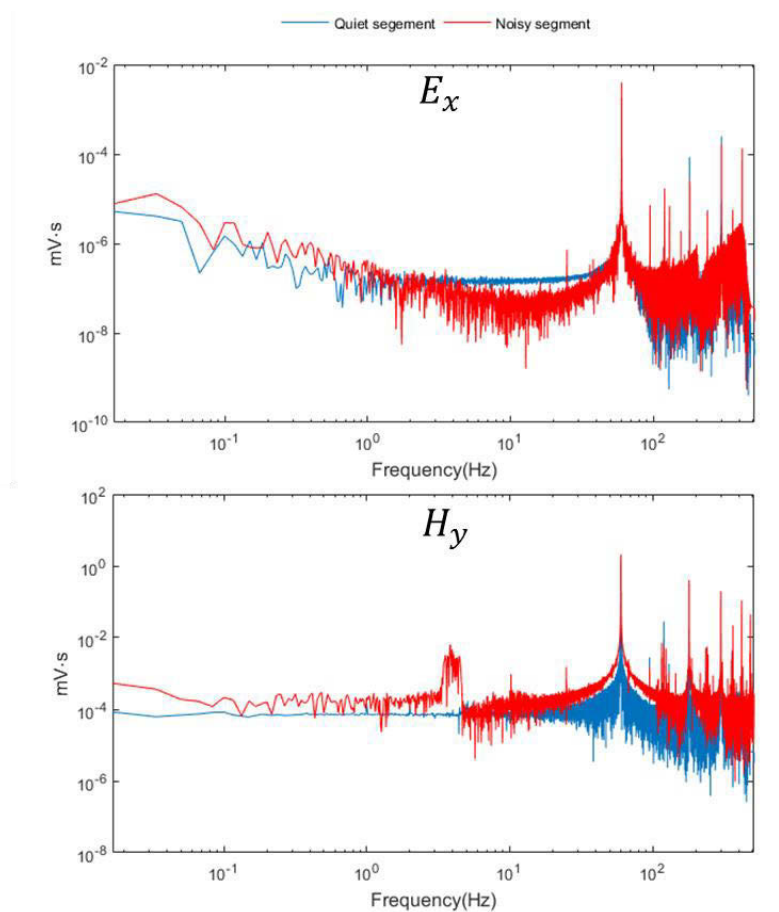


Figure 3.11 FT results of the two segments of the electric field component E_x and the magnetic component H_y at site #4.

For the results of acquisition site #5, the electric field component E_x is very similar to the site #3. We can see that the amplitude of the spectrum of the segment (red line),

which represents the period where the drilling site is operating, is slightly higher than that of the other segment (blue line). While, for the magnetic field component H_y , there are some distinctive features: for frequency range from DC (0 Hz) to 3 Hz, the FT result of the quiet segment has higher amplitude; when frequency is higher than 3 Hz, the FT result of the noisy segment has higher amplitude. This may imply the magnetic field component is more vulnerable to drilling activities.

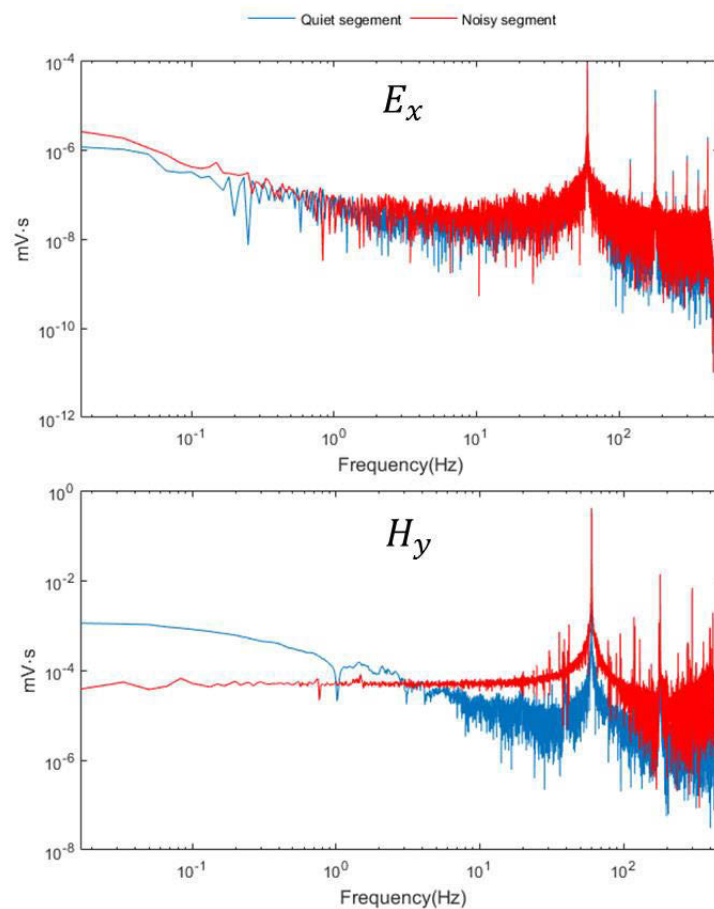


Figure 3.12 FT results of the two segments of the electric field component E_x and the magnetic component H_y at site #5.

Due to the fact that the sampling rate of ZEN is 1024, the highest frequency can be recorded in our survey is 512 Hz, therefore, high frequency noises come from

communication cables should be absent from our data. From above FT results, it seems not only 60 Hz is important in the recording but its harmonics. Obviously there is a background noise of low frequencies, therefore, further processing has been performed to remove random noises in order to better characterize the main noises related to the mining activities.

60 segments of length of one minute are randomly selected from both quiet and noisy period of measurement at site #2. The reason of choosing site #2 as an example is that the status of operation of the conveyor at this site is accurately recorded (see Figure 3.5). Spectra of these segments are calculated first; and then the average spectrum and the variance of these spectra (Figure 3.13) are computed.

Figure 3.13 shows that for the electric field component E_x when the frequency is lower than 6.5 Hz, the average spectrum of segments from quiet period is larger than that of segments from noisy period (the reason is not clear). In the average spectrum of noisy segments, the 60 Hz peak and its harmonics (120 Hz, 180 Hz, 240 Hz, 300 Hz, 420 Hz) are very well defined. In addition, four low frequencies are apparent, such as 7.7 Hz, 15.5 Hz, 22.8 Hz and 34 Hz. This also applies to the magnetic field component H_y .

Curves of variance prove that for both E_x and H_y the 60 Hz and some of its harmonics (180 Hz, 300 Hz, 420 Hz) are the most powerful noise sources in both quiet and noisy time. But for the noisy time, low frequency noises are detected in the two components.

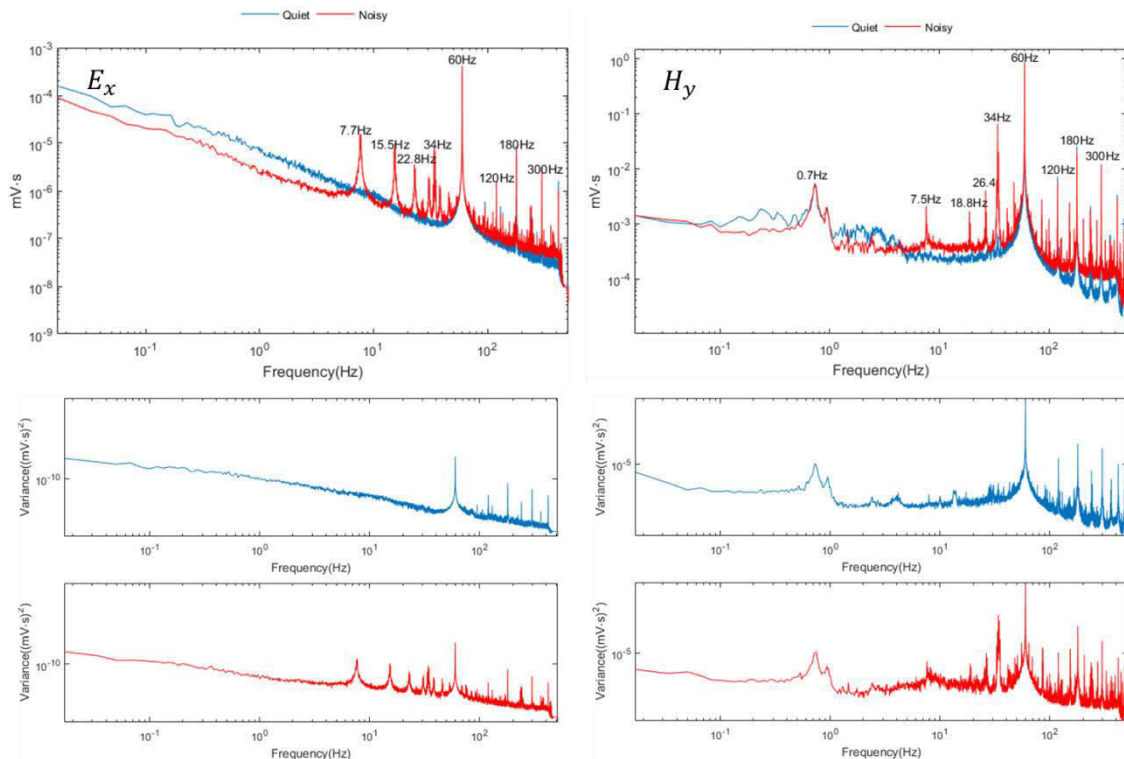


Figure 3.13 Average spectra and variance of the electric field component E_x (left column) and the magnetic component H_y (right column) at site #2 (blue line is the average spectrum of segments from quiet period of time; red line is the average spectrum of segments from quiet period of time).

3.6.2 Analysis with the CWT

We have chosen the CWT to analyze the two segments for its ability to do time-frequency analysis. In this section we choose the Morlet wavelet, which is a symmetry wavelet formed by multiplying an exponential with a Gaussian window.

Figure 3.14 shows the time-frequency representations of the two segments of electric field component E_x and magnetic field component H_y from site #1. In the frequency (vertical axis) and time (horizontal axis) systems, it clearly indicates when a signal at a certain frequency appears. For the electric field component E_x , only the event of 0.01 Hz has been observed in both segments. However, more events can be found in the CWT results of the two segments of H_y . For the quiet segment, there are three

main events: 0.01 Hz, 0.03 Hz, and 60 Hz. The pattern is more complex for the noisy segment. We can see apart from some low frequency signals through time, many discontinuous signals can be found between 1 Hz and 60 Hz. The source for the 60 Hz is the power lines, but to identify sources of other events, more field observations are needed.

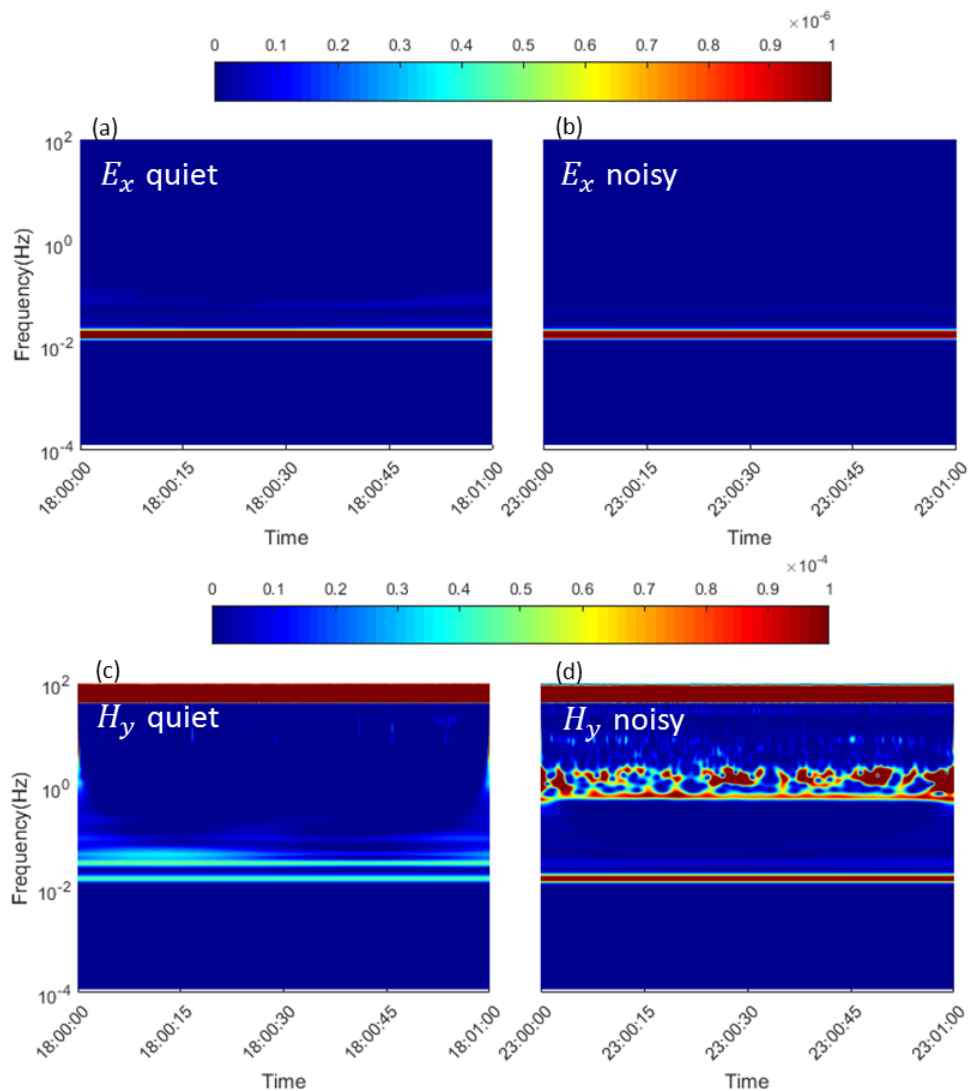


Figure 3.14 Time-frequency representation of the two segments of the electric field component E_x and the magnetic component H_y from site #1.

For the acquisition site #2, since there is a conveyor at this site, the 60 Hz alternative current flows in them, therefore 60 Hz event is recorded in both segments. We can see that when the conveyor is not working (Figure 3.15 (a) and Figure 3.15 (c)); there are events discontinuous in time in addition to the 60 Hz event. It could be as a result of passingby vehicles and other equipment used to load and unload rocks. When the conveyor is working ((Figure 3.15 (b) and Figure 3.15 (d)), additional features of the signal in time-frequency representation arise. For example, in Figure 3.15(d) there is an event of 50 Hz which does not exist in Figure 3.25(a). When the conveyor is operating the 60 Hz event becomes apparently more intense. It is not confirmed yet whether the vibration influences the signal.

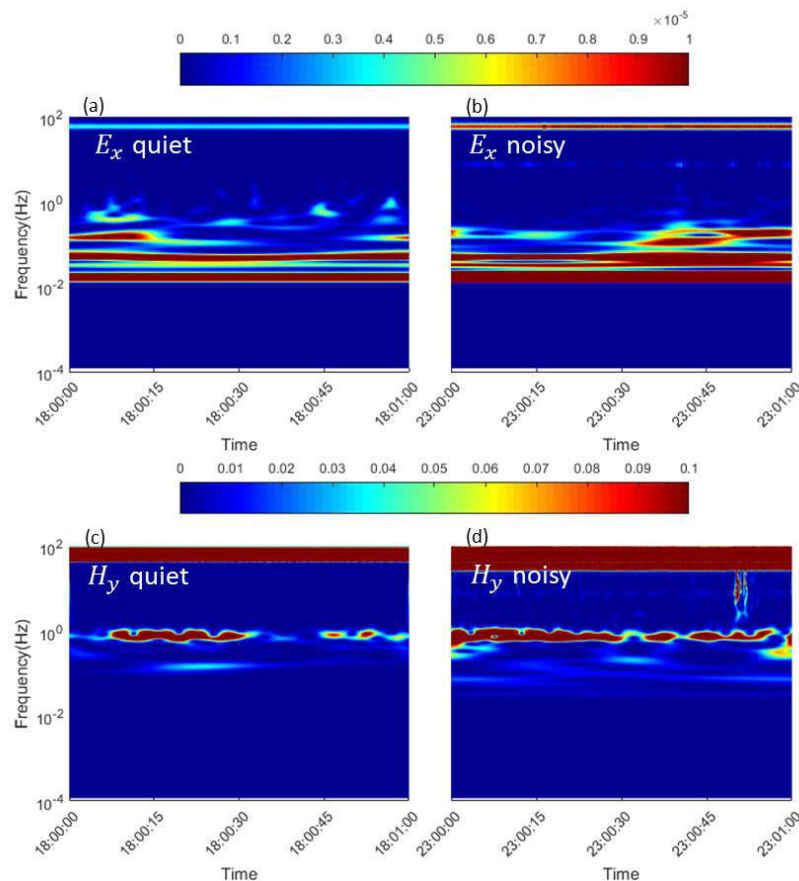


Figure 3.15 Time-frequency representation of the two segments of the electric field component E_x and the magnetic component H_y from site #2.

The environment situation of the acquisition site #3 is similar to that of site #1, therefore, the time-frequency representations for these two sites are basically similar. For site #3 in frequency domain we saw a peak at 60 Hz, however, that event is not shown in the time-frequency domain of the electric field component E_x for both segments. The reason is probably the energy of the 60 Hz event is relatively low so that the event is covered by other events. Whereas, for the magnetic field component, we only observe the 60 Hz event.

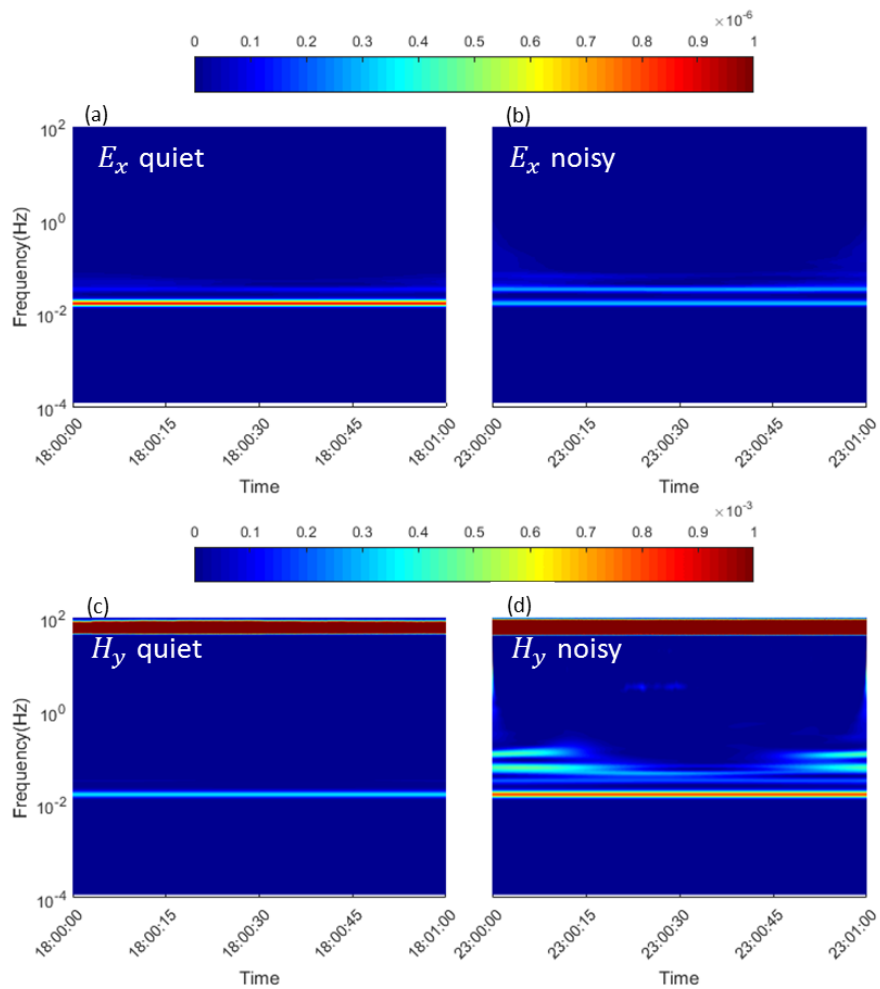


Figure 3.16 Time-frequency representation of the two segments of the electric field component E_x and the magnetic component H_y from site #3.

At the acquisition site #4, main events in the two signal segments of E_x reflected in the time-frequency representation are quite similar, apart from the intensity. As we previously stated that this site is located under a power station. Although the station is always in operation, but the output power changes over time along with other machines' operation status. Therefore, common points and differences between the two signal segments are understandable. The main features are: larger amplitude in the period from 23:00:00 to 23:01:00 while the conveyor and drilling are working, which implies larger output power of the station is. While for the period from 18:00:00 to 18:01:00 both the conveyor and drilling are not working, with lower output power, and we have smaller wavelet coefficient amplitudes in the transform.

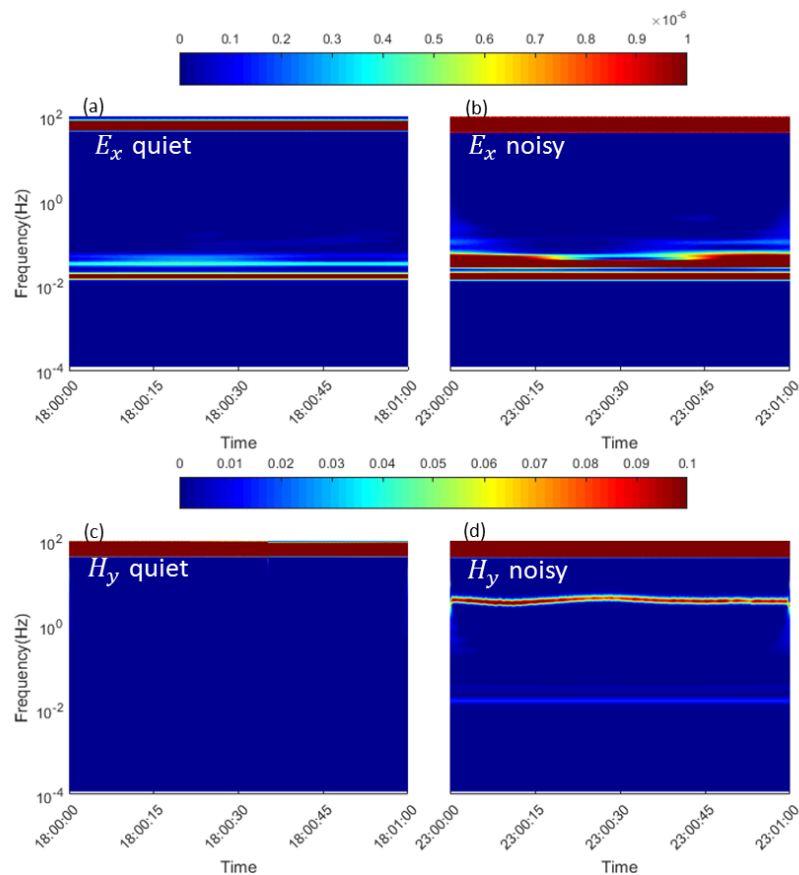


Figure 3.17 Time-frequency representation of the two segments of the electric field component E_x and the magnetic component H_y from site #4.

The acquisition site #5 is located near a drilling site. For E_x , events are observed at 0.01 Hz, 0.03 Hz, and 60 Hz in both segments; but for H_y , only the 60 Hz event is presented. Energy of events observed in noisy segment is higher than those observed in the quiet segment.

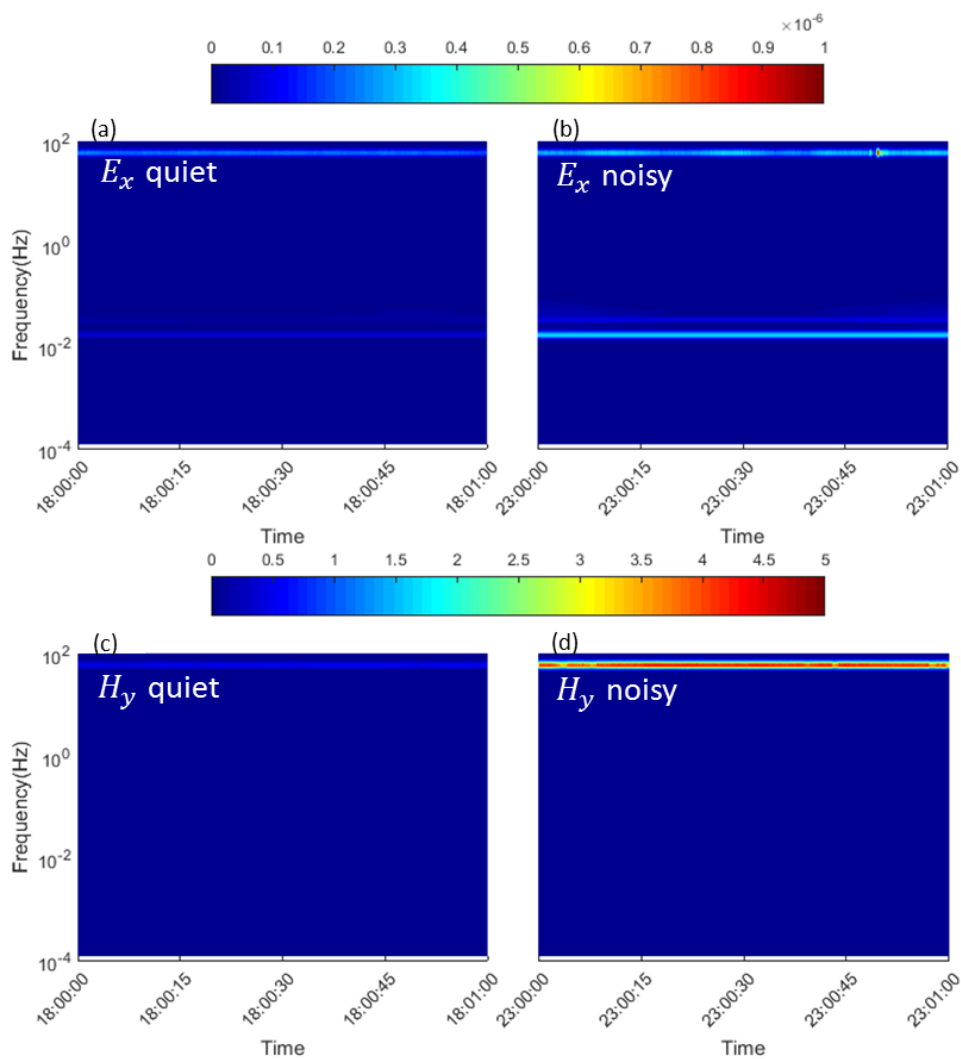


Figure 3.18 Time-frequency representation of the two segments of the electric field component E_x and the magnetic component H_y from site #5.

3.7 Conclusion

In this study we investigated influences of measurement environment on EM recordings. The five data acquisition sites are chosen to be representative of different environments allow to analyze the influence of different possible noise sources related to the mining activities. After applying both the Fourier transform and the CWT on data, we observe that the strongest noise source in the deep mining tunnels is the power supply system (power station, power lines). The mining machines are also a noise source which should be taken into consideration seriously during EM measurement. Not only do they affect the quality of measurement when they are in operation, the influence cannot be neglected even when they are shut off. Since the measurement took place in very deep underground tunnels, high frequency noise, such as sferics, cannot propagate to such a deep place. Furthermore, noises are location-dependent. The frequency bandwidth of most TEM measurement systems is usually very large, sampling rate up to 100 000. However, there is often a bandpass filter integrated in the receiver. By knowing the noise frequencies, one can choose the optimal parameters to prevent the incoming noise signals, or filter them. In the present, there is no study on typical frequencies that can characterize the mineralization.

Speaking of the Fourier transform and the CWT, they are both useful tools in analyzing EM signals. The Fourier transform has great frequency resolution at the cost of losing time information. While the CWT provide a time-frequency representation of the signal, and the resolution can be adjusted by changing scales.

We would mention a fact that there is no GPS signals in the deep underground tunnels; therefore, we were not able to synchronize the measurements. In addition, the data base is too large; even if we use a powerful server we can only process a 3-minutes long data. More researches will be carried out in a post-doctoral program.

CHAPTER IV

DENOISING THE BHTEM DATA WITH DISCRETE WAVELET TRANSFORM BASED METHOD

4.1 Introduction

The idea of wavelets first appeared in the doctoral dissertation of Alfred Haar in 1909. The simplest wavelet family, the Haar wavelet, is a result of his research on orthogonal systems of functions. Jean Morlet, who developed the technique of scaling and translating the analysis window in processing seismic data, formalized the concept of wavelet transform in 1980's. Since then, many researchers have further developed the method, both in theory and in applications (Stephane Mallat, Yves Meyer, Ingrid Daubechies, to name just a few). After decades of development, the wavelet transform has become a versatile tool in diverse scientific domains such as mathematics, physics, medicine, communication, signal processing, and geophysics. Applications of the wavelet transform within geophysics can be essentially summarized into two aspects. In one aspect, the wavelets are used as kernels to extract information from geophysical signal or process; in the other aspect, they are used as basis to characterize the process. Miao and Moon (1999) used wavelet transform to characterize and distinguish reflection and refraction events, coherent noises in reflection seismic signal. In their application, they choose Morlet wavelets, which are compactly supported non-orthogonal wavelets. Compared with compactly supported orthogonal wavelets, non-orthogonal wavelets will not distort the phase. Their results show that the signal-to-noise (S/N) ratio of the processed signal is

improved significantly. Sinha *et al.* (2005) applied the continuous wavelet transform (CWT) to analyze non-stationary seismic signals. They converted the time-scale map into a time-frequency map by implementing inverse Fourier transform on the inverse CWT.

Field examples shown the potential of the wavelet transform method in reservoir characterization. Li *et al.* (2009) introduced the CWT into monitoring the situation of a structure in civil engineering. They proved that the wavelet transform is superior to the Fourier transform in identifying transient signals through the time-frequency map. Liu *et al.* (2016) presented the application of the empirical wavelet transform (EWT), which is a combination of the Fourier transform and the wavelet transform, in analyzing multichannel seismic data. According to them the EWT provides higher resolution than the CWT. Noise reduction techniques for seismic data were developed based on the wavelet transform by Kourouniotis *et al.* (1996). Techniques presented in their paper can effectively attenuate surface waves, airwaves, first breaks, and other types of seismic noise to facilitate the detection of weak events.

In other geophysical fields, Martelet *et al.* (2001) developed an inversion scheme using 1-dimensional CWT for gravity data. Their results showed that the method can be used to estimate the geometry of the geological source. Xu *et al.* (2009) proposed using wavelet transform and spectrum analysis to separate the residual from the regional gravity anomaly. Singh and Singh (2017) investigated the use of the CWT and Euler deconvolution to characterize the source of the magnetic anomaly. The introduction of the wavelet transform to domain of EM came later than in seismic and in potential fields. However, nowadays the method has become pervasive in processing EM signals. Wang *et al.* (2013) proposed a wavelet-based method to correct the movement-induced baseline drift. Nenna and Pidlisecky (2013) used the continuous wavelet transform (CWT) to identify cultural noise and topographic features in an ATEM groundwater survey. Bouchedda *et al.* (2010) also used the

wavelet transform in ATEM data enhancement by reducing the sferics. For ground TEM, the effect of cultural noise, such as noise induced by the nearby building and power lines, and sferics becomes more apparent. Ji et al. (2016) combine the wavelet threshold method and stationary wavelet transform in removing background noise and random spikes for TEM data. As previously stated in section 1.2, the BHEM data suffer from different noise sources, which leads to the need of a specific technique to suppress noises. In the following sections of this chapter, we present the procedure of implementing our methodology to denoise the BHEM data.

4.2 Using the DWT to denoise BHEM data

We introduce first the strategy of applying the discrete wavelet transform (DWT) to BHEM data, and the process of choosing suitable wavelet and decomposition level.

4.2.1 Strategy of applying the DWT to BHEM data

One of the most important features of the wavelet transform is its time-frequency localization ability. Through the DWT, two sorts of coefficients are generated: detail coefficients and approximate coefficients (detail in Chapter II). Denoising with the DWT is mainly implemented by comparing the detail coefficients with a threshold value (Donoho and Johnstone, 1994; Donoho, 1995; and Nagendra *et al.*, 2013). If the absolute value of the coefficient is not smaller than the threshold, it is kept unchanged; otherwise, it will be changed as follow: set to zero (hard thresholding) or shrink towards zero (soft thresholding). Figure 4.1 illustrates the difference between them. The threshold in our case is determined according to the characteristic of the BHEM signal, which decays rapidly while the power-off, and then slowly diminishes to zero. By combining this transient characteristic and the fact that detail coefficients in DWT represent the transient events, it is reasonable to hypothesize that there will be only a few non-zero detail coefficients corresponding to the duration of the fast decay process. Therefore, our thresholding strategy is: detail coefficients corresponding to the fast decay process are kept unchanged, and others are set to

zero. The key question is how many detail coefficients are needed to reconstruct the signal.

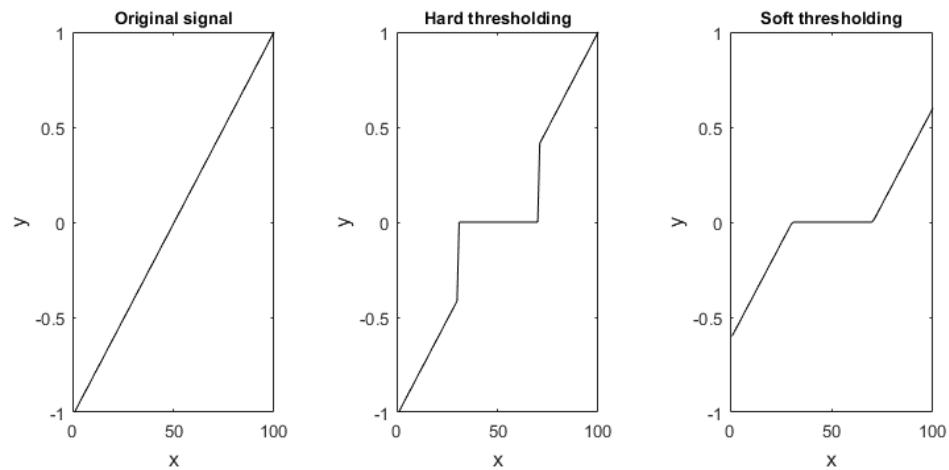


Figure 4.1 Comparison of hard and soft thresholding techniques (Nagendra et al., 2013).

To solve this problem, a synthetic signal is generated (See Figure 4.4). A series of modeling has been implemented by using this signal, the results indicate that only the first eight coefficients are significantly necessary to reconstruct the signal in our case. Figure 4.2 shows that the signal reconstructed with only the first eight detail coefficients perfectly coincides with the original signal; however, if coefficients kept are less than eight, the reconstructed signal will be distorted, which is the result of insufficient information.

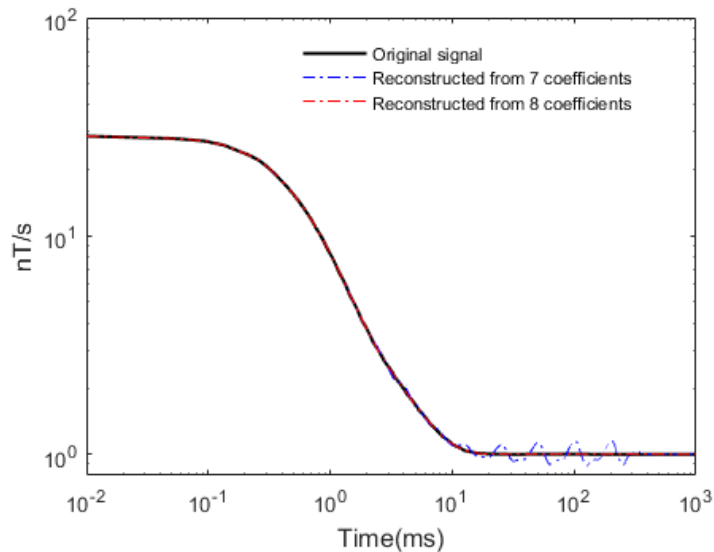


Figure 4.2 Comparison of the original signal and the reconstructed signals.

4.2.2 Choice of suitable wavelet and decomposition level

Before applying the DWT we have to decide the mother wavelet and the decomposition level. The way to find out these two parameters is an iterative comparison trial and error. We have tried many wavelets on a synthetic noisy signal to find out first the mother wavelet; and then with this mother wavelet we find the most appropriate decomposition level for our study.

We generate a noise-free signal (Figure 4.4(a)) using *Loki*, a 3D modeling algorithm developed by the research group of Art Raiche at CSIRO, Australia (Raiche, Sugeng, and Soininen, 2003). The model used to produce the BHTEM signal is presented in Figure 4.3, which contains a prismatic conductor (5 ohm·m) in a homogeneous half-space (3000 ohm·m). Then, three commonly encountered types of noise, which are random noise, noise induced by power line, and sferics (Figure 4.5) are added to the synthetic signal (Figure 4.4(b)). Except for the sferics, which is from field measurements, the other two kinds of noises are generated using Matlab. We would like to mention that the sferics present a type of noise varying with time, it doesn't mean its existence in deep mine environment. We then denoise the noisy signal with

different wavelets. In this process, many wavelets were tested, such as the haar wavelet, daubechies wavelet family, coiflet wavelet family, and symlet wavelet family. Table 4.1 presents the signal-to-noise ratio (SNR), which is calculated by Equation (4.1). According to the results, the wavelet ‘sym5’ is selected. With ‘sym5’ we tried to denoise the noisy signal in Figure 4.4(b) with different decomposition level. Table 4.2 lists the SNR improvements of using various decomposition levels. The decomposition level of 10 gives the best result, therefore it is considered in our study.

$$SNR = 10 \times \log_{10} \frac{P_{signal}}{P_{noise}}, \quad (4.1)$$

where, P_{signal} and P_{noise} are the power of signal and the power of noise, respectively. Given a signal s_n , ($n = 1, 2, 3, \dots, N$. N is the total amount of samples.), then the power of the signal is calculated as: $P = \frac{1}{N} \sum_{n=1}^N s_n^2$.

Table 4.1 Applying different wavelets on a noisy signal with an SNR of 15 dB with a decomposition level of 10.

Wavelet	sym1	sym2	sym3	sym4	sym5	sym6	sym7
SNR(dB)	33.39	33.47	34.27	35.71	35.72	29.00	19.23

Table 4.2 Trying different decomposition levels on a noisy signal with an SNR of 15 dB.

Decomposition level	6	7	8	9	10	11	12
SNR(dB)	26.89	27.97	32.79	35.17	35.72	35.71	35.39

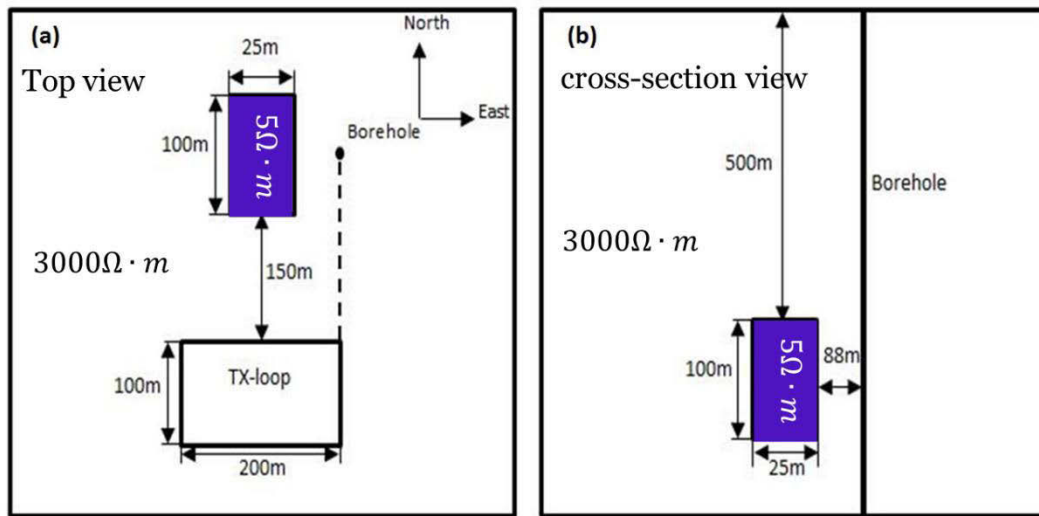


Figure 4.3 The 3D model used to generate synthetic data.

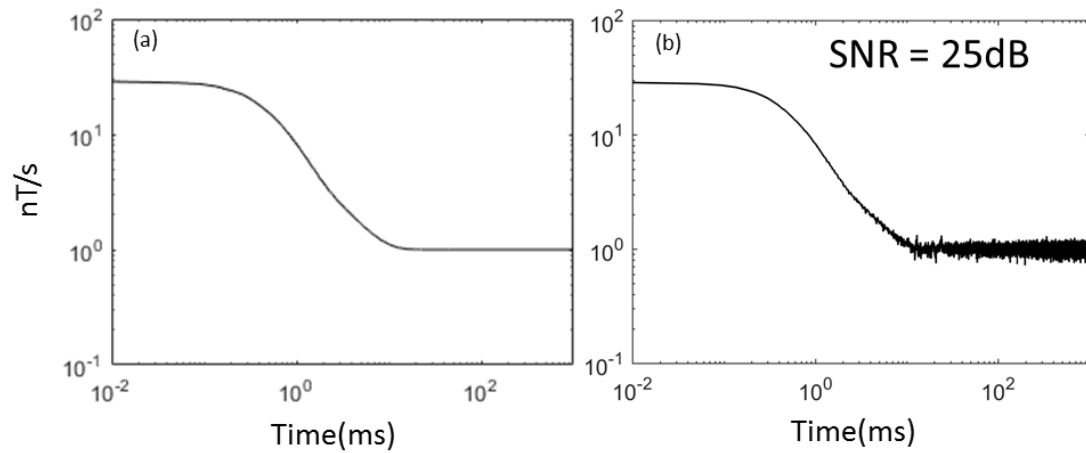


Figure 4.4 The BHEM noise-free signal (a) generated by Loki from the model in Figure 4.3 and the corresponding noisy signal (b).

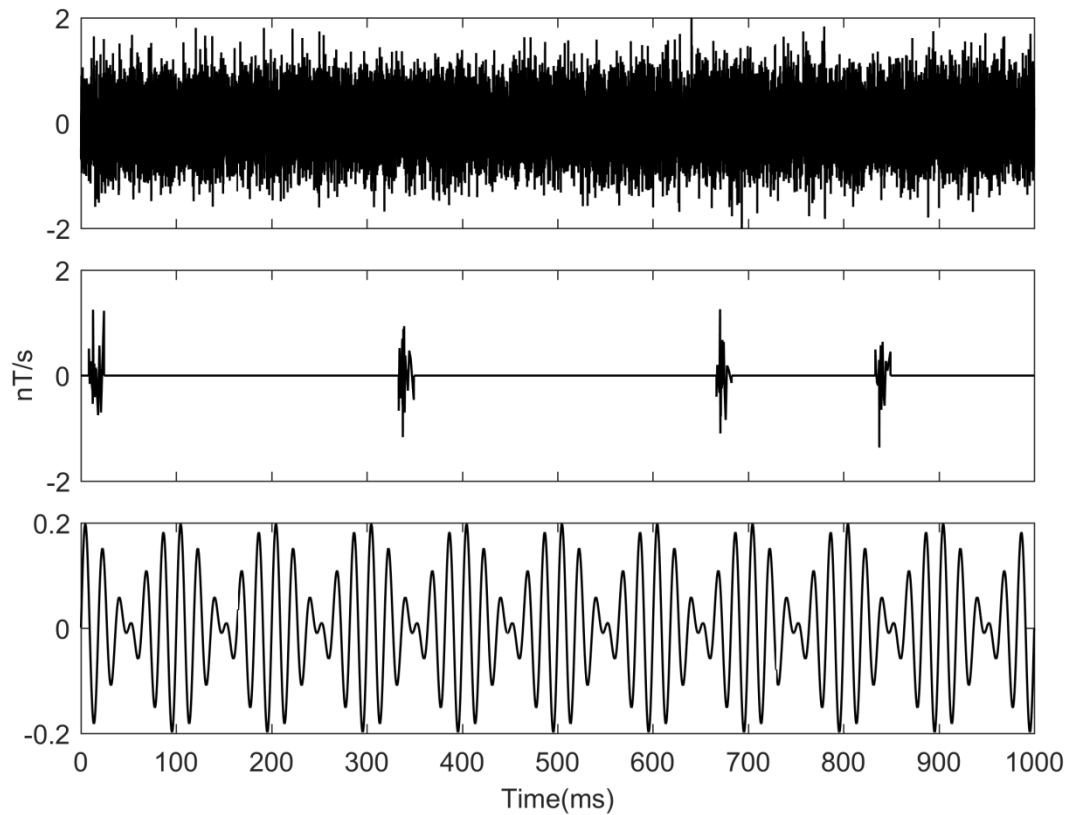


Figure 4.5 Three types of noise added to synthetic data. From top to bottom: random noise, sferics, and noise from the power line (50 and 60 Hz).

4.3 Method validation

To verify the efficiency and effectiveness of our methodology, we test it on both synthetic and field data.

4.3.1 Application of DWT on synthetic data

One way to verify the effectiveness of the denoising method is to apply it to a series of data at different noise levels. We observed when the original signal has an SNR larger than 20 dB, using the DWT alone can yield a satisfactory denoising result. Figures 4.6 (a) and (b) show the SNR increases from 30 dB to 52 dB, and from 25 dB to 47 dB (Figure 4.6 (c) and (d)) after the denoising with DWT. Whereas, when the quality of the signal is not good enough, using the DWT alone will not reduce the

noise to a satisfactory level (Figure 4.7 and Figure 4.8), especially for later time channels. There is a visible perturbation remained in processed data after the DWT. These noise residuals may affect the interpretation accuracy in future works. We therefore use the curve fitting technique (CFT) as a complementary method in dealing with the post-processing of simple data sets. Details of under what circumstances the curve fitting technique is used are explained in section 2.2.1.

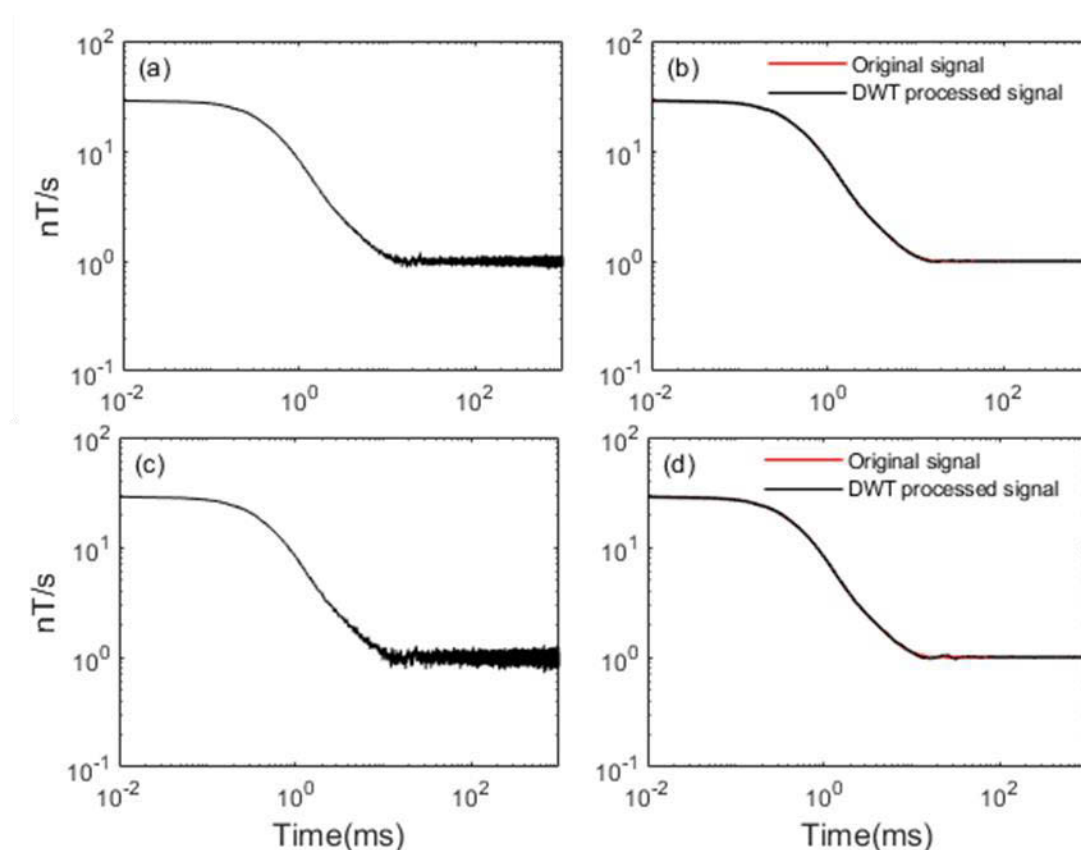


Figure 4.6 The synthetic noisy signals (a) and (c) at different noise level, the SNR after the DWT is increased from 30 dB to 52 dB (b), and from 25 dB to 47 dB (d), respectively.

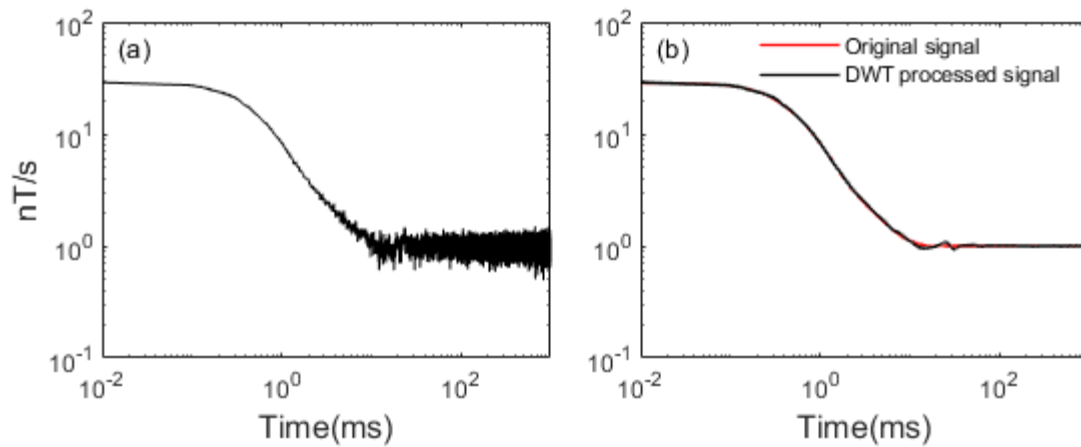


Figure 4.7 The synthetic noisy signal (a) and the result obtained from the DWT (b). In this case the SNR is increased from 20 dB to 40 dB. Slight perturbations appear in the DWT processed result.

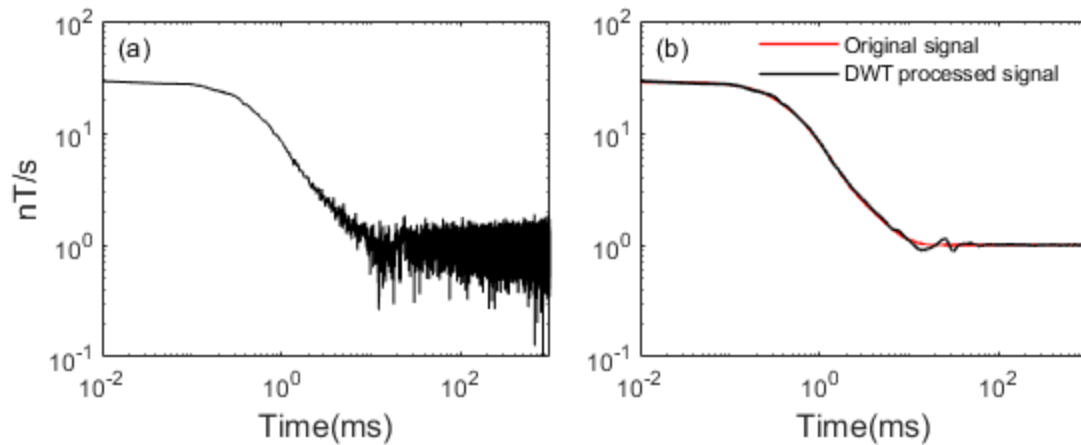


Figure 4.8 The synthetic noisy signal (a) and the result obtained from the DWT (b). In this case the SNR is increased from 15 dB to 35 dB. As the noise level increases, the perturbation in the DWT processed result becomes more severe.

To use the CFT to smooth the DWT denoised signal, we first locate the perturbations in the signal, and then exclude them by a fitting process as described in section 2.2.1. We take a noisy signal with an SNR of 15 dB as an example to show the effectiveness of the CFT as a complementary method.

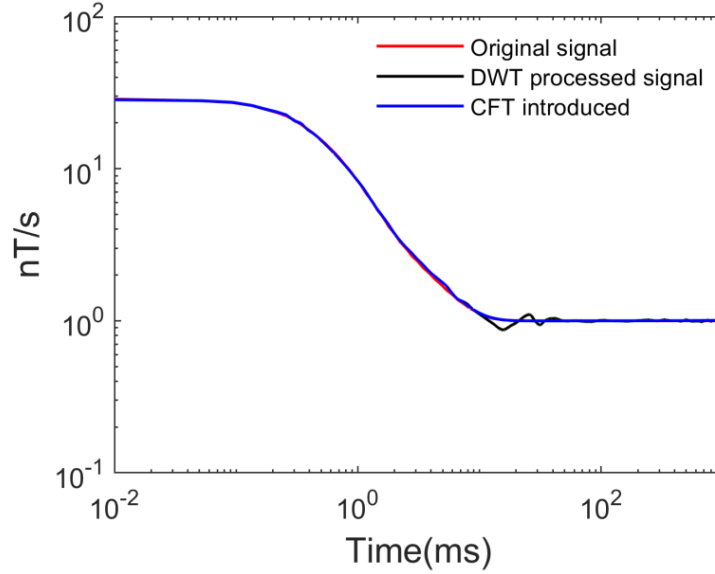


Figure 4.9 Comparison of denoising results before and after curve fitting.

Figure 4.9 shows that the residuals are removed by with CFT effectively. Apart from the SNR evaluation, two more statistic parameters are calculated. They are the relative error calculated by equation (4.2), and the mean squared error (MSE) calculated by equation (4.3).

$$\delta x_n = \left| \frac{x_n - x'_n}{x_n} \right|, \mathbf{n} = \mathbf{1}, \mathbf{2}, \mathbf{3}, \dots, \mathbf{N}. \quad (4.2)$$

$$MSE(x) = \frac{1}{N} \sum_{n=1}^N (x_n - x'_n)^2. \quad (4.3)$$

Variables x and x' represent the original noise-free signal and the denoised signal, respectively. N is the total amount of samplings. The relative error curves are shown in Figure 4.10, and values of MSE and SNR are listed in Table 4.3.

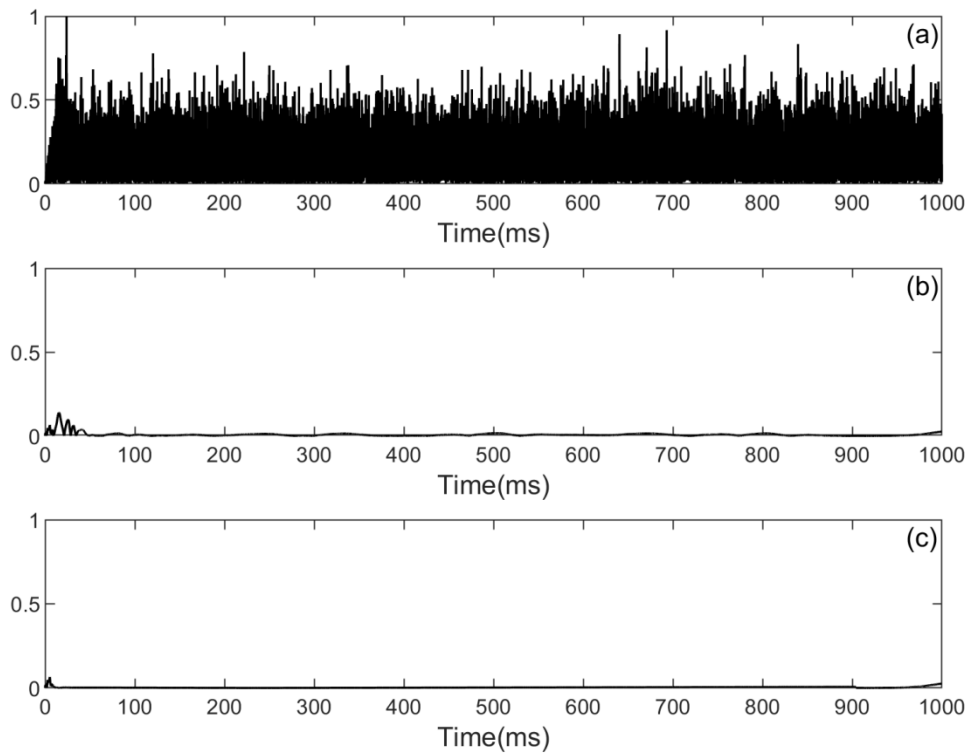


Figure 4.10 Relative error curves, (a) the error curve of the noisy signal, (b) the error curve of the denoised signal when only DWT is used, (c) the error curve of the denoised signal after DWT and CFT.

Table 4.3 Values of MSE and SNR of different signals.

Signal	MSE	SNR(dB)
Noisy signal	0.044	15.0
Signal processed by DWT	3.702×10^{-4}	35.7
Signal processed by DWT and CFT	0.907×10^{-4}	41.8

According to the relative error curves and the MSE and SNR values listed in Table 4.3, the DWT method can effectively remove the most part of the noise, and the CFT further eliminates residual noise.

4.3.2 Application on field data

The denoising method has also been tested on field BHTEM data, provided by Abitibi Geophysics Inc. The measurement system is the SmarTem24, which is a product of ElectroMagnetic Imaging Technology (EMIT), and can simultaneously record three components, coaxial component A and two orthogonal components (U and V) as depicted in Figure 1.2.

In the actual operation in the field, BHTEM measurement at each survey station is repeated for many times to improve data quality. In addition to the three types of noise considered in the synthetic data processing, other sorts of noise during the BHTEM measurement may come from the electronic instability and the movement of the sensor. Fortunately, the repeated measurement mechanism provides us with a way to identify the distorted signals and then correct them accordingly. Detailed steps of processing real BHTEM field data are as follows.

1. Denoise raw data using the DWT. Every BHTEM measurement consists of four transients: two on-time transients and two off-time transients. All of those transients are denoised by the DWT. Since every transient could be affected differently by the noise, the advantage of denoising raw data instead of stacked data is that those distorted transients can be identified and corrected afterwards. This can reduce distortion and preserve useful information.
2. Identify and correct distorted transients through correlation analysis. We take a certain percentage of the measurement, for example, 10% with the smallest mean values as distorted transients; and these distorted transients will be replaced by linear interpolation.
3. Stacking processed data. Stacking is a fundamental and rudimentary process to reduce noise in TEM data processing. It is a process of averaging a series of transients. As it is a process of averaging, it has a limited effect on reducing non-random noise. Examples are presented later to demonstrate the advantage

of using denoised raw data to stack. In this study, Halverson stacking is chosen for its ability to remove linear drift (Kingman et al., 2004).

Since the three components (A, U, and V) of BHEEM data may be affected differently by noise, three examples are presented separately below. These three example is not necessarily from the same survey point. They were chosen to represent a specific data set. For example the data set of component-A is chosen for its unique drift change phenomenon. Therefore, there is no direct connection between these examples.

Component-A: There are 128 transients in the example recording (Figure 4.11). From the figure, it can be seen that the signal can be divided into two segments based on the drift situation. The first segment, which has no drift, is consisted of the first 34 transients. The second segment, which drifts linearly, is composed of the last 94 transients. Each segment is processed separately.

Noise level in this data set is very low. There is no obvious difference between the raw data (Figure 4.11(a)) and those denoised by the DWT (Figure 4.11(b)). Nevertheless, the abrupt change of the drift situation causes the distortion of the 34th transient, as red arrows indicate in the Figure 4.11(a). The distortion is not corrected after the DWT denoising process (Figure 4.11(b)), but it is corrected by correlation analysis (Figure 4.11(c)).

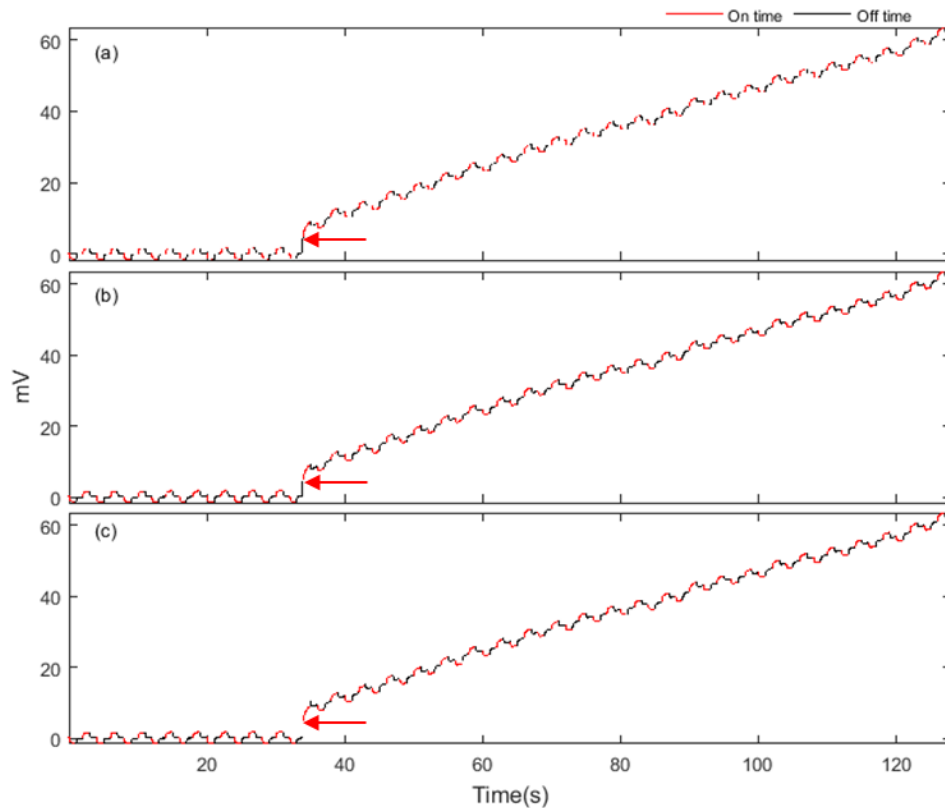


Figure 4.11 Raw data of component-A. (a) Original raw data, (b) denoised raw data, (c) denoised raw data with distortion corrected.

Figure 4.12 and Figure 4.13 show stacked signals for on-time transients and off-time transients, respectively. We can see that stacked on-time signals do not change over raw data sets. The reason is that the noise level is very low in this data set, and the only distortion occurs in off-time transients. However, for stacked off-time signals, big difference can be observed between the one stacked from denoised raw data with distortion corrected using correlation analysis. This example shows us that the distorted transient will significantly affect the stacked result. It proves the necessity to identify and correct the distorted transients properly.

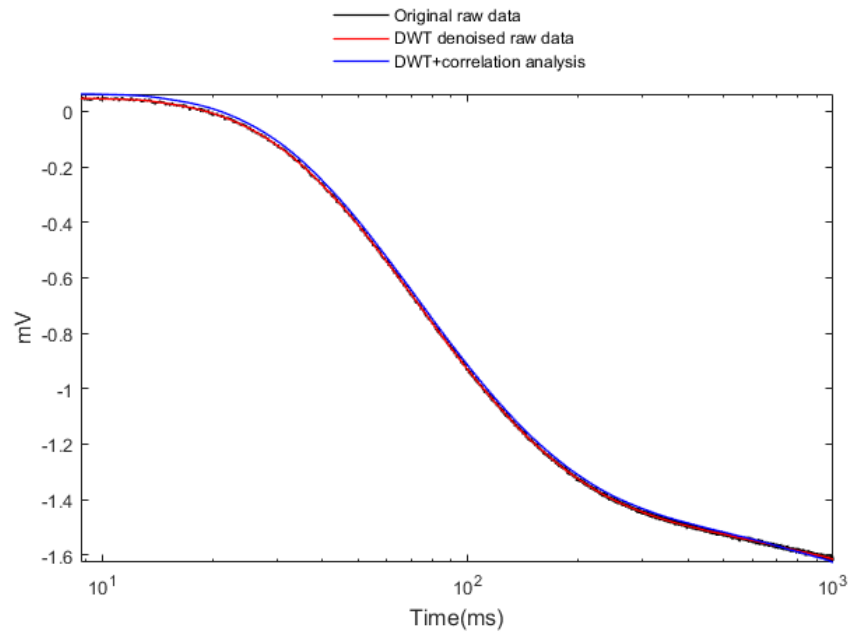


Figure 4.12 Stacked on-time signals for component-A.

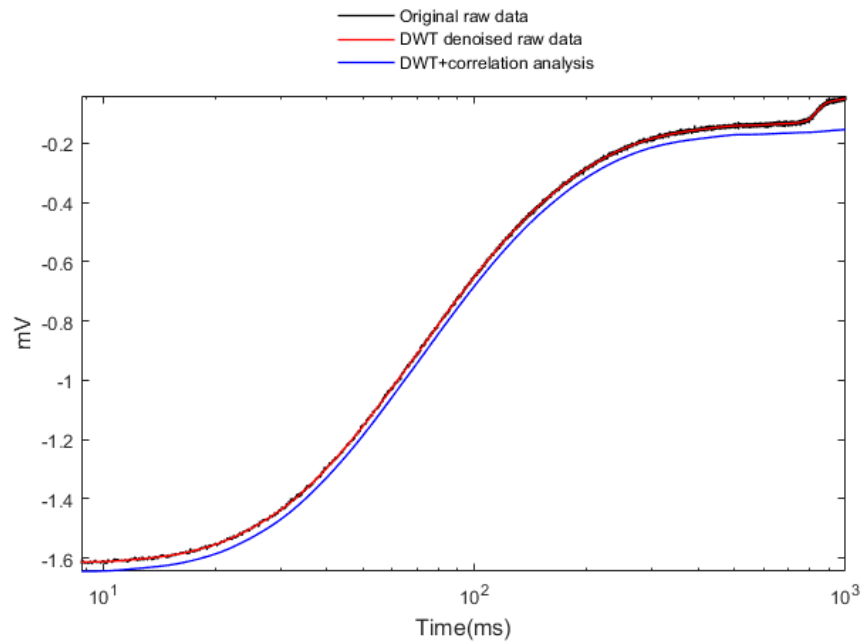


Figure 4.13 Stacked off-time signals for component-A.

Component-U: There are 128 transients in this data set (Figure 4.14). The segmentation of this data set is much more complicated than the previous example. Since we are using the Halverson stacking method, and this method is efficient in suppressing linear drifting, we need to keep the drift in every segment as linear as possible. Based on this criterion, the data set is divided into five segments: (1) transients 1 to 12; (2) transients 13 to 44; (3) transients 45 to 60; (4) transients 61 to 118; and (5) transients 119 to 128. Compared with the previous example, noise level in this data set is higher, and the distortion is more severe. After denoised by the DWT most noise is eliminated (compare 4.14(a) and (b)), whereas, distortions remain unchanged (Figure 4.14(b)). After the distorted transients in the data set are identified, they are corrected through correlation analysis (Figure 4.14(c)).

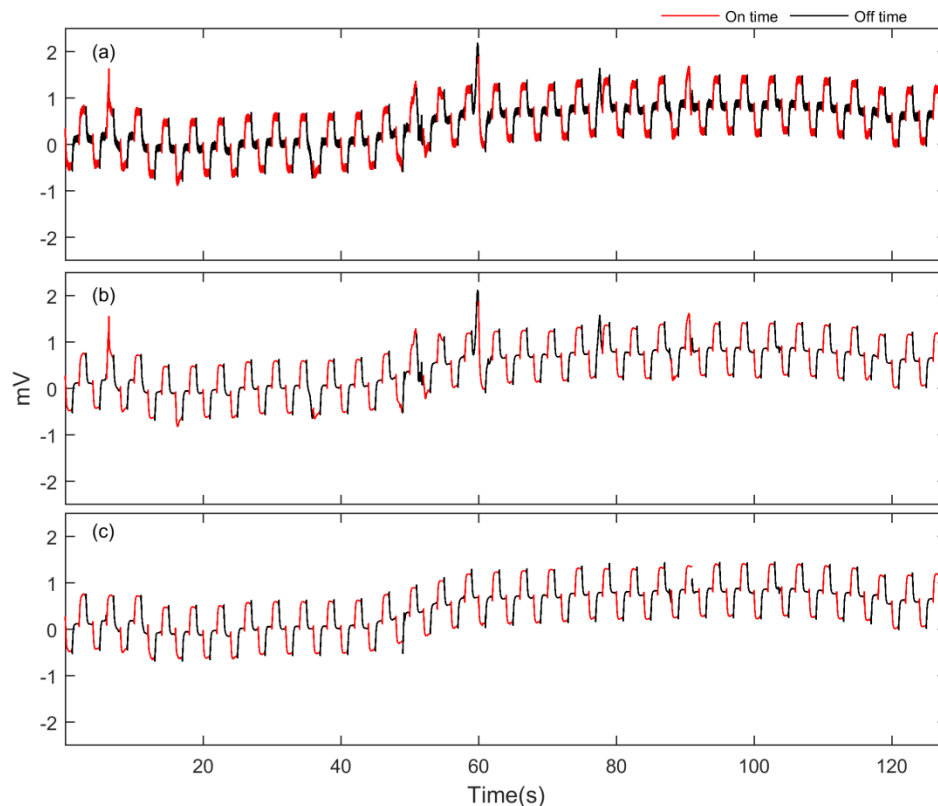


Figure 4.14 Raw data of component-U. (a) Original raw data, (b) denoised raw data, (c) denoised raw data with distortion corrected.

Figure 4.15 and Figure 4.16 present stacked signals for on-time transients and off-time transients, respectively. Applying the DWT on the data set certainly improves the quality, however, there is no apparent difference in the shape of the curve between stacking from original raw data and stacking from the DWT denoised raw data. After distortions are remedied, stacked curves become smoother and more reasonable. This example illustrates the impact of the distortions on the form of stacked curves.

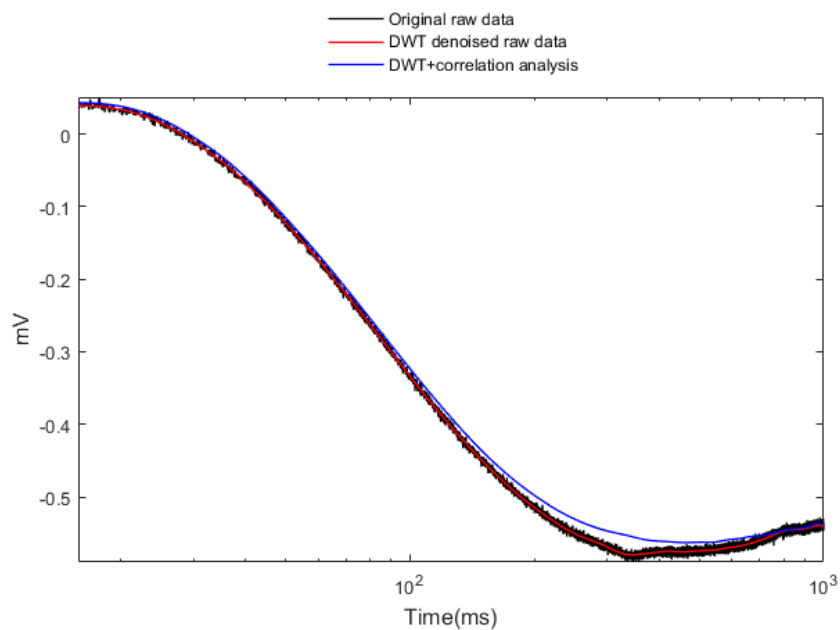


Figure 4.15 Stacked off-time signals for component-U

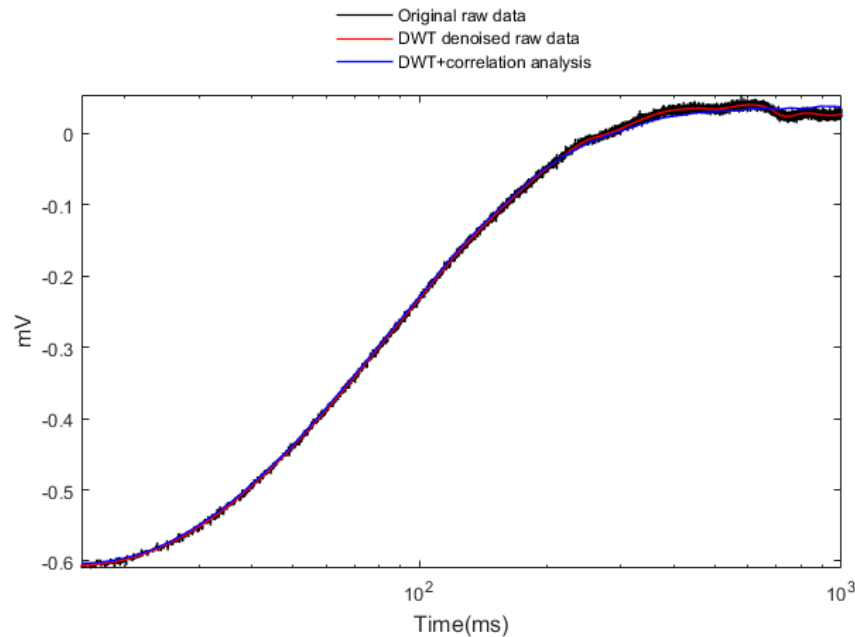


Figure 4.16 Stacked off-time signals for component-U.

Component-V: Same as data sets in the two previous examples, there are 128 transients in this data set (Figure 4.17). No obvious change in drift situation is observed, so the data set will be treated ensemble, i.e., no segmentation is needed.

The most obvious feature of the data set we notice is that the noise level is moderately high, and the amount of distorted transients is small, but the distortion degree is very large. Similarly, after the application of DWT noise level is lowered a lot (compare 4.17(a) and (b)), distortions remain unchanged (Figure 4.17(b)). Only after the use of correlation analysis distorted transients in the data set are corrected effectively (Figure 4.17(c)).

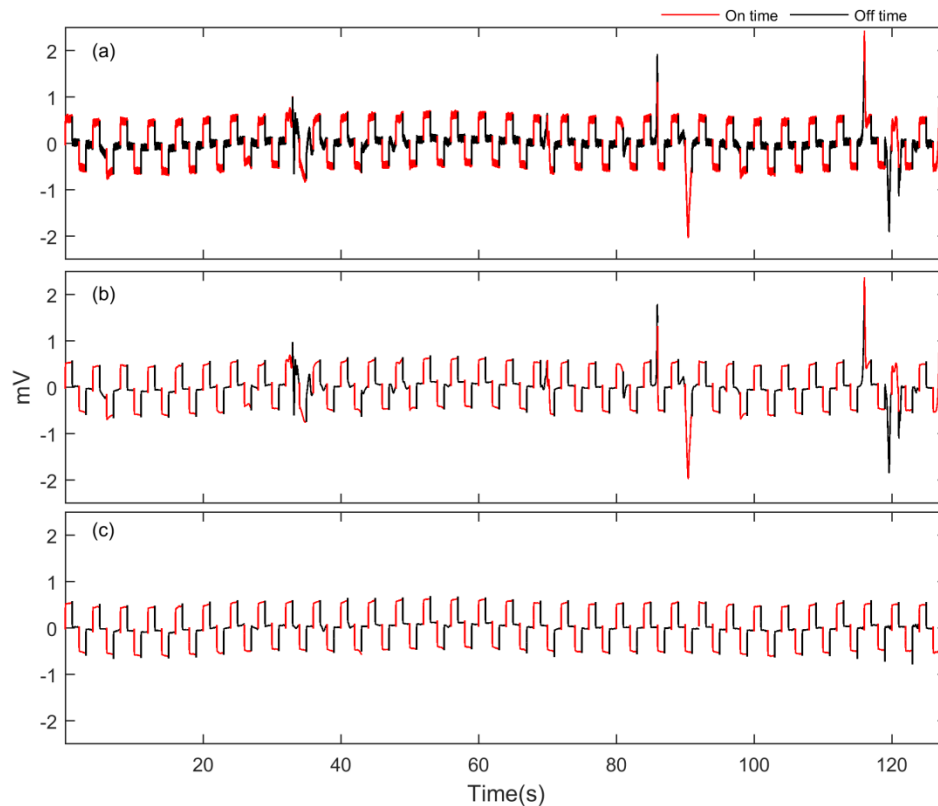


Figure 4.17 Raw data of component-V. (a) Original raw data, (b) denoised raw data, (c) denoised raw data with distortion corrected.

As presented in the two previous examples, the denoising process with the DWT does improve the SNR of the signal, whereas it is not able to reduce the influence of distorted transients on the result of stacking (Figure 4.18 and Figure 4.19). The correlation analysis is indispensable in improving data quality.

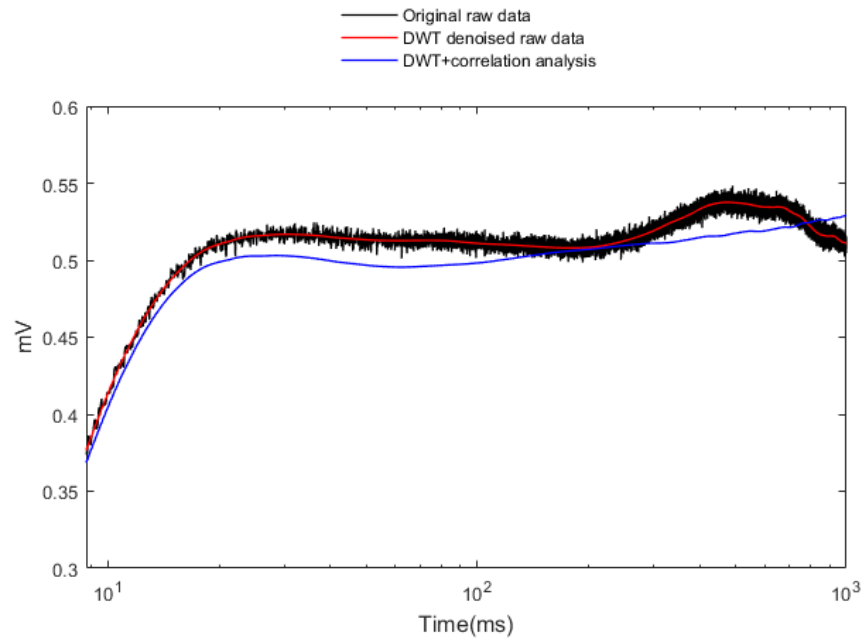


Figure 4.18 Stacked on-time signals for component-V.

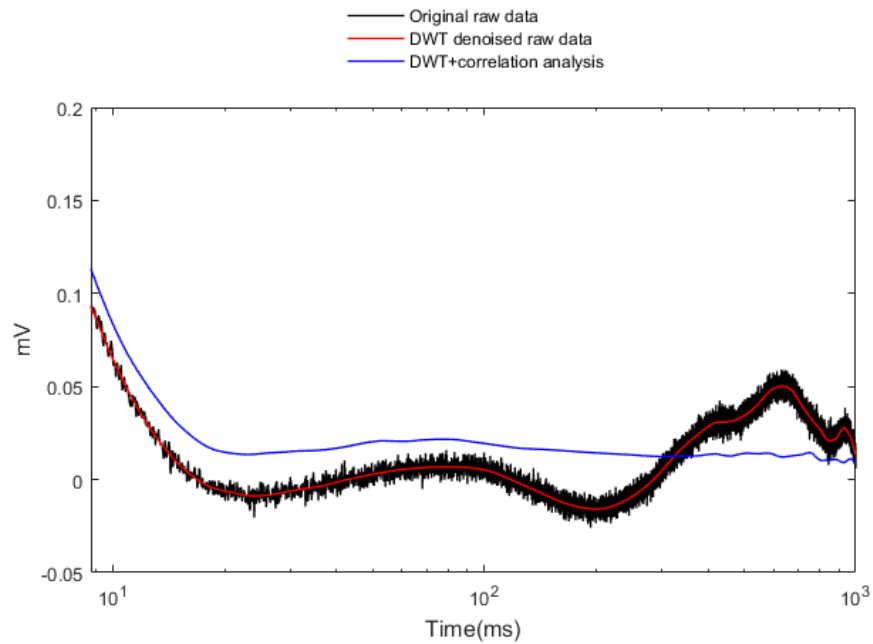


Figure 4.19 Stacked off-time signals for component-V.

4.4 Conclusion

The presented wavelet-based technique combines the wavelet's ability to detect transient events and the unique characteristics of the BHTEM signal. The application of our method is not limited by the nature of the noise, and there is no need to locate the noise in the signal.

Applications on synthetic and field data show that using the DWT alone can considerably reduce the noise level, but the noise residual may still have negative influences on future interpretations. Different complementary measures are taken to reduce the residuals. For simple data sets, the residual is caused mainly by the noise retained in the unprocessed detail coefficients. In this case, we use the curve fitting method to smooth the signal. For field data with repeated measurements, the residual is mainly caused by distorted transients. Those distortions can be caused by the instability of the equipment and the oscillation of the sensor. To reduce its influence, the correlation analysis is implemented. Another potential way to reduce the influences of distorted transients in field data sets is to apply a scheme of weighted stacking, which means we apply a small weight to these identified distorted transients.

CHAPTER V

GENERAL CONCLUSION

The Ph.D project focused on solving practical problems encountered by exploration geophysicists in EM prospecting. The entire project has been planned and carried out in close collaboration with our mining industry partners. Unlike on the surface of the earth, limited space makes measurements underground more challenging; especially for EM measurements because the target's response is proportional to the intensity of the primary electromagnetic field. This study is the first to analyze the noise characteristics of the deep underground mining environment. The investigation of influences of mining-related activities on EM measurements in deep ground galleries has been carried out. A methodology has then been developed to improve the data quality of the borehole transient electromagnetic (BHTEM) method.

A preliminary analysis was done on five EM signal recordings at quiet and noisy places in deep underground galleries of LaRonde Mine. It showed that the electricity supply system is the most important noise source. The 60 Hz signal is constantly observed at all five places and is more visible in quiet environment. Mining activities, such as drilling and rock crushing, are associated with increased power, which amplified the noise level in measurements considerably. To improve the signal-to-noise ratio of the BHTEM data, we developed methods based on the discrete wavelet transform (DWT) to denoise the raw data. After testing on both synthetic and field survey data, the proposed methodology is proven to be effective and efficient.

However, in some very noisy cases, the DWT alone is not sufficient. Therefore, complementary methods are introduced depending on the characteristics of the data to be processed. For relatively simple data sets, i.e. synthetic signals, a curve fitting method is enough to smooth the signal further after denoised by the DWT. In the fitting process, a widely used decay model for the EM signals is used. To constrain the fitting result, data points contaminated by residual noise are identified and excluded from the fitting process. For field data sets, which have a much more complicated data structure, we turn to correlation analysis of repeated BHTEM measurements at each survey point. The BHTEM measurements may suffer from distortions caused by electronic instability of the device, or the movement of the sensor, but geological noises are the same over time. Therefore, correlation analysis of measurements made at the same place at different times can separate random noises from geological noises. Reviewing work done in the frame of this Ph.D project, the following recommendations are made for further developments:

- A more powerful computation facility or a re-write of the algorithm outside of Matlab is necessary, in order to process the full data set recorded in deep underground galleries with high temporal resolution.
- To characterize the noises in the deep mining environment more accurately, vibrations due to heavy trucks and blasts should be taken into account. A detailed record of all underground mining activities is necessary.
- In the survey in galleries at the LaRonde mine was carried out without synchronization. This makes it virtually impossible to locate very short-time-duration events, because without synchronization every channel in one receiver starts at different time; and we do not know . In future work, it can be improved using 2.2 % ZEN GPS SYNC. (Zonge International).
- Regarding the denoising method for BHTEM data, it was developed specifically for data collected by SmarTem 24. Whether it works on data collected by other BHTEM systems is to be tested.

- In the process of denoising BHTEM field data set we use the linear interpolation to correct the distorted transients. As we mentioned in Chapter IV another potential method is using weighted stacking method. This probably will speed up the calculation.

APPENDIX I

RESULTS OF CHANNEL 2 (EY) AND CHANNEL 3 (HX)

I.1 Results of acquisition site #1

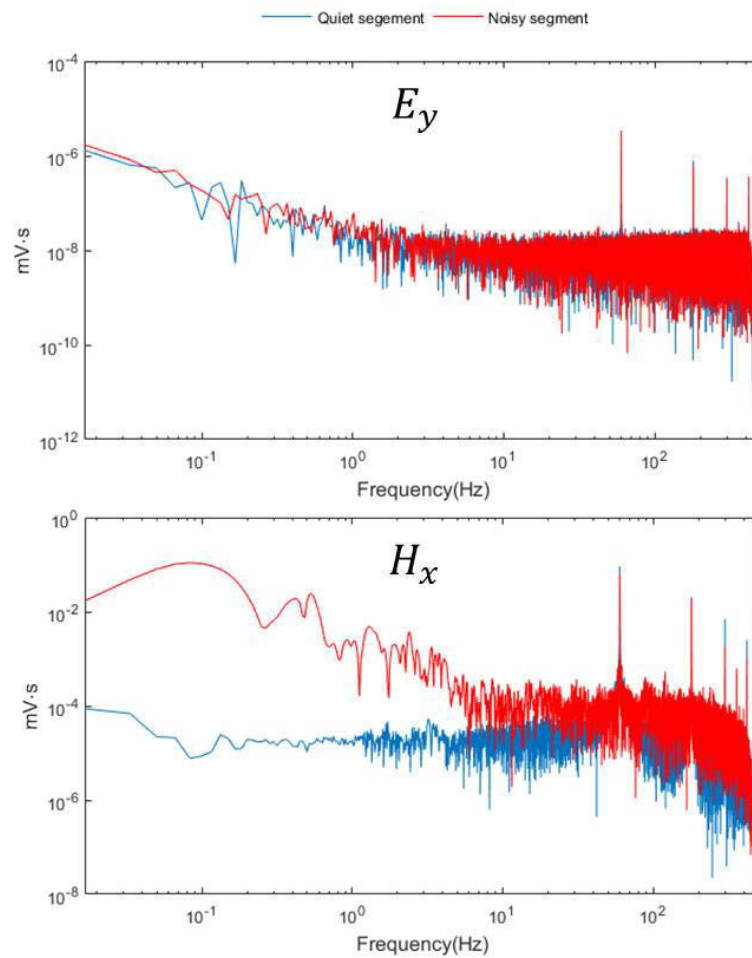


Figure I.1 FT results of the two segments of the electric field component E_y and the magnetic component H_x at site #1.

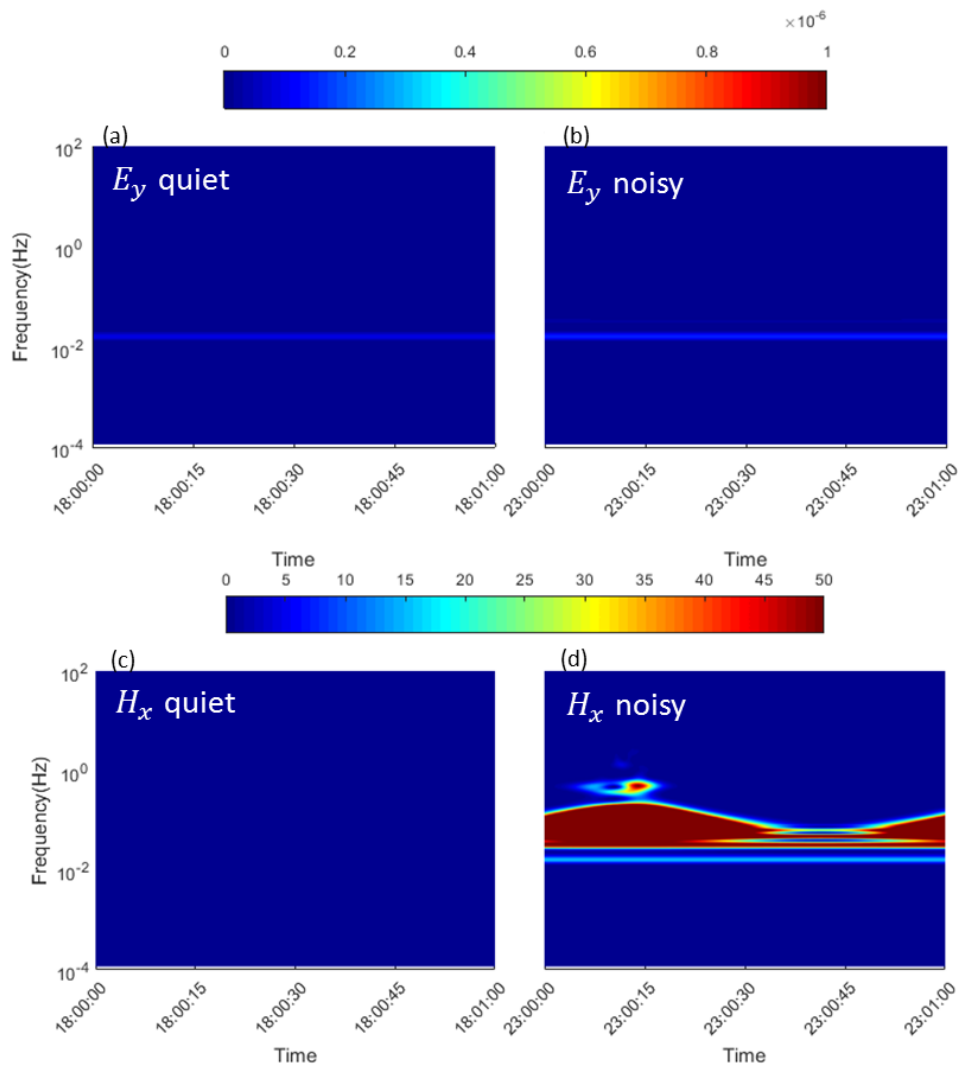


Figure I.2 Time-frequency representation of the two segments of the electric field component E_y and the magnetic component H_x from site #1.

I.2 Results of acquisition site #2

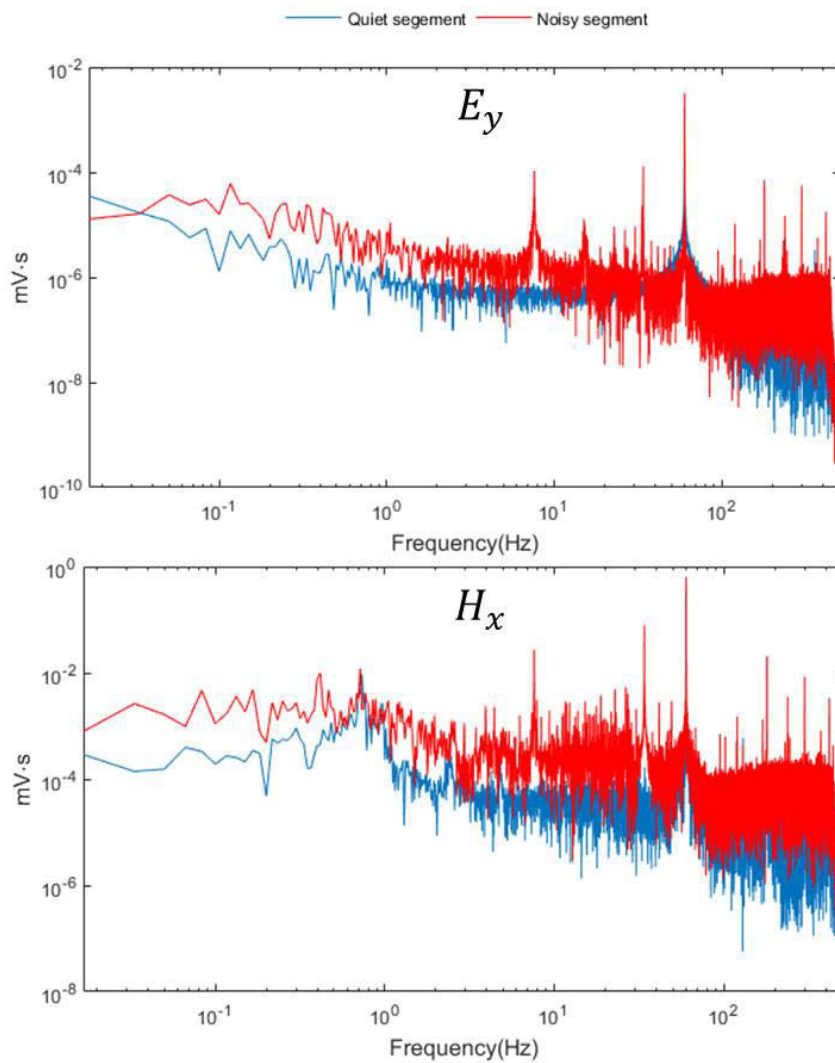


Figure I.3 FT results of the two segments of the electric field component E_y and the magnetic component H_x at site #2.

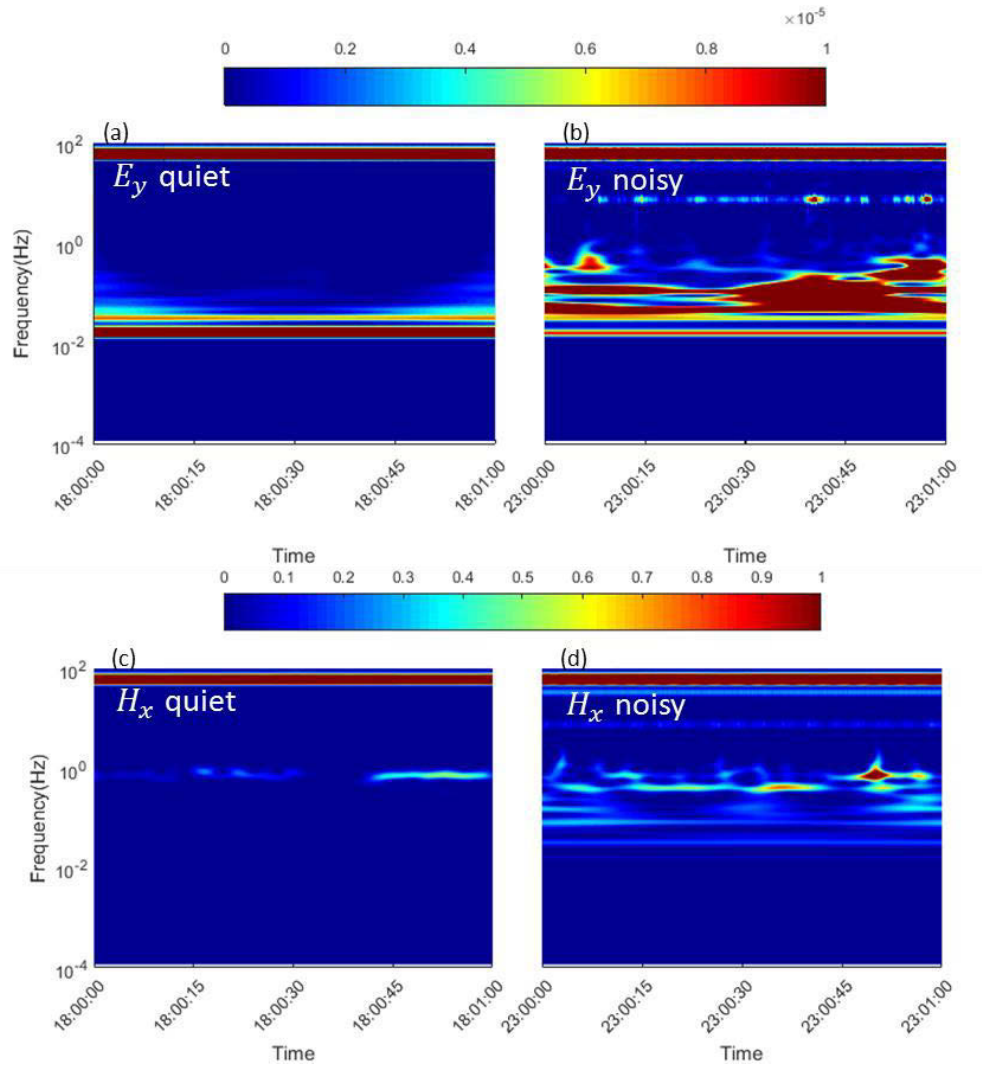


Figure I.4 Time-frequency representation of the two segments of the electric field component E_y and the magnetic component H_x from site #2.

I.3 Results of acquisition site #3

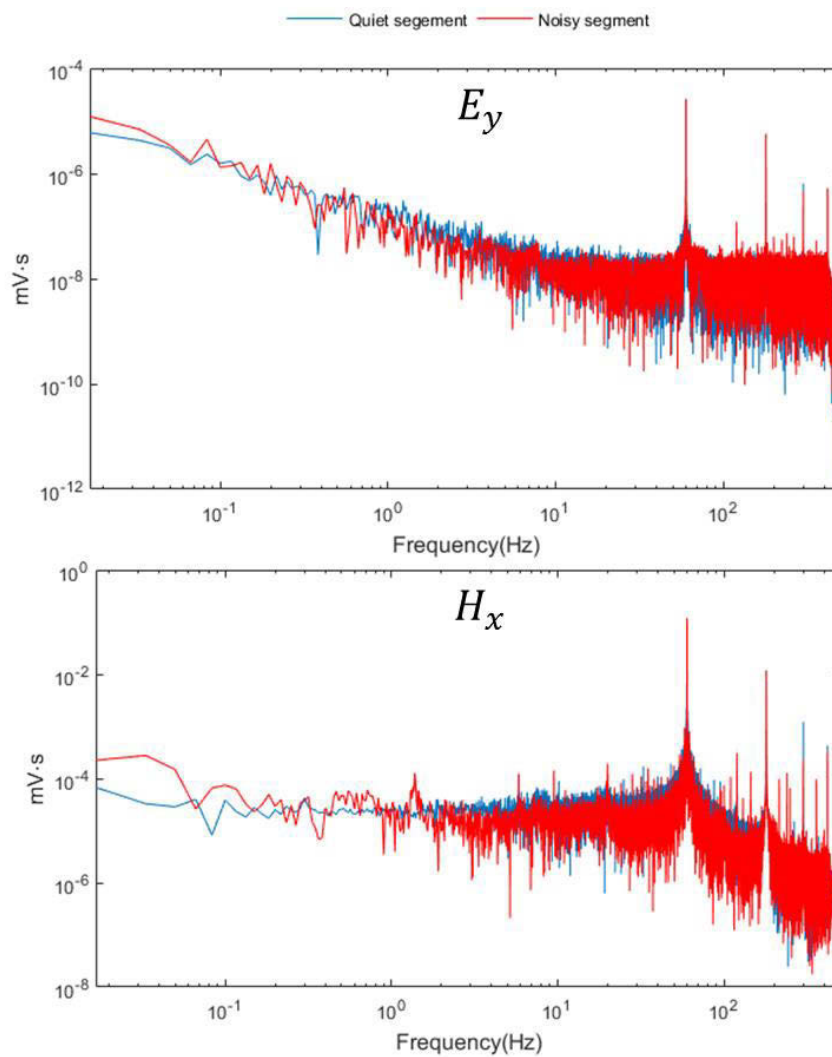


Figure I.5 FT results of the two segments of the electric field component E_y and the magnetic component H_x at site #3.

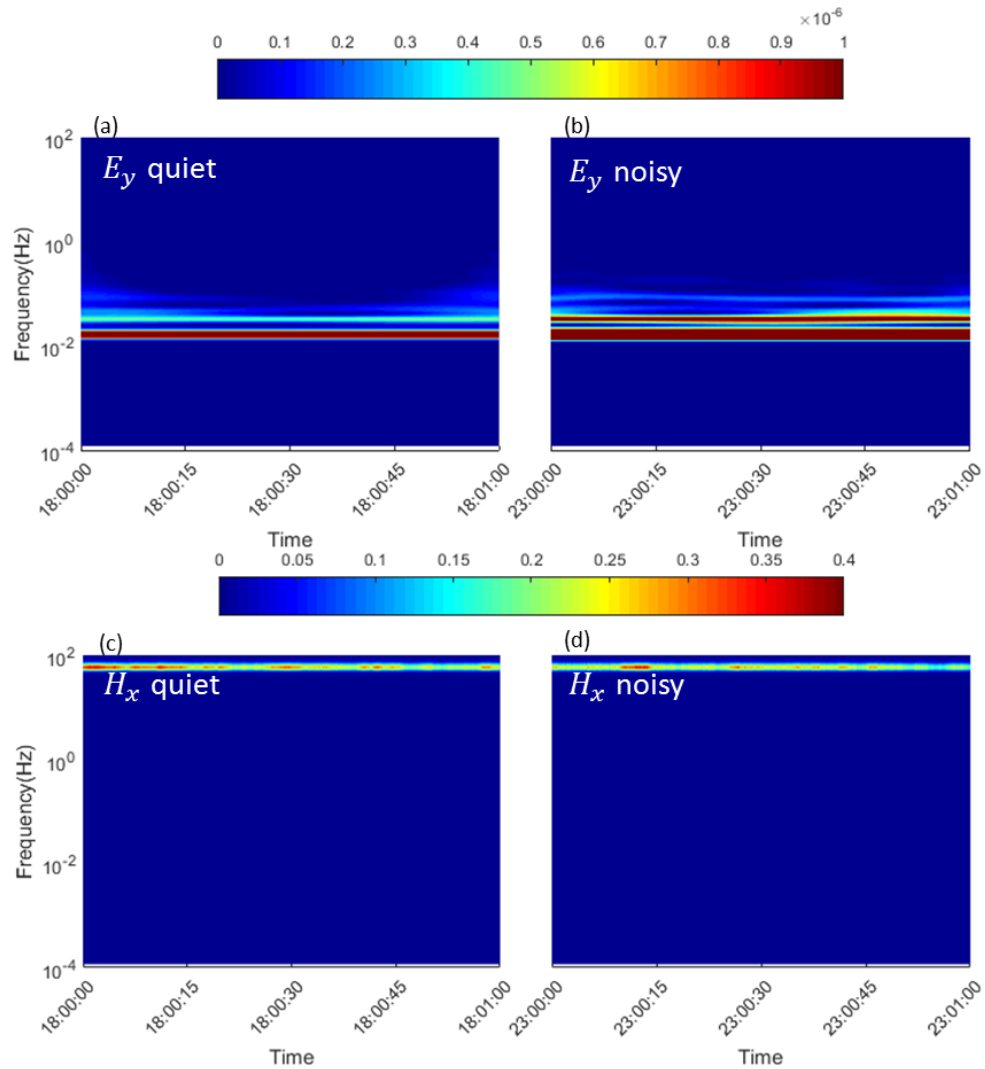


Figure I.6 Time-frequency representation of the two segments of the electric field component E_y and the magnetic component H_x from site #3.

I.4 Results of acquisition site #4

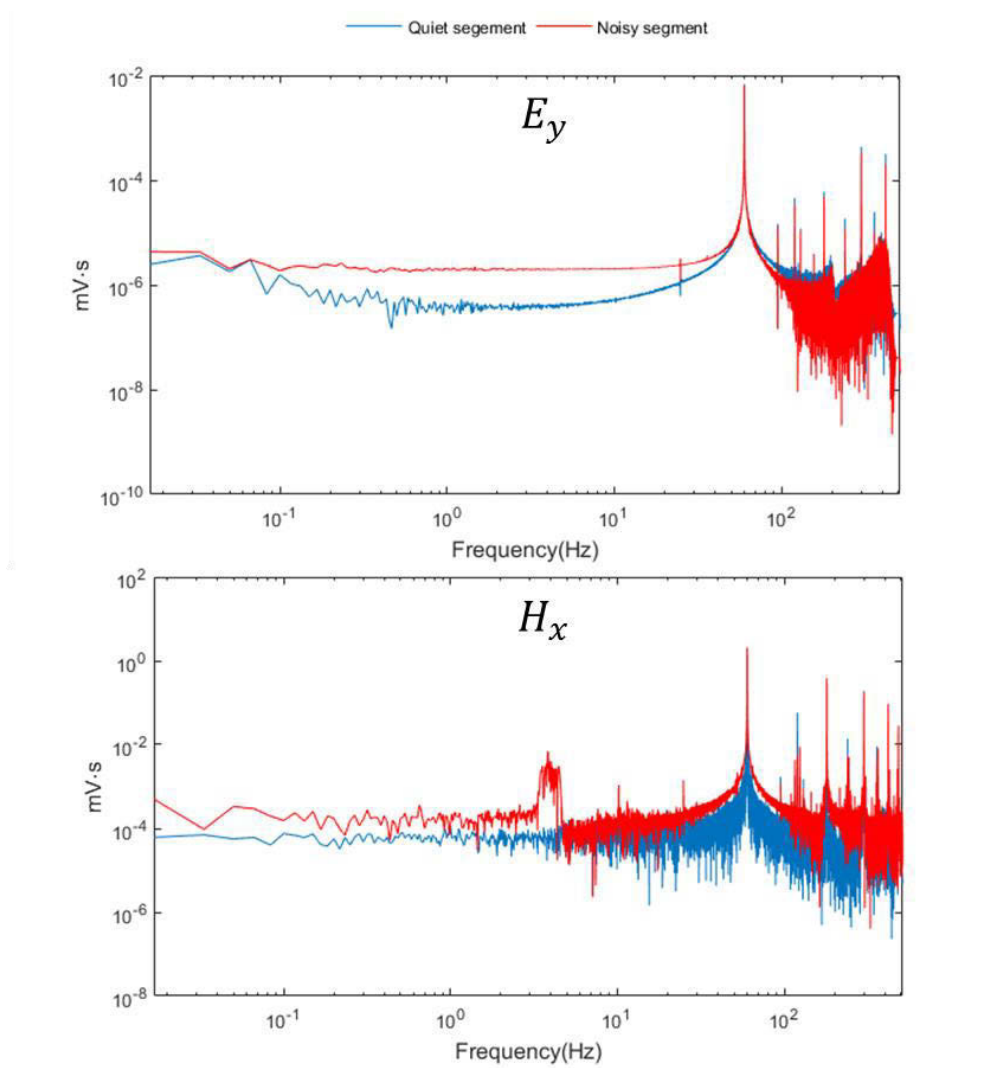


Figure I.7 FT results of the two segments of the electric field component E_y and the magnetic component H_x at site #4.

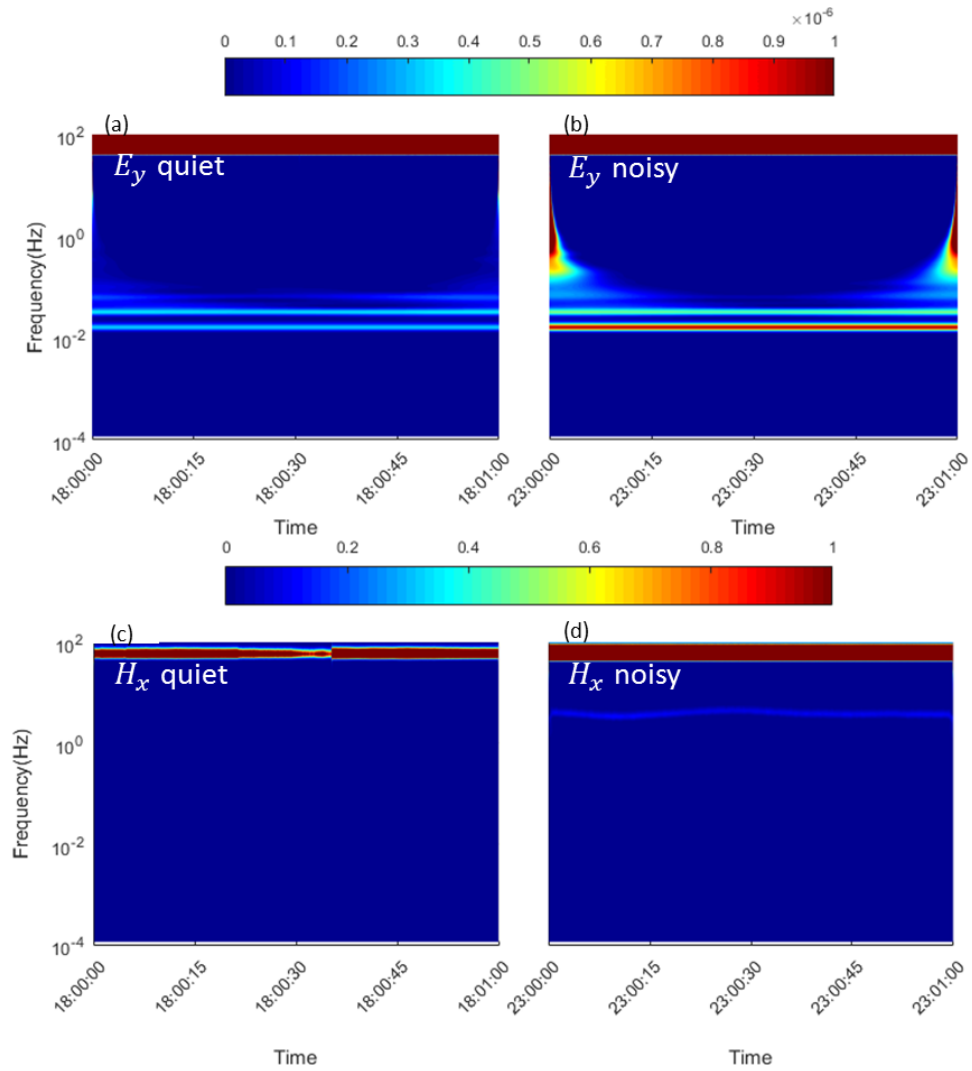


Figure I.8 Time-frequency representation of the two segments of the electric field component E_y and the magnetic component H_x from site #4.

I.5 Results of acquisition site #5

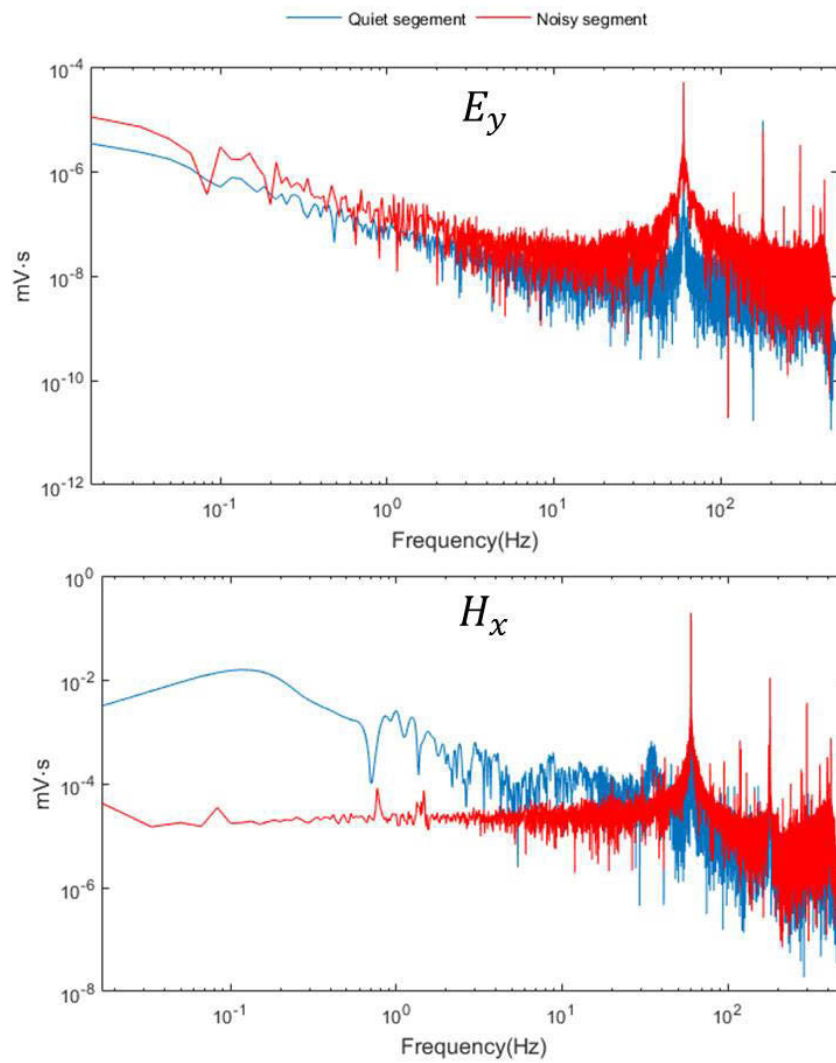


Figure I.9 FT results of the two segments of the electric field component E_y and the magnetic component H_x at site #5.

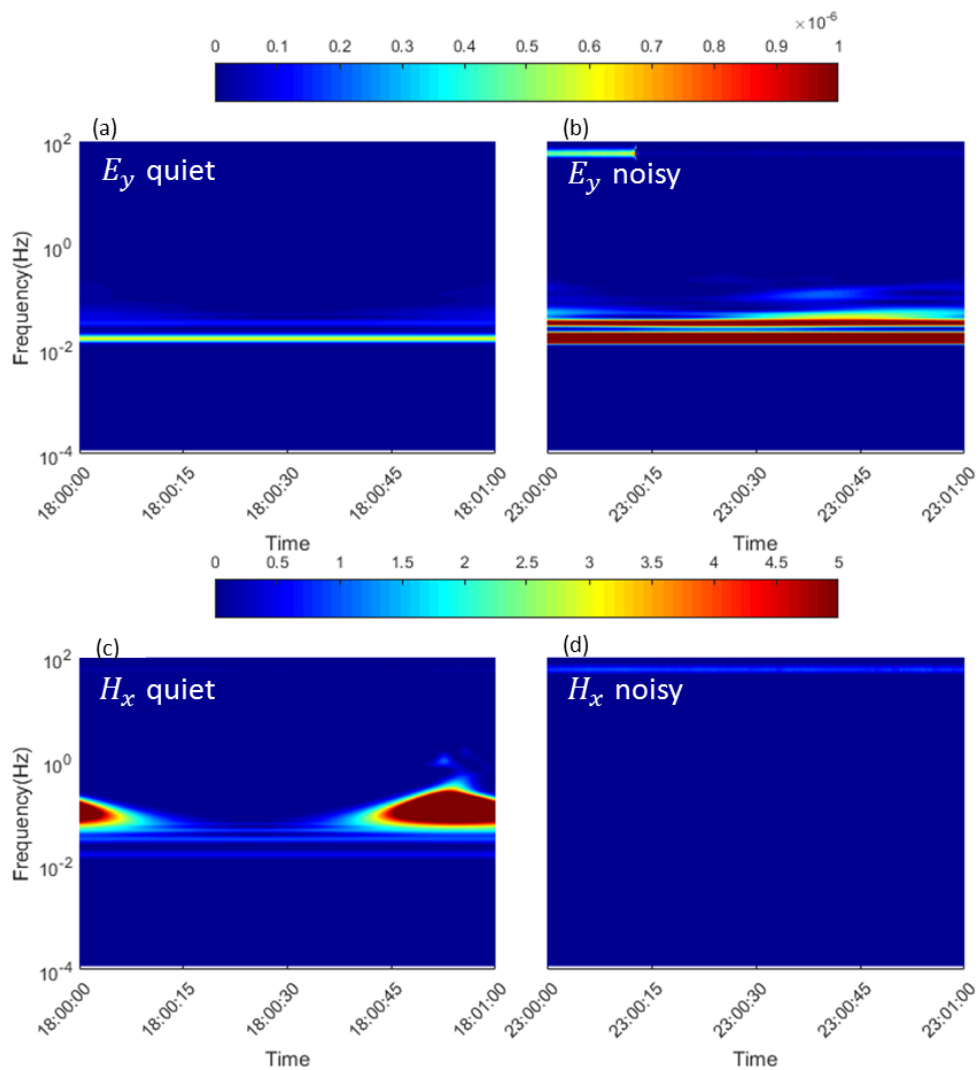


Figure I.10 Time-frequency representation of the two segments of the electric field component E_y and the magnetic component H_x from site #5.

APPENDIX II

MATLAB PROGRAMS FOR ANALYZING DATA COLLECTED IN GALLERIES AT THE LARONDE MINE

II.1 Main MATLAB program: LaRondeDataAnaly.m

% This function is main Matlab program used to analyze the data collected
% in the galleries at the LaRonde mine.

```
clearvars;
close all;
clc;
%% Read Zen data
Files = dir('*.z3d');
Fs = 1024;
ChNum = 1;
[Site,Info] = Get_data(Files, ChNum);
Time = cell(1,5); % generate time vectors for each site
for k = 1:5
    Time{k} = (0:1/Fs:(length(Site{k})-1)/Fs);
end

%% plot signal in time-domain
figure
axes('position',[0.1 0.86,0.85,0.13])
plot(Time{1}/10000,Site{1}*1000,'linewidth',1)
axis tight
axes('position',[0.1 0.68,0.85,0.13])
plot(Time{2}/10000,Site{2}*1000,'linewidth',1)
axis tight
axes('position',[0.1 0.5,0.85,0.13])
```

```

plot(Time{3}/10000,Site{3}*1000,'linewidth',1)
ylabel('Amplitud(mV/m)','fontsize',13)
axis tight
axes('position',[0.1 0.32,0.85,0.13])
plot(Time{4}/10000,Site{4}*1000,'linewidth',1)
axis tight
axes('position',[0.1 0.14,0.85,0.13])
plot(Time{5}/10000,Site{5}*1000,'linewidth',1)
xlabel('Time(s\times10^4)','fontsize',12)
axis tight
Filename = ['AllSites_',num2str(ChNum)];
print(Filename,'-dtiff','-r0')

%% to select segment from each site for the analysis
SiteStart = {'10:42:50','09:43:10','11:44:10','11:49:10','11:03:30'};
P1_Start = [18 00 00];
P1_End = [18 01 00];
P2_Start = [23 00 00];
P2_End = [23 01 00];
Section1 = cell(1,5);
Section2 = cell(1,5);
for k = 1:5
    Hour = str2double(SiteStart{k}(1:2));
    Minute = str2double(SiteStart{k}(4:5));
    Second = str2double(SiteStart{k}(7:8));
    temp1 = Fs*((P1_Start(1)-Hour)*3600+(P1_Start(2)-Minute)*60+P1_Start(3)-
Second);
    temp2 = Fs*((P1_End(1)-Hour)*3600+(P1_End(2)-Minute)*60+P1_End(3)-
Second);
    Section1{k} = Site{k}(temp1:temp2);
    temp1 = Fs*((P2_Start(1)-Hour)*3600+(P2_Start(2)-Minute)*60+P2_Start(3)-
Second);
    temp2 = Fs*((P2_End(1)-Hour)*3600+(P2_End(2)-Minute)*60+P2_End(3)-
Second);
    Section2{k} = Site{k}(temp1:temp2);
end

%% FFT analysis

figure
for k = 1:5
    Y = fft(Section1{k});

```

```

L = length(Section1 {k});
P2 = abs(Y/L);
P1 = P2(1:L/2+1);
P1(2:end-1) = 2*P1(2:end-1);
Freq = Fs*(0:(L/2))/L;
clf;
axes('position',[0.2 0.3 0.7 0.6])
loglog(Freq,P1)
xlim([0,512])
Y = fft(Section2 {k});
L = length(Section2 {k});
P2 = abs(Y/L);
P1 = P2(1:L/2+1);
P1(2:end-1) = 2*P1(2:end-1);
Freq = Fs*(0:(L/2))/L;
hold on
loglog(Freq,P1,'r-')
xlabel('Frequency(Hz)','fontsize',12)
ylabel('Amplitude','fontsize',12)
legend({'18:00:00-18:01:00','23:00:00-
23:01:00'},'box','off','location','northoutside','orientation','horizontal')
FileName = ['FFT_',num2str(k),'_CH',num2str(ChNum)];
print(FileName,'-dtiff','-r0')
end

%% CWT analysis
T0 = (P1_Start(1)-10)*3600+P1_Start(2)*60+P1_Start(3);
T1 = (P1_End(1)-10)*3600+P1_End(2)*60+P1_End(3);
Time1 = T0:1/Fs:T1;
T0 = (P2_Start(1)-10)*3600+P2_Start(2)*60+P2_Start(3);
T1 = (P2_End(1)-10)*3600+P2_End(2)*60+P2_End(3);
Time2 = T0:1/Fs:T1;
wname = 'morl';
f0 = centfrq(wname);

% generate scale vector for CWT analysis

scales = helperCWTimeFreqVector(1e-4,500,f0,1/Fs,32);
xticks1 =
[Time1(1),Time1(1+15360),Time1(1+15360*2),Time1(1+15360*3),Time1(1+15360
*4)];
xticklabels1 = {'18:00:00','18:00:15','18:00:30','18:00:45','18:01:00'};

```

```

xticks2 =
[Time2(1),Time2(1+15360),Time2(1+15360*2),Time2(1+15360*3),Time2(1+15360
*4)];
xticklabels2 = {'23:00:00','23:00:15','23:00:30','23:00:45','23:01:00'};
figure
for k = 1:5
    clf
    cwts = cwtft({Section1 {k},1/Fs},'wavelet',wname,'scales',scales);
    h1 = axes('position',[0.1 0.35 0.4 0.4]);
    surf(Time1,cwts.frequencies,abs(cwts.cfs).^2,'edgecolor','none');
    view(0,90)
    colormap jet
    text(Time1(1),220,'(a)')

set(h1,'XTick',xticks1,'XTickLabel',xticklabels1,'XTickLabelRotation',45,'yscale','log')
ylim([10^-4,100])
ylabel('Frequency(Hz)')
xlabel('Time')

    cwts = cwtft({Section2 {k},1/Fs},'wavelet',wname,'scales',scales);
    h2 = axes('position',[0.55 0.35 0.4 0.4]);
    surf(Time2,cwts.frequencies,abs(cwts.cfs).^2,'edgecolor','none');
    view(0,90)
    colormap jet
    cb = colorbar;
    set(cb,'location','north','position',[0.23 0.8 0.6 0.05])
    text(Time2(1),220,'(b)')

set(h2,'XTick',xticks2,'YTick',[],'XTickLabel',xticklabels2,'XTickLabelRotation',45,'
YScale','log')
ylim([10^-4,100])
xlabel('Time')
    Filename = ['CWT_Site#',num2str(k),'_CH',num2str(ChNum)];
    print(Filename,'-dtiff','-r0')

end

```

II.2 Functions

II.2.1 Get_data.m

```
function [Data,metadata]=Get_data(Files,ChNum)
```

```

% Function used to get data of a specific channel.
FNumber = size(Files,1);

for k = 1:FNumber
    Ch = str2double(Files(k).name(9));
    if Ch == ChNum
        switch Files(k).name(4:6)
            case '123'
                [Data{2},metadata{2}] = readZ3D(Files(k).name,1);
            case '124'
                [Data{1},metadata{1}] = readZ3D(Files(k).name,1);
            case '125'
                [Data{4},metadata{4}] = readZ3D(Files(k).name,1);
            case '126'
                [Data{5},metadata{5}] = readZ3D(Files(k).name,1);
            case '127'
                [Data{3},metadata{3}] = readZ3D(Files(k).name,1);
        end
    end
end
end

```

II.2.2 readZ3D.m

```

function [TS_data,metadata] ...
    = readZ3D(file,VFlag)

```

% Function to read raw data from *.Z3D files.

% inputs:

% file: filename of the *.Z3D file;

% VFlag: 0/1, 0-no unit, 1-the unit is volt.

% outputs:

% TS_data: data read from the *.Z3D file;

% metadat: basic information about the measurement.

% *note* this function is modified from a function provided by Wanjie Feng,

% who works at Zonge Inc.

```

tic

```

```

error_status=0;

```

```

Flag0=-1;

```

```

Flag1= 2147483647;
Flag2=-2147483648;
databytes=0;
ADC_freq=2097152; %ADC speed
AVr=2.048;
TS_start = 1;
TS_end = 0;

% INITIALISATION

TS_data=[];
TS_time=[];
GPS=[];
L_TS=[];

% READ Z3D FILE
fid = fopen(file);

% HEADER (512 bytes) ---Read the header information

header = fscanf(fid,'%c',512);
HEADER=textscan(header,'%s','delimiter','\n;,&');

%Firmware
metadata.version=str2double(parsing(HEADER{1,1},'Version','=',2));
%Firmware info
metadata.build_software=str2double(parsing(HEADER{1,1},'Main.hex','=',2));

%Hardware info
metadata.build_hardware=str2double(parsing(HEADER{1,1},'fpga','=',2));

metadata.Serial=parsing(HEADER{1,1},'ChannelSerial','=',2); %Ch SN.
metadata.channel=str2double(parsing(HEADER{1,1},'channel ','=',2)); %Ch NO.
metadata.ADfreq=str2double(parsing(HEADER{1,1},'rate','=',2)); %ADC rate
metadata.gain=log2(str2double(parsing(HEADER{1,1},'gain','=',2))); %Gain info

%Period
metadata.period=str2double(parsing(HEADER{1,1},'period','=',2));

%Duty
metadata.duty=str2double(parsing(HEADER{1,1},'duty','=',2));

%TX Freq

```

```

metadata.TXFreq=str2double(parsing(HEADER{1,1},'Tx.Freq','=',2));

%TX Duty
metadata.TXDuty=str2double(parsing(HEADER{1,1},'Tx.Duty','=',2));

metadata.latitude=str2double(parsing(HEADER{1,1},'lat','=',2));      %GPS Lat
metadata.longitude=str2double(parsing(HEADER{1,1},'long','=',2))    %GPS Lon
metadata.altitude=str2double(parsing(HEADER{1,1},'alt','=',2));     %GPS Alt
%NO. of Sat
metadata.Nbsat=str2double(parsing(HEADER{1,1},'NumSats','=',2))

%GPS week
metadata.GPSweek=str2double(parsing(HEADER{1,1},'gpsweek','=',2));
metadata.AttenChannelsMask=parsing(HEADER{1,1},'box
AttenChannelsMask','=',2);      %Ch mask.
metadata.Box_Nb=str2double(parsing(HEADER{1,1},'box
number','=',2));      %Box NO.
[~,metadata.ch_hardware] = strtok(parsing(HEADER{1,1},'GPS
Brd','Logfile',1));%GPS hardware info
metadata.ch_factor=str2double(parsing(HEADER{1,1},'Ch.Factor','=',2));
metadata.TX_Freq=str2double(parsing(HEADER{1,1},'Tx.Freq','=',2));
% Check if old Header version  %%
if isnan(metadata.channel)
    metadata.channel=str2double(parsing(HEADER{1,1},'channel','=',2));
end
if isempty(metadata.Serial)
    metadata.Serial=parsing(HEADER{1,1},'Serial','=',2);
end
%Calculate Period information
metadata.Serial=metadata.Serial(3:end);      %Ch serial number

% CALCULATE THE CALIBRATION KEY

% METADATA & CALIBRATION (512 bytes)
startbytes=0;
fseek(fid,startbytes, 'bof');
meta = fscanf(fid,'%c',8192);
META1=textscan(meta,'%s','delimiter','\n;,&');
metadata.Date=parsing(META1{1,1},'Schedule.Date','=',2);      %Schedule date
metadata.Time=parsing(META1{1,1},'Schedule.Time','=',2);      %Schedule date
metadata.Sync=parsing(META1{1,1},'Schedule.Sync','=',2);      %Schedule sync
metadata.RXSTN=str2double(parsing(META1{1,1},'CH.STN','=',2));
Frec=strfind(meta, 'GPS Brd339/Brd357 Metadata Record');

```

```

if ~isempty(Frec)
    %if METADATA
    META="";
    for i=1:length(Frec)
        content=deblank(meta(Frec(i)+34:Frec(i)+507));
        META=strcat(META, content);
    end

    meta2=textscan(META,'%s','delimiter','|');
    metadata.CMP = parsing(meta2{1,1},'CH.CMP','=',2);
    metadata.TX = parsing(meta2{1,1},'TX.ID','=',2);
    metadata.RX = parsing(meta2{1,1},'RX.STN','=',2);
    metadata.STN_ANT = str2double(parsing(meta2{1,1},'CH.NUMBER','=',2));
    metadata.A_spacing = str2double(parsing(meta2{1,1},'CH.VARASP','=',2));

% CAL %%

    CAL_BOARD=parsing(meta2{1,1},'CAL.SYS','=',2);
    AA=~cellfun('isempty',strfind(lower(meta2{1,1}),lower('CAL.SYS')));
    if sum(AA)~=0
        AAA=meta2{1,1}{AA,1};
        Z=textscan(AAA,'%s','delimiter','|');

        Z4=zeros(size(Z{1,1},1)-2,4);
        for i=3:size(Z{1,1},1)
            Z3=textscan(Z{1,1}{i,1},'%f %s %f %f','delimiter','|');
            STRING=Z3{1,2}{1,1};
            STRING1=STRING(9:16);
            ID1=uint64(hex2dec(STRING1));
            Z4(i-2,1)=ID1;
            Z4(i-2,2)=Z3{1,1};
            Z4(i-2,3)=Z3{1,3};
            Z4(i-2,4)=(pi/180).*Z3{1,4}.*1000; % phase degree --> milliradian
        end

        LOC_CAL= Z4(:,1)==hwklookup;
        CAL_TABLE=Z4(LOC_CAL,2:4);
        formatSpec = '%f:%d:%d';
        str = sprintf(formatSpec,CAL_TABLE(:,:));
        metadata.CAL=['CAL.SYS,' CAL_BOARD ' ' str(1:end-1)];
    else
        metadata.CAL=['CAL.SYS,' metadata.Serial ' ,1,0'];
    end
end

```

```

else

%if NO METADATA
metadata.TX=";
metadata.RX=";
metadata.STN_ANT=1;
metadata.CMP='Ex';
metadata.A_spacing=1;
metadata.CAL=['CAL.SYS,' metadata.Serial ',1,0'];

end

% GET OPTIMAL BUFFER SIZE %%
tic
% Get number of bytes of the file and length of the data record.

java_call = java.io.File(file);
bytes_size = length(java_call);

clear A_spacing AA ADC_freq altitude Avr CAL CAL_BOARD content meta meta2
clear duty Freq header HEADER META TX RX week coef FileName FilterIndex
clear GPSweek latitude longitude PathName period Serial startbytes STN_ANT

% Find first timestamp
fseek(fid,0, 'bof');

if (bytes_size/4>2^15)
    data=fread(fid,2^15,'uint8=>uint8');
else
    data=fread(fid,'uint8=>uint8');
end

% Find first second
found=0;ii=0;
while found==0
    ii=ii+1;
    if data(ii,1)==255 && data(ii+1,1)==255 && data(ii+2,1)==255 &&
data(ii+3,1)==127 ...
        && data(ii+4,1)==0 && data(ii+5,1)==0 && data(ii+6,1)==0 &&
data(ii+7,1)==128
        found=1;
    end
end

```

```

        if ii>bytes_size-10
            error_status=1;
            return;
        end

    end

offset=ii-1;          %offset for the first second

metadata.size=offset;

%Calculate the data block size
LL=floor(((bytes_size-databytes)-offset)/4) ;

power_size = nextpow2(LL+1)-1;

if power_size < 15
    data_block=2^12; % 4096 bytes
elseif power_size >= 15 && power_size < 17
    data_block=2^13; % 8182 bytes
elseif power_size >= 17 && power_size < 20
    data_block=2^15; % 32768 bytes
elseif power_size >= 20
    data_block=2^16; % 65536 bytes
end

%Define Nb of Buffer and size of the last buffer
block_number=floor(LL/data_block); % number of block
residual=LL-block_number*data_block; % residual bytes
residualbytes=databytes+(LL-residual)*4; % residual bytes location
databytes=offset;

%READ DATA
fseek(fid,0,'bof');
headerBIN = fread(fid,metadata.size);

%try

% Read buffer of data
fseek(fid,offset,'bof');
TS_data=int32(zeros(LL,1));
for i=1:block_number
    TS_data(data_block*(i-1)+1:data_block*(i),1)=fread ...

```

```

        (fid,data_block,'int32');
end

% Read residual
fseek(fid,residualbytes+offset,'bof');
TS_data(LL-residual+1:LL,1)=fread(fid,residual,'int32');

L_TS_data=size(TS_data,1);          %Size of TS data

% Close file
fclose(fid);

% Display status %
File_clock=toc;

% ORGANIZE DATA
% Get GPS informations

tic
i=0;

if metadata.build_software>=2828

    GPS=uint32(zeros(ceil(L_TS_data/metadata.ADfreq)+16,2));
    for j=1:L_TS_data-2
        if TS_data(j)==Flag1 && TS_data(j+1)==Flag2
            i=i+1;          % index increment
            GPS(i,2)=TS_data(j+2); % GPS time
            GPS(i,1)=j;      % Flag location (FF FF FF FF)
        end
    end

% Get GPS size

    GPS=GPS(TS_start:i-TS_end,:);
    L_GPS=size(GPS,1);

    GPS(1:end-1,3)=GPS(2:end,1)-GPS(1:end-1,1)-17;

else

    GPS=uint32(zeros(ceil(L_TS_data/metadata.ADfreq)+9,2));
    for j=1:L_TS_data-1

```

```

    if TS_data(j)==Flag0
        i=i+1;          % index increment
        GPS(i,2)=TS_data(j+1); % GPS time
        GPS(i,1)=j;    % Flag location (FF FF FF FF)
    end
end

% Get GPS size
GPS=GPS(TS_start:i-TS_end,:);
L_GPS=size(GPS,1);

% Generate GPS(:,3) = GPS(i+1,1)-GPS(i,1) (points between two GPS stamps)
GPS(1:end-1,3)=GPS(2:end,1)-GPS(1:end-1,1)-10;

end

GPS(end,3)=L_TS_data-GPS(end,1);

% Display status %
GPS_infos_clock=toc;

%%
ts_clock=tic;

pos=0; coef=0; week=0;
TS_time=double(zeros(sum(GPS(1:L_GPS-1,3))+1,1));
for i=1:L_GPS-1
    pos=pos+1;

    % Get GPS seconds
    GPStime_v=GPS(i,2)./1024;
    frac=(GPS(i,2)./1024-floor(GPS(i,2)./1024))*(1024/1000);

    % CONDITION IF WEEK CHANGE
    % If GPS second == 604800 (second in a week) then increment week
    if round(GPStime_v)==604800
        GPStime_v=0;
        week=week+1;
        coef=week*604800;
    end

    % If GPS second value is > 604800

```

```

if round(GPStime_v)>604800
GPStime_v=GPStime_v-604800;
end

% Get GPS seconds
GPS(i,2)=(floor(GPStime_v)+frac)+coef;

% % Clean 0/2 second timestamp issue.
% if i>1
% if GPS(i,2)~=GPS(i-1,2)+1
% GPS(i,2)=GPS(i-1,2)+1;
% end
% end

% GENERATE TS_data & % TS_time
if metadata.build_software>=2828
    TS_data(pos:pos+GPS(i,3),1)=TS_data(GPS(i,1)+16:GPS(i+1,1)-1);
else
    TS_data(pos:pos+GPS(i,3),1)=TS_data(GPS(i,1)+9:GPS(i+1,1)-1);
end

TS_time(pos:pos+GPS(i,3),1)=double(GPS(i,2))+(1/metadata.ADfreq)* ...
    double((0:GPS(i,3)));
pos=pos+GPS(i,3);
end

%added by Wanjie
pos=pos+1;
GPStime_v=GPS(end,2)./1024;
frac=(GPS(end,2)./1024-floor(GPS(end,2)./1024))*(1024/1000);
if round(GPStime_v)==604800
    GPStime_v=0;
    week=week+1;
    coef=week*604800;
end
if round(GPStime_v)>604800
    GPStime_v=GPStime_v-604800;
end
GPS(end,2)=(floor(GPStime_v)+frac)+coef;
if metadata.build_software>=2828
    TS_data(pos:pos+GPS(end,3)-16,1)=TS_data(GPS(end,1)+16:GPS(end,1)+...
        GPS(end,3));

```

```

else
    TS_data(pos:pos+GPS(end,3)-9,1)=TS_data(GPS(end,1)+9:GPS(end,1)+...
        GPS(end,3));
end

TS_time(pos:pos+GPS(end,3)-16,1)=double(GPS(end,2))+(1/metadata.Adfreq)* ...
    double((0:GPS(end,3)-16)');
pos=pos+GPS(end,3)-16;

```

```

L_TS=pos;
TS_data=TS_data(1:L_TS);
if(VFlag==1)
    TS_data=single(TS_data).*metadata.ch_factor;
else
    TS_data=TS_data;
end

% Display status %

ts_clock=toc(ts_clock);

%ERROR SUMMARY

try

    err1=find(GPS(TS_start+1:end-TS_end,3)~=metadata.Adfreq-1); %% Block
    Error (sec.)

    if ~isempty(err1)
        err1(:,2)=GPS(err1(:,1),2)-floor(GPS(1,2)); %% Time from start
        err1(:,3)=GPS(err1(:,1),2); %% Time (GPS)
        err1(:,4)=GPS(err1(:,1),3); %% Number(s) of points in the Error block
        err1(:,5)=-((metadata.Adfreq)-err1(:,4)); %% Less/Extra points
        err1(:,6)=databytes+GPS(err1(:,1),1)*4+4;
        b=err1(:,5)~-1;
        err=err1(b,:);
        a=(err1(:,5)=-1); %% Add the second part if +1 is needed.
        err_minus=err1(a,:);
    end

```

```

else
err=[];
err_minus=[];
end

% TIMESTAMP ERROR

% Gps time check
delta=zeros((length(GPS)-1),1);
if size(GPS,1)>2
    for i=1:length(GPS)-1
        delta(i,1)=GPS(i+1,2)-GPS(i,2);
    end

% find where there is not a second between 2 bloc
% and where timestamp value is twice the same.
    err_t(:,1)=unique([find(delta~=1);find(round(GPS(:,2))~=GPS(:,2),2)]);
    err_t(:,2)=GPS(err_t(:,1),2);
    err_t(1:end-1,3)=GPS(err_t(1:end-1,1)+1,2);
    if isempty(err_t)==0
        if GPS(end,2)-GPS(err_t(end,1),2)==0
            err_t(end,3)=NaN;
        else
            err_t(end,3)=GPS(err_t(end,1)+1,2);
        end
    end
    err_t(:,4)=err_t(:,3)-err_t(:,2);
    err_t(:,5)=(err_t(:,4)-1);
    err_t(:,7)=err_t(:,5)./(1/metadata.ADfreq);
    err_t(:,6)=databytes+GPS(err_t(:,1),1)*4+4;

end

catch error
    msg=['data_readZ3D Could not read (error in ERROR ANALYSIS) :' file];
    disp(error)
    errordlg(msg,'File Error');
    error_status=1;
    toc
    return;
end

```

II.2.3 helperCWTTIMEFREQVECTOR.M

```
function scales = helperCWTTIMEFREQVECTOR(minfreq,maxfreq,f0,dt,NumVoices)
```

```
% scales = helperCWTTIMEFREQVECTOR(minfreq,maxfreq,f0,dt,NumVoices)
% minfreq = minimum frequency in cycles/unit time. minfreq must be
% positive.
% maxfreq = maximum frequency in cycles/unit time
% f0 - center frequency of the wavelet in cycles/unit time
% dt - sampling interval
% NumVoices - number of voices per octave
%
% Note: This function used in an example in the wavelet toolbox in Matlab
```

```
a0 = 2^(1/NumVoices);
minscale = f0/(maxfreq*dt);
maxscale = f0/(minfreq*dt);
minscale = floor(NumVoices*log2(minscale));
maxscale = ceil(NumVoices*log2(maxscale));
scales = a0.^(minscale:maxscale).*dt;
```

II.2.4 parsing.m

```
function [ VARIABLE ] = parsing( CELL,STRING,DELIMITER,POSITION )
```

```
A=~cellfun('isempty',strfind(lower(CELL),lower(STRING)));
if sum(A)~=0
AA=CELL{A,1};
Z=textscan(AA,'%s','delimiter',DELIMITER);
if size(Z{1,1},1)<POSITION
VARIABLE=";
else
VARIABLE=Z{1,1}{POSITION,1};
end
else
VARIABLE=";
end
end
```

II.2.5 Fourier.m

```
function [P, Freq] = Fourier(X,Fs)
```

```
% Function used to calculate the Fourier transform of a signal  
% required inputs are: the signal (X) and the sampling frequency (Fs)  
% outputs include the single sided spectrum (P) and the frequencies (Freq)
```

```
Y = fft(X);  
L = length(X);  
P2 = abs(Y/L);  
P = P2(1:L/2+1);  
P(2:end-1) = 2*P(2:end-1);  
Freq = Fs*(0:(L/2))/L;
```

```
end
```

APPENDIX III

MATLAB PROGRAMS FOR VALIDATING THE DENOISING METHOD ON SYNTHETIC AND FIELD DATA

III.1 Main MATLAB program: ValidationOnSyntheticData.m

```
close all;
clearvars;
clc;

% this program is used to test the effectiveness of the denoising method on
% synthetic BHTEM signals
%% Synthetic signal preparation

fid = fopen('Data_10512.txt'); %%component order: z, x, y
fgetl(fid);
z = fscanf(fid,'%f',[47,91]);
DataZ = z(:,5:47);
Stations = abs(z(:,4));
fgetl(fid);
fgetl(fid);
x = fscanf(fid,'%f',[47,91]);
DataX = x(:,5:47);
fgetl(fid);
fgetl(fid);
y = fscanf(fid,'%f',[47,91]);
DataY = y(:,5:47);
fclose(fid);
figure
subplot(3,1,1)
for k = 1:1:43
    plot(Stations,DataZ(:,k),'k-', 'linewidth',0.8)
    hold on
```

```

end
xlabel('Depth(m)');ylabel('nT/s');
title('A-component')
subplot(3,1,2)
for k = 1:1:43
    plot(Stations,DataX(:,k),'k-','linewidth',0.8)
    hold on
end
xlabel('Depth(m)');ylabel('nT/s');
title('U-component')
subplot(3,1,3)
for k = 1:1:43
    plot(Stations,DataY(:,k),'k-','linewidth',0.8)
    hold on
end

%% NOISE-FREE SIGNAL

fid = fopen('ChIfor.chn'); % get channel information of the SmarTem 24
fgetl(fid)
fgetl(fid)
fgetl(fid)
CHInfor = fscanf(fid,'%f\r\n',[2,43]);
fclose(fid);
t_beg = CHInfor(1,:);
t = linspace(0.01,1000,24000);
m = size(DataX,1);
SignalX = zeros(m,24000);
SignalY = zeros(m,24000);
SignalZ = zeros(m,24000);
for k = 1:m
    SignalZ(k,:) = interp1(t_beg,DataZ(k,:),t,'linear','extrap');
    SignalX(k,:) = interp1(t_beg,DataX(k,:),t,'linear','extrap');
    SignalY(k,:) = interp1(t_beg,DataY(k,:),t,'linear','extrap');
end
Signal = -SignalX(51,:)*20+1;
figure
axes('position',[0.3,0.3,0.5,0.5])
loglog(t,Signal,'k-','linewidth',0.1)
xlim([0,1000])
ylim([0.1,100])
xlabel('Time(ms)','fontsize',12)
ylabel('nT/s','fontsize',12)

```

```

%% GENERATE NOISE
% -----sferics noise-----%

Sferics = load('Sferics.txt');
Sferics1 = Sferics(30,:)/200;
Sferics2 = Sferics(200,:)/200;
Sferics3 = Sferics(600,:)/200;
Sferics4 = Sferics(700,:)/200;
Mega30 = [0.326,1.02,2.105,3.32,4.08,4.275,4.427,4.622,4.883,5.208,5.599,...
    6.076,6.641,7.292,8.073,9.028,10.2,11.632,13.325,15.451];
NoInter = 381;
tSferics = linspace(0.13,16.667,NoInter);
NoiseSF1 = interp1(Mega30,Sferics1,tSferics,'linear','extrap');
NoiseSF2 = interp1(Mega30,Sferics2,tSferics,'linear','extrap');
NoiseSF3 = interp1(Mega30,Sferics3,tSferics,'linear','extrap');
NoiseSF4 = interp1(Mega30,Sferics4,tSferics,'linear','extrap');
NoiseSF = zeros(1,24000);
NoiseSF(200:200+NoInter-1) = NoiseSF(200:200+NoInter-1)+NoiseSF1;
NoiseSF(8000:8000+NoInter-1) = NoiseSF(8000:8000+NoInter-1)+NoiseSF2;
NoiseSF(16000:16000+NoInter-1) = NoiseSF(16000:16000+NoInter-1)+NoiseSF3;
NoiseSF(20000:20000+NoInter-1) = NoiseSF(20000:20000+NoInter-1)+NoiseSF4;
NoiseSF = NoiseSF/10;
figure
axes('position',[0.1,0.4,0.85,0.25])
plot(t,NoiseSF,'k-','linewidth',0.8)
ylabel('nT/s','fontsize',10)
title('Sferics')
set(gca,'xticklabel',[])

% -----random noise-----%

NoiseRND = randn(size(Signal))/2;
axes('position',[0.1,0.7,0.85,0.25])
plot(t,NoiseRND,'k-','linewidth',0.8)
ylim([-2,2])
title('Random noise')
set(gca,'xticklabel',[])

% -----noise from power line (60 Hz and 50 Hz)-----%

NoisePL = 0.1*(sin(2*pi*0.06*t)+sin(2*pi*0.05*t));
axes('position',[0.1,0.1,0.85,0.25])

```

```

plot(t,NoisePL,'k-', 'linewidth',0.8)
title('Noise induced by the power line')
xlabel('Time(ms)', 'fontsize',10)

%% GENERATE NOISY SIGNAL

Noise = NoisePL+NoiseSF+NoiseRND;
SNR = 25; % objective SNR for the noisy signal
SignalNoisy = AddNoise(Signal, Noise, SNR);
figure
axes('position',[0.1,0.3,0.4,0.4])
loglog(t,SignalNoisy,'k-', 'linewidth',0.8)
xlim([0,1000])
ylim([0.1,100])
xlabel('Time(ms)', 'fontsize',12)
ylabel('nT/s', 'fontsize',12)
title('Noisy signal')
wname = 'sym5';
lvl = 10;
WTDenoised = DWTDenoise(SignalNoisy, wname, 8, lvl);
SNRWT = CalSNR(WTDenoised,Signal);
axes('position',[0.58,0.3,0.4,0.4])
loglog(t,Signal,'r-', 'linewidth',1)
hold on
loglog(t,WTDenoised,'k-', 'linewidth',1)
hold off
legend({'Original signal','DWT processed
signal'}, 'fontsize',8, 'location',[0.73,0.63,0.18,0.05], 'box','off')
xlim([0,1000])
ylim([0.1,100])
xlabel('Time(ms)', 'fontsize',12);
title('The DWT denoised result Vs the orignal signal')

%% CURVE FIT DENOISE

[Peaks, Valleys] = PeaksAndValleys(WTDenoised,0.03);
NumPeaks = size(Peaks,1);
tPeaks = t(Peaks(:,2));
tValleys = t(Valleys(:,2));
Newsignal = CurveFitting(WTDenoised,t,Peaks,Valleys);
SNRF = CalSNR(Newsignal,Signal);
figure

```

```

axes('position',[0.3,0.3,0.5,0.5])
loglog(t,Signal,'r-','linewidth',1)
hold on
loglog(t,WTDenoised,'k-','linewidth',1)
loglog(t,Newsignal,'b-','linewidth',1)
xlim([0,1000])
ylim([0.1,100])
title({'Demonstrating the effectiveness of, 'the curve fitting method'})
xlabel('Time(ms)','fontsize',12);ylabel('nT/s','fontsize',12)
legend({'Original signal','DWT processed signal','CFT introduced'}...
    , 'fontsize',8,'location',[0.55,0.71,0.2,0.05],'box','off')

```

```

%%% ERROR CURVE
ErrorNoisy = abs((SignalNoisy-Signal)./Signal);
ErrorWTD = abs((WTDenoised-Signal)./Signal);
ErrorCFT = abs((Newsignal-Signal)./Signal);
figure
axes('position',[0.1 0.75 0.8 0.2])
plot(t,ErrorNoisy,'k','linewidth',0.8)
xlabel('Time(ms)','fontsize',10)
ylim([0 1])
title('Error curve of the noisy signal')
axes('position',[0.1 0.425 0.8 0.2])
plot(t,ErrorWTD,'k','linewidth',0.8)
ylim([0 1])
title('Error curve of the DWT denoised signal')
xlabel('Time(ms)','fontsize',10)
axes('position',[0.1 0.1 0.8 0.2])
plot(t,ErrorCFT,'k','linewidth',0.8)
ylim([0 1])
xlabel('Time(ms)','fontsize',10)
title('Error curve of signal obtained by the DWT+Curve fitting')
MSEWTD = sum((WTDenoised-Signal).^2)/24000;
MSECFT = sum((Newsignal-Signal).^2)/24000;
MSENoisy = sum((SignalNoisy-Signal).^2)/24000;

```

III.2 Main MATLAB program: ValidationOnFieldData.m

```

% this program is used to process field data with the method.

```

```

clearvars;
close all;

```

```

clc;

FileInfo = cell(96,1);
wname = 'sym5';
lvl = 10;
Point = 8;
t = linspace(0,1000,24000);

Filename =
'15N014_12EA256_Lp12EA311_500x500_2turns_24April2015_20150424_184408.
0000000_V_2_34.raw';
fid = fopen(Filename,'r');

%-----Get raw data from the file-----%

for kk = 1:96
    FileInfo{kk} = fgetl(fid);
    a = strfind(FileInfo{kk}, '<');
    b = strfind(FileInfo{kk}, '>');
    if strcmp(FileInfo{kk}(a(1)+1:b(1)-1), 'ReadingNumber')
        ReadingNumber = str2double(FileInfo{kk}(b(1)+1:a(2)-1));
    elseif strcmp(FileInfo{kk}(a(1)+1:b(1)-1), 'SampleRate')
        SampleRate = str2double(FileInfo{kk}(b(1)+1:a(2)-1));
    elseif strcmp(FileInfo{kk}(a(1)+1:b(1)-1), 'Freq')
        Freq = str2double(FileInfo{kk}(b(1)+1:a(2)-1));
    elseif strcmp(FileInfo{kk}(a(1)+1:b(1)-1), 'DataFormat')
        DataFormat = ['bit', FileInfo{kk}(b(1)+2:a(2)-10)];
    elseif strcmp(FileInfo{kk}(a(1)+1:b(1)-1), 'scale')
        Scale = str2double(FileInfo{kk}(b(1)+1:a(2)-1));
    elseif strcmp(FileInfo{kk}(a(1)+1:b(1)-1), 'NullingVoltage')
        NV = str2double(FileInfo{kk}(b(1)+1:a(2)-1));
    elseif strcmp(FileInfo{kk}(a(1)+1:b(1)-1), 'volt_offset')
        Volt_offset = str2double(FileInfo{kk}(b(1)+1:a(2)-1));
    elseif strcmp(FileInfo{kk}(a(1)+1:b(1)-1), 'SysGain')
        SysGain = str2double(FileInfo{kk}(b(1)+1:a(2)-1));
    elseif strcmp(FileInfo{kk}(a(1)+1:b(1)-1), 'y_zero_volt_offset')
        y_zero = str2double(FileInfo{kk}(b(1)+1:a(2)-1));
    end
end
fgetl(fid);

Raw = fread(fid, DataFormat);
Raw = 1000*(Raw*Scale-Volt_offset);

```

```

fclose(fid);
L = length(Raw);
Raw = reshape(Raw,[SampleRate,L/SampleRate]);

%% Processing
StackDepth = 0.5*L/SampleRate;
Ontime = Raw(:,1:2:end);
Offtime = Raw(:,2:2:end);
DenoisedOntime = DWTDenoise(Ontime,wname,Point,lvl);
DenoisedOfftime = DWTDenoise(Offtime,wname,Point,lvl);

StackOntime = HalversonStack(Ontime,StackDepth);
StackOfftime = HalversonStack(Offtime,StackDepth);
StackRaw = [StackOntime,StackOfftime];

StackOntime = HalversonStack(DenoisedOntime,StackDepth);
StackOfftime = HalversonStack(DenoisedOfftime,StackDepth);
StackDenoised = [StackOntime,StackOfftime];

ImprovedOfftime = DenoisedOfftime;
ImprovedOntime = DenoisedOntime;
figure
set(gcf,'units','normalized','outerposition',[0.1 0.1 0.7 0.8])
for kk = 1:StackDepth
    plot(1+(2*kk-2)*24000:(2*kk-1)*24000,DenoisedOntime(:,kk),'r-')
    hold on
    plot(1+(2*kk-1)*24000:2*kk*24000,DenoisedOfftime(:,kk),'b-')
    text((2*kk-1)*24000,min(DenoisedOfftime(:,kk)),num2str(kk))
end

%% Correlation analysis

Breaks = input('Please enter the break points (separate by space, return to finish):');
Percentage = input('Please enter the percentage of data to be improved (0.1 for 10%,
return to finish):');
NB = length(Breaks);

if NB == 0
    ImprovedOfftime = CorrelationAnaly(ImprovedOfftime,Percentage);
    ImprovedOntime = CorrelationAnaly(ImprovedOntime,Percentage);
else
    ImprovedOfftime(:,1:Breaks(1)) =
    CorrelationAnaly(ImprovedOfftime(:,1:Breaks(1)),Percentage);

```

```

    ImprovedOntime(:,1:Breaks(1)) =
CorrelationAnaly(ImprovedOntime(:,1:Breaks(1)),Percentage);
    ImprovedOfftime(:,Breaks(end)+1:end) =
CorrelationAnaly(ImprovedOfftime(:,Breaks(end)+1:end),Percentage);
    ImprovedOntime(:,Breaks(end)+1:end) =
CorrelationAnaly(ImprovedOntime(:,Breaks(end)+1:end),Percentage);
    if NB>=2
        for kk = 2:NB
            ImprovedOfftime(:,Breaks(kk-1)+1:Breaks(kk)) =
CorrelationAnaly(ImprovedOfftime(:,Breaks(kk-1)+1:Breaks(kk)),Percentage);
            ImprovedOntime(:,Breaks(kk-1)+1:Breaks(kk)) =
CorrelationAnaly(ImprovedOntime(:,Breaks(kk-1)+1:Breaks(kk)),Percentage);
        end
    end
end

%% Save figures
figure
axes('position',[0.15,0.69,0.8,0.28])
for kk = 1:StackDepth
    plot(1+(2*kk-2)*SampleRate:(2*kk-1)*SampleRate,Ontime(:,kk),'r-
','linewidth',0.8)
    hold on
    plot(1+(2*kk-1)*SampleRate:(2*kk)*SampleRate,Offtime(:,kk),'k-','linewidth',0.8)
end
axis tight
xticklabels({})

axes('position',[0.15,0.395,0.8,0.28])
for kk = 1:StackDepth
    plot(1+(2*kk-2)*SampleRate:(2*kk-1)*SampleRate,DenoisedOntime(:,kk),'r-
','linewidth',0.8)
    hold on
    plot(1+(2*kk-1)*SampleRate:(2*kk)*SampleRate,DenoisedOfftime(:,kk),'k-
','linewidth',0.8)
end
xticklabels({})
ylabel('mV','fontsize',12)
axis tight

axes('position',[0.15,0.104,0.8,0.28])
for kk = 1:StackDepth

```

```

    plot(1+(2*kk-2)*SampleRate:(2*kk-1)*SampleRate,ImprovedOnTime(:,kk),'r-
','linewidth',0.8)
    hold on
    plot(1+(2*kk-1)*SampleRate:(2*kk)*SampleRate,ImprovedOffTime(:,kk),'k-
','linewidth',0.8)
end
legend({'On time','Off
time'},'fontsize',8,'location',[0.7,0.96,0.2,0.05],'orientation','horizontal','box','off')
xlabel('Samples','fontsize',12)
axis tight
text([0.03,0.03,0.03],[3,1.95,0.93],{'(a)','(b)','(c)'},'unit','normalized')
idx = strfind(Filename,'_');
FNR = [Filename(idx(5)+1:idx(6)),Filename(idx(8)+1:end-4),'_RAW'];
print(FNR,'-dtiff','-r0')

StackOnTime = HalversonStack(ImprovedOnTime,StackDepth);
StackOffTime = HalversonStack(ImprovedOffTime,StackDepth);
StackImproved = [StackOnTime,StackOffTime];
P0 = 1;
figure
axes('position',[0.15,0.2,0.7,0.7])
plot(t(P0:end),StackRaw(P0:end,2),'k-','linewidth',1)

hold on
plot(t(P0:end),StackDenoised(P0:end,2),'r-','linewidth',1)
plot(t(P0:end),StackImproved(P0:end,2),'b-','linewidth',1)

xlabel('Time(ms)','fontsize',12);
ylabel('mV','fontsize',12)
legend('Original raw data','DWT denoised raw data','DWT+correlation
analysis','location','northoutside','box','off')
FNSR = [Filename(idx(5)+1:idx(6)),Filename(idx(8)+1:end-4),'_OFF_STK'];
print(FNSR,'-dtiff','-r0')

figure
axes('position',[0.15,0.2,0.7,0.7])
plot(t(P0:end),StackRaw(P0:end,1),'k-','linewidth',1)

hold on
plot(t(P0:end),StackDenoised(P0:end,1),'r-','linewidth',1)
plot(t(P0:end),StackImproved(P0:end,1),'b-','linewidth',1)

xlabel('Time(ms)','fontsize',12);

```

```

ylabel('mV','fontsize',12)
legend('Original raw data','DWT denoised raw data','DWT+correlation
analysis','location','northoutside','box','off')
FNSR = [Filename(idx(5)+1:idx(6)),Filename(idx(8)+1:end-4),'_ON_STK'];
print(FNSR,'-dtiff','-r0')

```

III.3 Functions

III.3.1 DWTDenoise.m

```

function SigDenoised = DWTDenoise(signal, wname, Point, lvl)

% This function is to implement the DWT denoising process.
% input:
%   signal: the signal to be denoised;
%   wname: the wavelet name chosen for the DWT decomposition;
%   Point: the amount of detail coefficients to be kept unchanged;
%   lvl: the decomposition level to which the signal is to be
%   decomposed.
% output:
%   SigDenoised: the denoised signal.

[m,n] = size(signal);
SigDenoised = zeros(m,n);
NoM = min(m,n);

for k = 1:NoM
    if m>n
        [coefs, longs] = wavedec(signal(:,k),lvl,wname);
    else
        [coefs, longs] = wavedec(signal(k,:),lvl,wname);
    end
    first = cumsum(longs)+1;
    first = first(end-2:-1:1);
    tmp = longs(end-1:-1:2);
    last = first+tmp-1;

    for kk = 1:lvl
        cfs = coefs(first(kk):last(kk));
        cfs(Point:end) = 0;
        coefs(first(kk):last(kk)) = cfs;
    end
end

```

```

    if m>n
        SigDenoised(:,k) = waverec(coefs,longs,wname);
    else
        SigDenoised(k,:) = waverec(coefs,longs,wname);
    end

end

III.3.2 CurveFitting.m
function NewSignal = CurveFitting(Signal,t,Peaks,Valleys)

% This function is used to implement curve fitting process on signals
% denoised by the DWT.
% inputs:
% Signal: the signal denoised by the DWT;
% t: time series corresponding to Signal;
% Peaks/Valleys: the output of the function PeaksAndValleys.m.
% output:
% NewSignal: the curve fitted result.

NewSignal = Signal;
Npts = length(Signal);
PksVlys = [Peaks;Valleys];
PksVlys = sortrows(PksVlys,2);
FSP = PksVlys(1,2)-round(PksVlys(1,3));
FEP = PksVlys(end,2)+round(PksVlys(end,3));
if FSP>10
    FTime1 = t(FSP-10:FSP)';
    FValue1 = Signal(FSP-10:FSP)';
else
    FTime1 = t(1:FSP)';
    FValue1 = Signal(1:FSP)';
end
if (Npts-FEP)>10
    FTime2 = t(FEP:FEP+10)';
    FValue2 = Signal(FEP:FEP+10)';
else
    FTime2 = t(FEP:end)';
    FValue2 = Signal(FEP:end)';
end
FTime3 = [t(Peaks(:,2))';t(Valleys(:,2))']';
FTime = [FTime1;FTime3;FTime2];

```

```

FValue3 = [Peaks(:,1)-0.5*Peaks(:,4);Valleys(:,1)+0.5*Valleys(:,4)];
FValue = [FValue1;FValue3;FValue2];
FPoint = [FTime,FValue];
FModel = fit(FPoint(:,1),FPoint(:,2),'exp2');
SP = min([Peaks(:,2);Valleys(:,2)])-round(PksVlys(1,3));
EP = max([Peaks(:,2);Valleys(:,2)])+round(PksVlys(end,3)/2);
NewSignal(SP:EP) = FModel(t(SP:EP));

```

```
end
```

III.3.3 PeaksAndValleys.m

```
function [Peaks, Valleys] = PeaksAndValleys(y, value)
```

```

% This function is used to find extrema and to estimate the width of
% peaks/valleys.
% inputs:
% y: the signal
% value: the minimum prominence value
% outputs:
% Peaks/Valleys: two matrix of four columns:values, location, width,
% and prominence values

```

```

[pks1, locs1, width1, prominence1] = findpeaks(y,'minpeakprominence',value);
Peaks = [pks1', locs1', width1', prominence1'];
[pks2, locs2, width2, prominence2] = findpeaks(max(y)-
y,'minpeakprominence',value);
pks2 = max(y)-pks2;
Valleys = [pks2', locs2', width2', prominence2'];

```

```
end
```

III.3.4 CorrelationAnaly.m

```
function Improved = CorrelationAnaly(Data, Percentage)
```

```

% This function is used to carried out correlation analysis
% inputs:
% Data: the data set to be analyzed
% Percentage: the percentage of transients to be considered as distorted.
% output:
% Improved: the data set with distortions corrected.

```

```
Improved = Data;
```

```

[m,n] = size(Data);
x = 1:n;
x1 = x(1:2:end);
x2 = x(2:2:end);
coefs = corrcoef(Data(:,1:2:end));
ave1 = mean(coefs,1);
coefs = corrcoef(Data(:,2:2:end));
ave2 = mean(coefs,1);
if and(min(ave1)>0.9,min(ave2)>0.9)

%   fprintf('No need to improve!\n')

    return
elseif min(ave1)>0.9
    [~,index] = sort(ave2);
    num = fix(Percentage*(length(x2)))+1;
    idx = index(1:num);
    xq2 = x2(idx);
    x2(idx) = [];
    Temp = Improved(:,2:2:end);
    Temp(:,idx) = [];
    for k = 1:m
        v = Temp(k,:);
        Improved(k,2*idx) = interp1(x2,v,xq2,'linear','extrap');
    end
elseif min(ave2)>0.9
    [~,index] = sort(ave1);
    num = fix(Percentage*(length(x1)))+1;
    idx = index(1:num);
    xq1 = x1(idx);
    x1(idx) = [];
    Temp = Improved(:,1:2:end);
    Temp(:,idx) = [];
    for k = 1:m
        v = Temp(k,:);
        Improved(k,2*idx-1) = interp1(x1,v,xq1,'linear','extrap');
    end
else
    [~,index] = sort(ave1);
    num = fix(Percentage*(length(x1)))+1;
    idx = index(1:num);
    xq1 = x1(idx);
    x1(idx) = [];

```

```

Temp = Improved(:,1:2:end);
Temp(:,idx) = [];
for k = 1:m
    v = Temp(k,:);
    Improved(k,2*idx-1) = interp1(x1,v,xq1,'linear','extrap');
end

[~,index] = sort(ave2);
num = fix(Percentage*(length(x2)))+1;
idx = index(1:num);
xq2 = x2(idx);
x2(idx) = [];
Temp = Improved(:,2:2:end);
Temp(:,idx) = [];
for k = 1:m
    v = Temp(k,:);
    Improved(k,2*idx) = interp1(x2,v,xq2,'linear','extrap');
end

end

end

```

REFERENCES

- Agnico Eagle Ltd. LaRonde Division, 2005, 2005 LaRonde mineral resource & mineral reserve estimate.
- Agnico Eagle Ltd., 2017, Annual information form for the year ended December 31, 2016.
- Agnico Eagle website : <https://www.agnicoeagle.com/English/operations-and-development-projects/operations/laronde/default.aspx>.
- Akansu, A.N., Haddad, P.A., Haddad, R.A. and Haddad, P.R., 2001. Multiresolution signal decomposition: transforms, subbands, and wavelets. Academic press.
- Asten, M.W., 2001. Borehole EM and MMR Methods for Weak Conductors—A Project Review. ASEG Extended Abstracts, 2001(1), pp.1-4.
- Augustin, A.M., Kennedy, W.D., Morrison, H.F. and Lee, K.H., 1989. A theoretical study of surface-to-borehole electromagnetic logging in cased holes. *Geophysics*, 54(1), pp.90-99.
- Barnett, C.T. and Williams, P.M., 2006, Mineral exploration using modern data mining techniques: First break, 24(7).
- Bartel, D.C. and Hohmann, G.W., 1985, Interpretation of Crone pulse electromagnetic data. *Geophysics*, 50(9), 1488-1499.
- Bloomfield, P., 2004, Fourier analysis of time series: an introduction. John Wiley & Sons.
- Boggess, A. and Narcowich, F.J., 2015. A first course in wavelets with Fourier analysis. John Wiley & Sons.
- Boivin, M. and Milkereit, B., 2007, Advances in geophysical technology for VMS exploration: in Exploration in the New Millenium Proceedings Fifth Decennial International Conference on Mineral Exploration, Decennial Mineral Exploration Conferences, Toronto, 731-739.

- Bouchedda, A., Chouteau, M., Keating, P. and Smith, R., 2010. Sferics noise reduction in time-domain electromagnetic systems: application to MegaTEMII signal enhancement. *Exploration Geophysics*, 41(4), pp.225-239.
- Boukerbout, H. and Gibert, D., 2006. Identification of sources of potential fields with the continuous wavelet transform: Two-dimensional ridgelet analysis. *Journal of Geophysical Research: Solid Earth*, 111(B7).
- Chui, C.K., 2016, *An introduction to wavelets*: Elsevier.
- Cohen, A. and Kovacevic, J., 1996, *Wavelets: The mathematical background*: Proceedings of the IEEE, 84(4), 514-522.
- Crone, J.D., 1986, Field examples of borehole Pulse EM surveys used to detect and outline Conductive ore deposits: in *Borehole Geophysics for Mining and Geotechnical Applications*, ed. PG. Killeen, Geological Survey of Canada, paper 85-27.
- Daniels, J.J. and Dyck, A.V., 1984, Borehole resistivity and electromagnetic methods applied to mineral exploration: *IEEE Transactions on Geoscience and Remote Sensing*, (1), 80-87.
- Daubechies, I., 1992. *Ten lectures on wavelets* (Vol. 61). Siam.
- Donoho, D. L., 1993, *Progress in Wavelet Analysis and WVD: A Ten Minute Tour*. *Progress in Wavelet Analysis and Applications* (Y. Meyer, and S. Roques, eds.). Gif-sur-Yvette: Editions Frontières.
- Donoho, D.L. and Johnstone, I.M., 1994, November. Threshold selection for wavelet shrinkage of noisy data. In *Engineering in Medicine and Biology Society, 1994. Engineering Advances: New Opportunities for Biomedical Engineers*. Proceedings of the 16th Annual International Conference of the IEEE (Vol. 1, pp. A24-A25). IEEE.
- Donoho, D.L. and Johnstone, I.M., 1995. Adapting to unknown smoothness via wavelet shrinkage. *Journal of the American Statistical Association*, 90(432), pp.1200-1224.
- Donoho, D.L., 1995. De-noising by soft-thresholding. *IEEE transactions on information theory*, 41(3), pp.613-627.
- Duncan, A., 2017. Advances in ground and borehole EM survey technology to 2017. In "Proceedings of exploration 17: sixth decennial international conference on mineral exploration", *Ground and borehole geophysics*, p. 169-182.

- Durak, L. and Arikan, O., 2003, Short-time Fourier transform: two fundamental properties and an optimal implementation. *IEEE Transactions on Signal Processing*, 51(5), 1231-1242.
- Dyck, A.V. and Young, R.P., 1985, Physical characterization of rock masses using borehole methods: *Geophysics*, 50(12), 2530-2541.
- Dyck, A.V., 1981, A method for quantitative interpretation of wideband, drill-hole EM surveys in mineral exploration: Doctoral dissertation, University of Toronto.
- Dyck, A.V., 1991, Drill-hole electromagnetic methods: in *Electromagnetic Methods in Applied Geophysics: Volume 2, Applications, Part B*. Society of Exploration Geophysicists, 881-930.
- Eadie, T. and Staltari, G., 1987, Introduction to downhole electromagnetic methods: *Exploration Geophysics*, 18(3), 247-254.
- Fargues, M.P., Barsanti, R.J., Hippenstiel, R. and Coutu, G., 1997, Wavelet-based denoising: comparisons between orthogonal and non-orthogonal decompositions. In *Circuits and Systems. Proceedings of the 40th Midwest Symposium on (Vol. 2, pp. 929-932)*. IEEE.
- Fedi, M., Primiceri, R., Quarta, T. and Villani, A.V., 2004. Joint application of continuous and discrete wavelet transform on gravity data to identify shallow and deep sources. *Geophysical Journal International*, 156(1), pp.7-21.
- Fedi, M.A.U.R.I.Z.I.O., Lenarduzzi, L.I.C.I.A., Primiceri, R.I.T.A. and Quarta, T.A.T.I.A.N.A., 2000. Localized denoising filtering using the wavelet transform. *Pure and Applied Geophysics*, 157(9), pp.1463-1491.
- Foufoula-Georgiou, E. and Kumar, P. eds., 2014. *Wavelets in geophysics (Vol. 4)*: Elsevier.
- Gabor, D., 1946, Theory of communication. Part 1: The analysis of information: *Journal of the Institution of Electrical Engineers*, 93(26), 429-441.
- Goodwin, D.A., 2008, Wavelet analysis of temporal data: Doctoral dissertation, University of Leeds.
- Gosselin, G., 2005, 2005 LaRonde Mineral Resource & Mineral Reserve Estimate Agnico-Eagle Mines Ltd. LaRonde Division : Technical report of Agnico Eagle Ltd..

- Hohmann, G.W., 1988. Electromagnetic methods in applied geophysics: Volume 1, Theory, edited by Misac N. Nabighian: Society of Exploration Geophysicists, Tulsa, Oklahoma.
- Ji, Y., Li, D., Yu, M., Wang, Y., Wu, Q. and Lin, J., 2016. A de-noising algorithm based on wavelet threshold-exponential adaptive window width-fitting for ground electrical source airborne transient electromagnetic signal. *Journal of Applied Geophysics*, 128, pp.1-7.
- Ji, Y., Li, D., Yuan, G., Lin, J., Du, S., Xie, L. and Wang, Y., 2016. Noise reduction of time domain electromagnetic data: Application of a combined wavelet denoising method. *Radio Science*, 51(6), pp.680-689.
- Joshi, S.S. and Hainalkar, V.N., 2016. A comparison of soft and hard thresholding by using discrete wavelet transforms. *International Research Journal of Multidisciplinary Studies*, 2(3).
- Josso, B., 2000, New wavelet based space-frequency analysis methods applied to the characterisation of 3-dimensional engineering surface textures: Doctoral dissertation, Liverpool John Moores University.
- Killeen, P.G. ed., 1986. Borehole geophysics for mining and geotechnical applications. Canadian Government Publishing Centre and Services Canada.
- King, A.R., 2016. Interpretation report on borehole TDEM survey. For Landore Resources Canada Inc.
- Kingman, J.E., Halverson, M. and Garner, S.J., 2004. Stacking of Controlled Source Electrical Geophysical Data.
- Kourouniotis, F.P., Kubichek, R.F., Boyd, N.G. and Majumdar, A.K., 1996, October. Application of the wavelet transform in seismic data processing for the development of new noise reduction techniques. In *Wavelet Applications in Signal and Image Processing IV* (Vol. 2825, pp. 620-632). International Society for Optics and Photonics.
- Kumar, P. and Fougoula-Georgiou, E., 1997. Wavelet analysis for geophysical applications. *Reviews of geophysics*, 35(4), pp.385-412.
- Lafrance, B., Davis, D.W., Goutier, J., Moorhead, J., Pilote, P., Mercier-Langevin, P., Dubé, B., Galley, A.G. and Mueller, W.U., 2005. Nouvelles datations isotopiques dans la portion québécoise du Groupe de Blake River et des unités adjacentes, Ministère des ressources naturelles et de la faune (Québec), report RP 2005-01.

- Lamontagne, Y. and Milkereit, B., 2007. Deep exploration with EM in boreholes. Exploration in the new millennium, pp.401-415.
- Larnier, H., Sailhac, P. and Chambodut, A., 2016. New application of wavelets in magnetotelluric data processing: reducing impedance bias. Earth, Planets and Space, 68(1), p.70.
- Lei, L., Wang, C. and Liu, X., 2013. Discrete wavelet transform decomposition level determination exploiting sparseness measurement. International Journal of Electrical, Computer, Energetic, Electronic and Communication Engineering, 7(9), pp.691-694.
- Li, H., Yi, T., Gu, M. and Huo, L., 2009. Evaluation of earthquake-induced structural damages by wavelet transform. Progress in Natural Science, 19(4), pp.461-470.
- Liu, C.L., 2010. A tutorial of the wavelet transform: NTUEE, Taiwan.
- Liu, W., Cao, S. and Chen, Y., 2016. Seismic Time-Frequency Analysis via Empirical Wavelet Transform. IEEE Geosci. Remote Sensing Lett., 13(1), pp.28-32.
- Macnae, J.C., Lamontagne, Y. and West, G.F., 1984. Noise processing techniques for time-domain EM systems. Geophysics, 49(7), pp.934-948.
- Mallat, S., 1999, A wavelet tour of signal processing: Elsevier.
- Mallat, S.G., 1989, A theory for multiresolution signal decomposition: the wavelet representation: IEEE transactions on pattern analysis and machine intelligence, 11(7), 674-693.
- Martelet, G., Sailhac, P., Moreau, F. and Diament, M., 2001. Characterization of geological boundaries using 1-D wavelet transform on gravity data: Theory and application to the Himalayas. Geophysics, 66(4), pp.1116-1129.
- Mercier-Langevin, P., Dubé, B., Hannington, M.D., Davis, D.W., Lafrance, B. and Gosselin, G., 2007. The LaRonde Penna Au-rich volcanogenic massive sulfide deposit, Abitibi greenstone belt, Quebec: Part I. Geology and geochronology. Economic Geology, 102(4), pp.585-609.
- Mercier-Langevin, P., Dubé, B., Hannington, M.D., Richer-Laflèche, M. and Gosselin, G., 2007. The LaRonde Penna Au-rich volcanogenic massive sulfide deposit, Abitibi Greenstone Belt, Quebec: part II. litho geochemistry and paleotectonic setting. Economic Geology, 102(4), pp.611-631.

- Meyer, Y., 1993, Wavelets-algorithms and applications. Wavelets-Algorithms and applications Society for Industrial and Applied Mathematics Translation.
- Miao, X.G. and Moon, W.M., 1999. Application of wavelet transform in reflection seismic data analysis. *Geosciences Journal*, 3(3), pp.171-179.
- Michael, W., 2007. Digital signal processing using MATLAB and wavelets. Infinity.
- Misiti, M., Misiti, Y., Oppenheim, G. and Poggi, J.M., 2005, Wavelet Toolbox for Use with {MATLAB}.
- Moen, H., 2007. Wavelet transforms and efficient implementation on the GPU, Master's thesis: University of Oslo.
- Moreau, F., Gibert, D., Holschneider, M. and Saracco, G., 1999. Identification of sources of potential fields with the continuous wavelet transform: Basic theory. *Journal of Geophysical Research: Solid Earth*, 104(B3), pp.5003-5013.
- Muszala, S., Stoffa, P.L. and Lawver, L.A., 2001. An application for removing cultural noise from aeromagnetic data. *Geophysics*, 66(1), pp.213-219.
- Nabighian, M.N. and Macnae, J.C., 1991. Time domain electromagnetic prospecting methods. *Electromagnetic methods in applied geophysics*, 2(part A), pp.427-509.
- Nagendra, H., Mukherjee, S. and Kumar, V., 2013. Wavelet based nonlinear thresholding techniques for pre-processing ECG signals. *International Journal of Biomedical and Advance Research*, 4(8), pp.534-544.
- Nenna, V. and Pidlisecky, A., 2013. The use of wavelet transforms for improved interpretation of airborne transient electromagnetic data. *Geophysics*, 78(3), pp.E117-E123.
- Oldenburg, D.W., Levy, S. and Whittall, K.P., 1981, Wavelet estimation and deconvolution: *Geophysics*, 46(11), 1528-1542.
- Percival, D.B. and Walden, A.T., 2006. Wavelet methods for time series analysis (Vol. 4). Cambridge university press.
- Pinsky, M.A., 2008. Introduction to Fourier analysis and wavelets (Vol. 102). American Mathematical Soc..

- Polzer, B., 2000. The role of borehole EM in the discovery and definition of the Kelly Lake Ni-Cu deposit, Sudbury, Canada. In SEG Technical Program Expanded Abstracts 2000 (pp. 1063-1066). Society of Exploration Geophysicists.
- Rabeau, O., Legault, M., Cheilletz, A., Jébrak, M., Royer, J.J. and Cheng, L.Z., 2010. Gold potential of a hidden Archean fault zone: the case of the Cadillac–Larder Lake Fault. *Exploration and Mining Geology*, 19(3-4), pp.99-116.
- Raiche, A., Sugeng, F. and Wilson, G., 2007. Practical 3D EM inversion, The P223F software suite. *ASEG Extended Abstracts*, 2007(1), pp.1-5.
- Ravier, P. and Amblard, P.O., 2001. Wavelet packets and de-noising based on higher-order-statistics for transient detection. *Signal processing*, 81(9), pp.1909-1926.
- Ridsdill-Smith, T.A. and Dentith, M.C., 1999. The wavelet transform in aeromagnetic processing. *Geophysics*, 64(4), pp.1003-1013.
- Rückemann, C.P., 2012, January. Comparison of stacking methods regarding processing and computing of geoscientific depth data. In *Proc. Fourth International Conference on Advanced Geographic Information Systems, Applications, and Services (GEOProcessing 2012)*, Vol. 30, pp. 35-40.
- Sadowsky, J., 1996. Investigation of signal characteristics using the continuous wavelet transform. *Johns Hopkins apl technical digest*, 17(3), pp.258-269.
- Sailhac, P. and Gibert, D., 2003. Identification of sources of potential fields with the continuous wavelet transform: Two-dimensional wavelets and multipolar approximations. *Journal of Geophysical Research: Solid Earth*, 108(B5).
- Sailhac, P., Galdeano, A., Gibert, D., Moreau, F. and Delor, C., 2000. Identification of sources of potential fields with the continuous wavelet transform: Complex wavelets and application to aeromagnetic profiles in French Guiana. *Journal of Geophysical Research: Solid Earth*, 105(B8), pp.19455-19475.
- Shukla, P.D., 2003, Complex wavelet transforms and their applications: Master of Philosophy (M. Phil.) report, University of Strathclyde Glasgow, Scotland.
- Singh, A. and Singh, U.K., 2017. Continuous wavelet transform and Euler deconvolution method and their application to magnetic field data of Jharia coalfield, India. *Geoscientific Instrumentation, Methods and Data Systems*, 6(1), p.53.

- Sinha, S., Routh, P.S., Anno, P.D. and Castagna, J.P., 2005. Spectral decomposition of seismic data with continuous-wavelet transform. *Geophysics*, 70(6), pp.P19-P25.
- Spies, B.R. and Greaves, R.J., 1991. Numerical modeling of surface-to-borehole electromagnetic surveys for monitoring thermal enhanced oil recovery. *Geoexploration*, 28(3-4), pp.293-311.
- Spies, B.R., 1996. Electrical and electromagnetic borehole measurements: A review. *Surveys in Geophysics*, 17(4), pp.517-556.
- Tao, R., Li, Y.L. and Wang, Y., 2010, Short-time fractional Fourier transform and its applications. *IEEE Transactions on Signal Processing*, 58(5), 2568-2580.
- Tseng, H.W., Becker, A., Wilt, M.J. and Deszcz-Pan, M., 1998. A borehole-to-surface electromagnetic survey. *Geophysics*, 63(5), pp.1565-1572.
- Wang, Y., Ji, Y., Li, S., Lin, J., Zhou, F. and Yang, G., 2013. A wavelet-based baseline drift correction method for grounded electrical source airborne transient electromagnetic signals. *Exploration Geophysics*, 44(4), pp.229-237.

Figure 2.6 is an example showing a signal is decomposed to level 3 with the DWT, which we can summarize as below.

- a) Detail coefficients (cD_i) store high-frequency features of the signal; and approximation coefficients (cA_i) show low-frequency components of the signal.
- b) Higher decomposition level means larger scale value; features extracted from the signal or the approximation coefficients of the previous level to the detail coefficients have lower frequencies, and vice-versa.

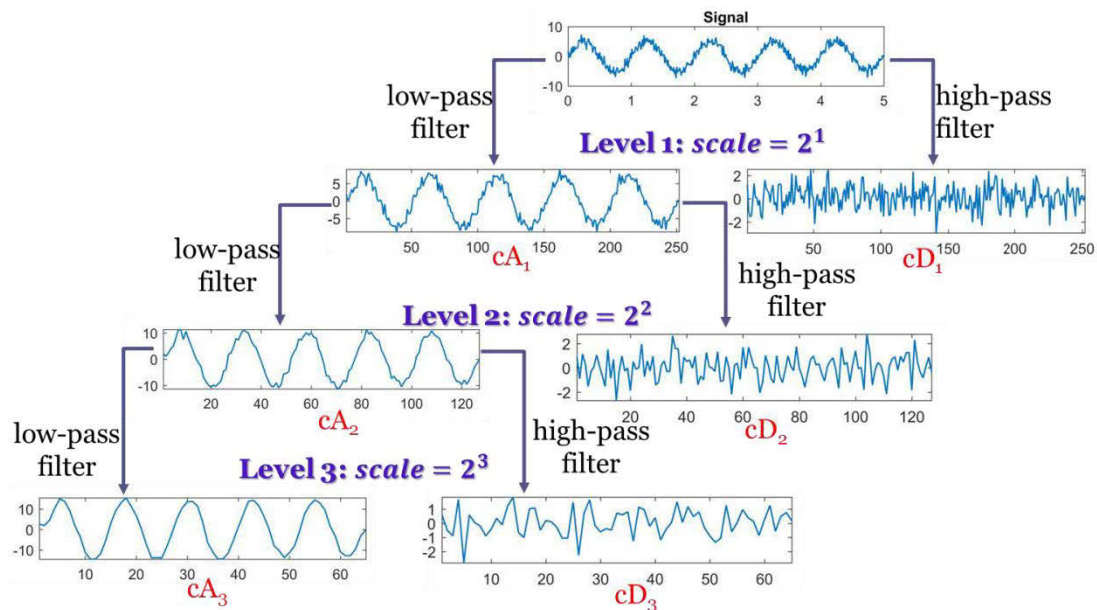


Figure 2.6 A signal is decomposed to level 3 with the DWT.

2.1.3 Selection of a wavelet

There is a number of wavelet families, such as Haar, Daubechies, Symlets, Coiflets, Biorthogonal, Meyer, Gaussian, Mexican hat, Morlet, Shannon, Frequency B-Spline, Complex Morlet and Fejer-Korovkin wavelets (see wavlet Toolbox of MATLAB). Users have to decide first which wavelet is suitable for their application: CWT or DWT. If the goal of the application is to perform a detailed time-frequency analysis,

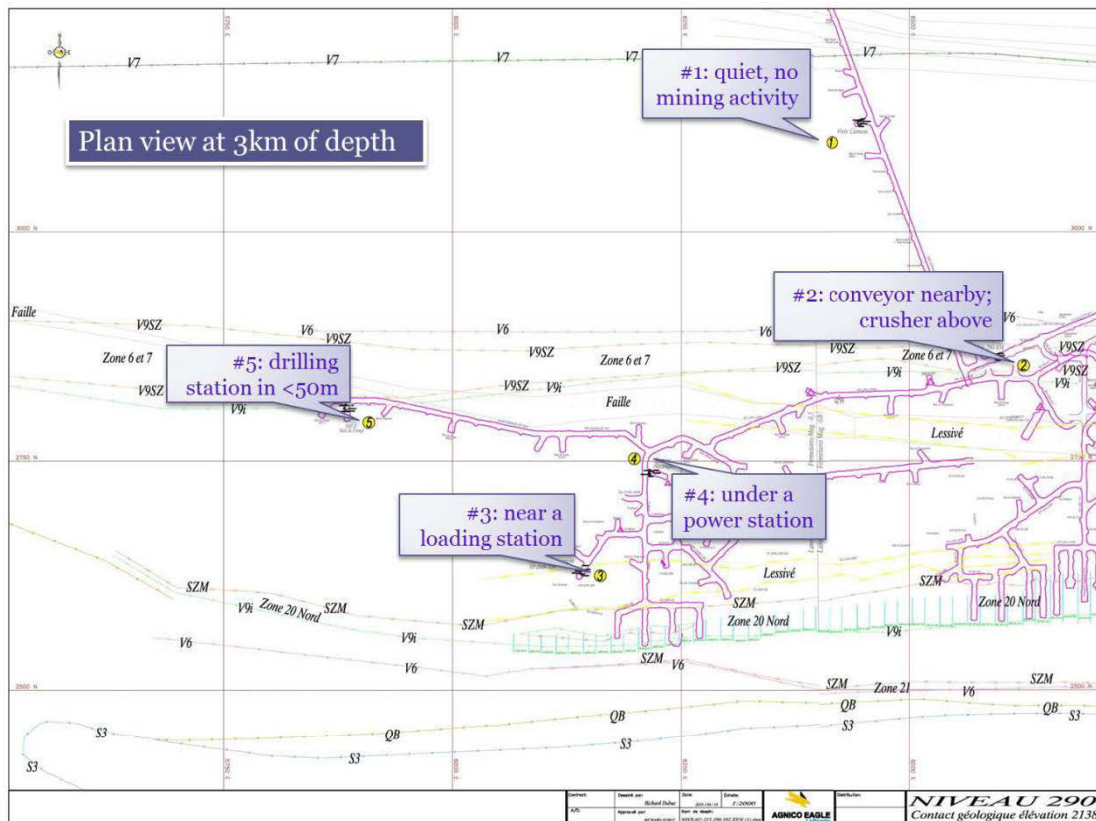


Figure 3.4 Locations of the five data acquisition sites (scale: 1:2000).

3.4.3 Recorded signals

There are 6.11 gigabytes electromagnetic data recorded during more than 22 hours. For better associating changes in the EM signals with underground mining activities, the operation period of mining equipment (drilling, crusher, and conveyor etc.) is considered. Operation hours for the drilling site that is near the data acquisition site #5 are from 08:00:00 to 15:00:00 on April 12, 2018, and from 20:00:00 on April 12, 2018 to 03:00:00 on April 13, 2018. In addition, Figure 3.5 tells the electrical current variations in the conveyor near the data acquisition site #2. All data acquisition sites were blocked for the measurement, therefore no traffic presented at all sites during the period of recording. Two blasting events took place between 17:43:28.992 and 17:43:37.661, 05:19:24.873 and 05:19:34.437. The first blast happened near 380 m above site #2, while the 2nd is 50 m in the East-North of site #2. However, we do not

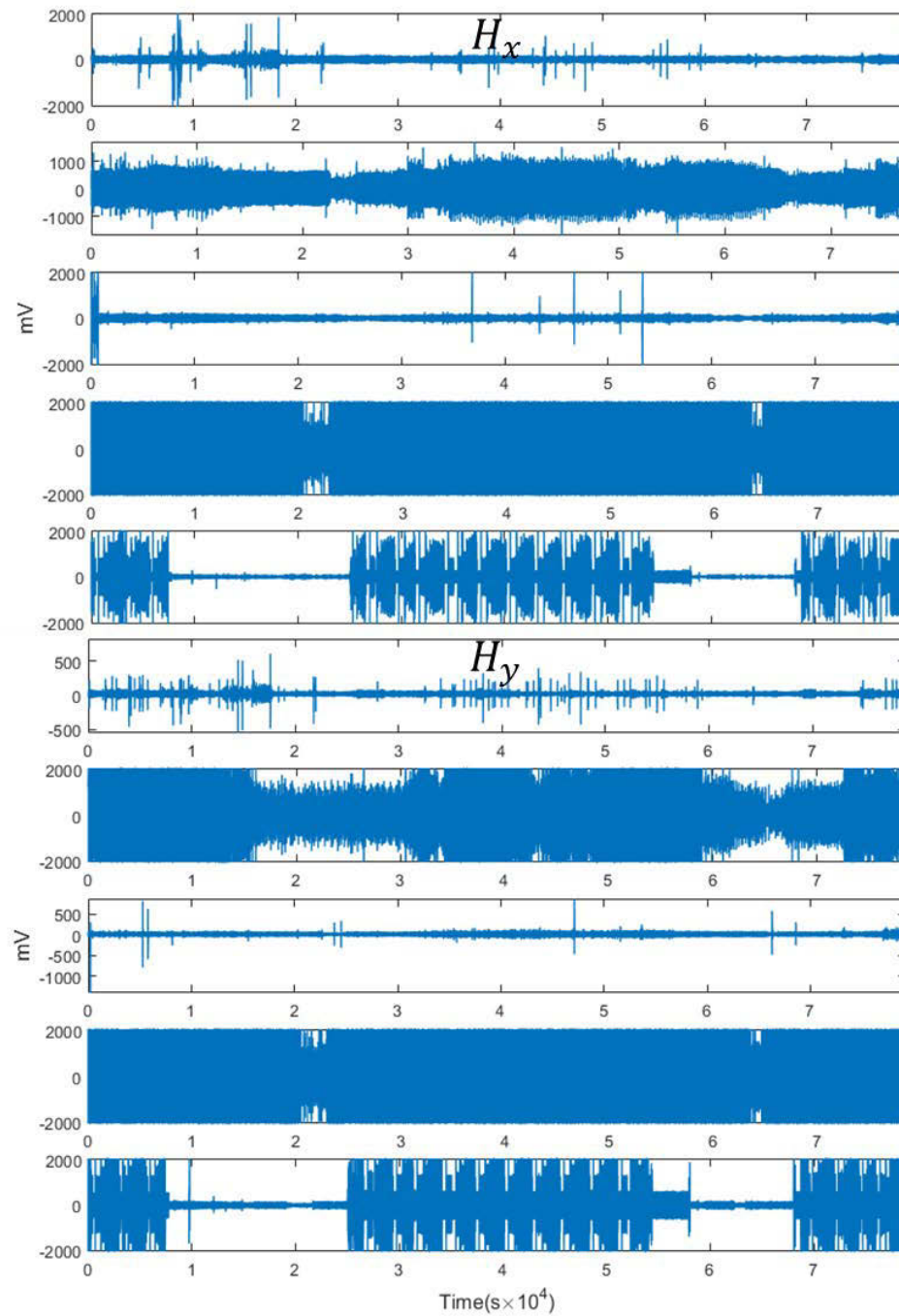


Figure 3. 7 Magnetic components (H_x and H_y) from five acquisition sites. From top to bottom: site #1, site #2, site #3, site #4, and site #5.

is impossible to guess the cause of this difference without witness. The 60 Hz signal is highlighted in both fields.

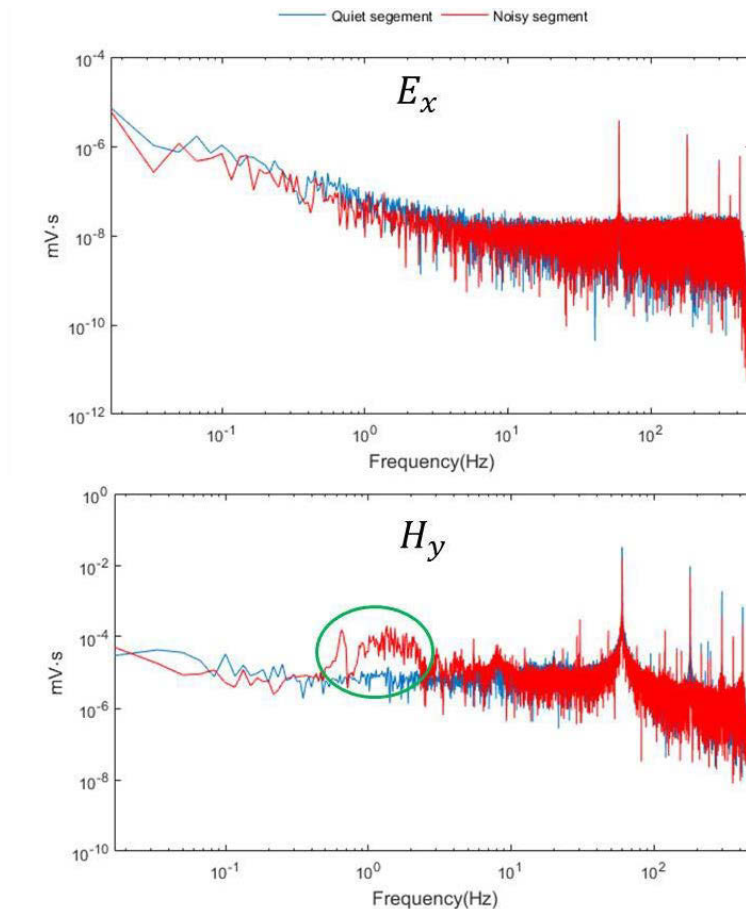


Figure 3.8 FT results of the two segments of the electric field component E_x and the magnetic component H_y at site #1.

Results of acquisition site #2: This site is near to a conveyor; and there is a crusher above. The noise level at this site should be affected by the operating status of the mining machine.

For the electric component E_x , we can see, in Figure 3.9, no matter the machine is operating or not the 60 Hz peak presents. This is understandable, because there is always alternative current of 60 Hz in the power lines no matter the machine is

operating or not. But when the machine is operating, in the spectrum segment of data corresponding to the time when the machine is operating, we observed another peak at around 7 Hz, indicated by the black arrow. And again, the spectra of both segments decrease with frequency. Again, the spectra decrease linear with frequency.

For the magnetic field component, we have not observed apparent difference between the spectra of these two segments of data. But the spectrum amplitude of the noisy segment is slightly bigger than that of the quiet segment. And the 60 Hz peak is detected in both segments.

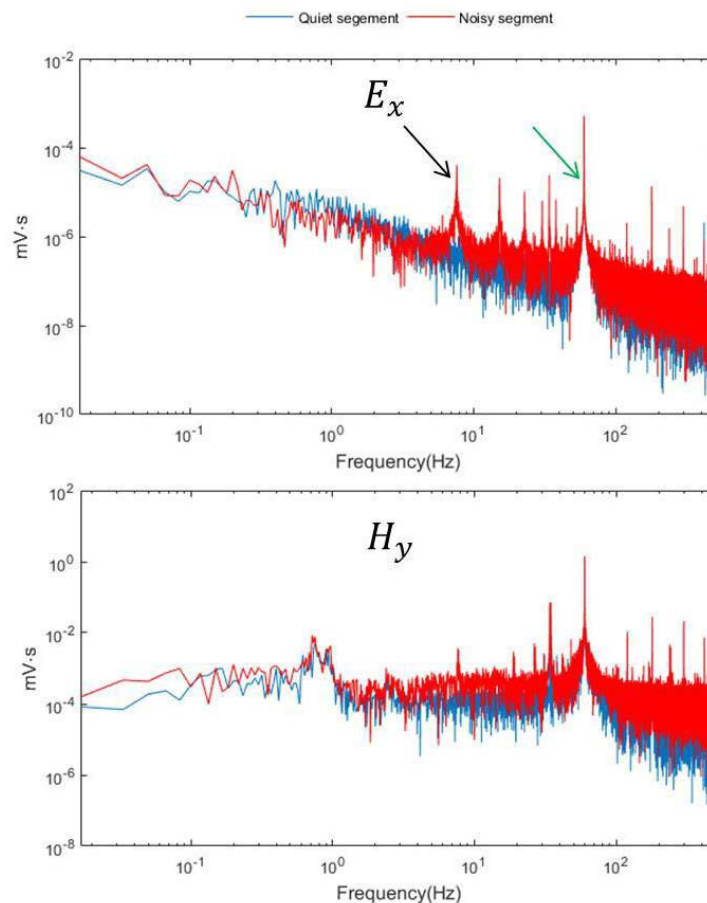


Figure 3.9 FT results of the two segments of the electric field component E_x and the magnetic component H_y at site #2.

Results of acquisition site #3: The environment situation of site #3 is similar to that of the site #1. The 60 Hz peak is detected in both segments of both E_x and H_y (Figure 3.10). The other apparent feature in H_y is the amplitude of the noisy segment is clearly bigger than that of the quiet segment.

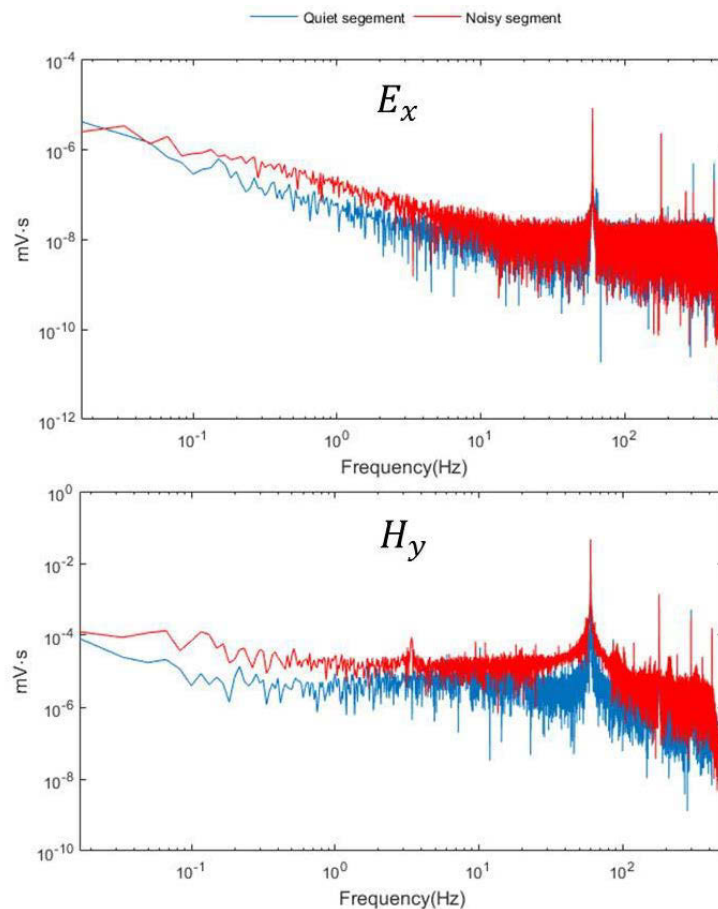


Figure 3.10 FT results of the two segments of the electric field component E_x and the magnetic component H_y at site #3.

The acquisition site #4 is the noisiest site of the five acquisition sites. There is not only a peak at 60 Hz, its amplitude is larger than other sites. Although the power station above the acquisition site is always working, there are differences between the two segments of signal. We speculate that the difference is caused by the change of

the output power of the station. When there is no mining related activity, the mining apparatuses are shutdown; as a result the output power of the station is lower; on the contrary, the mining apparatuses are operating; consequently, the output power of the station is higher. The reason of the abrupt change around 4 Hz in the FT result of the magnetic component H_y of the noisy segment in Figure 3.11 is not clear yet. Neither can any rational speculation be made here.

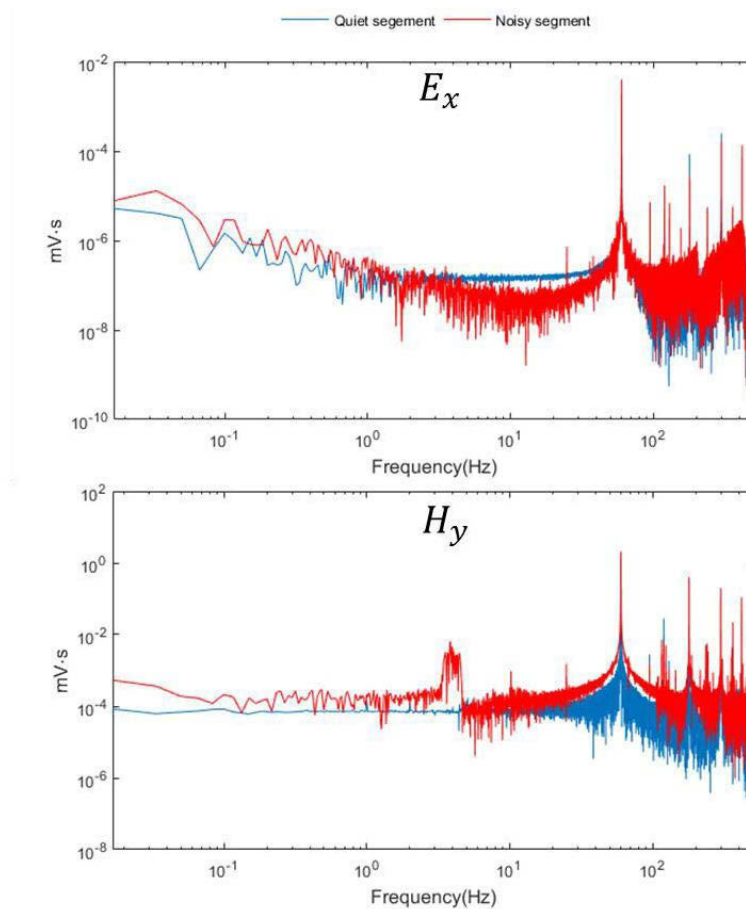


Figure 3.11 FT results of the two segments of the electric field component E_x and the magnetic component H_y at site #4.

For the results of acquisition site #5, the electric field component E_x is very similar to the site #3. We can see that the amplitude of the spectrum of the segment (red line),

which represents the period where the drilling site is operating, is slightly higher than that of the other segment (blue line). While, for the magnetic field component H_y , there are some distinctive features: for frequency range from DC (0 Hz) to 3 Hz, the FT result of the quiet segment has higher amplitude; when frequency is higher than 3 Hz, the FT result of the noisy segment has higher amplitude. This may imply the magnetic field component is more vulnerable to drilling activities.

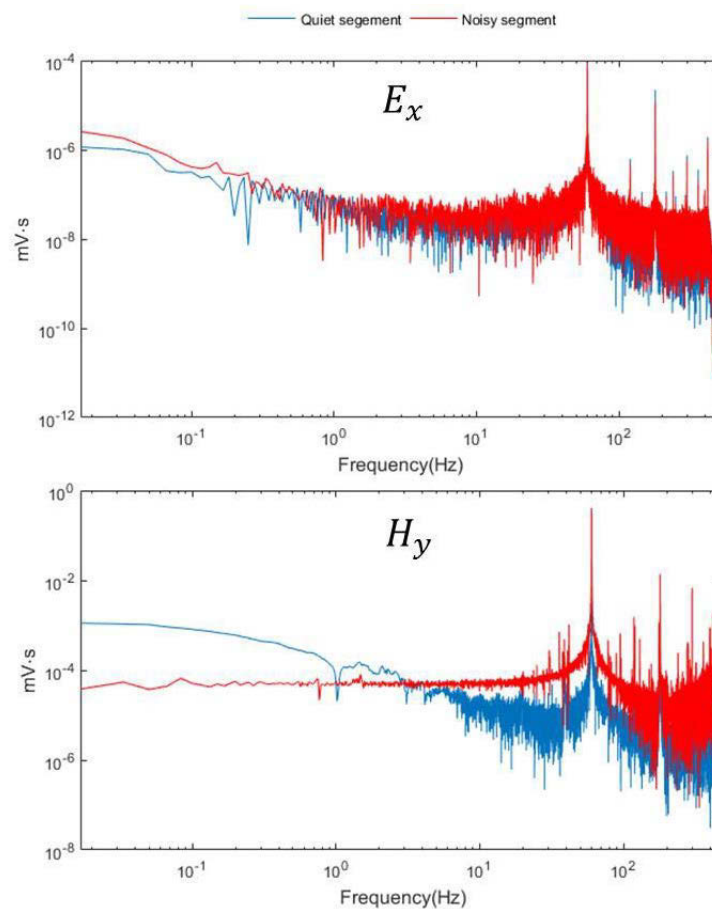


Figure 3.12 FT results of the two segments of the electric field component E_x and the magnetic component H_y at site #5.

Due to the fact that the sampling rate of ZEN is 1024, the highest frequency can be recorded in our survey is 512 Hz, therefore, high frequency noises come from

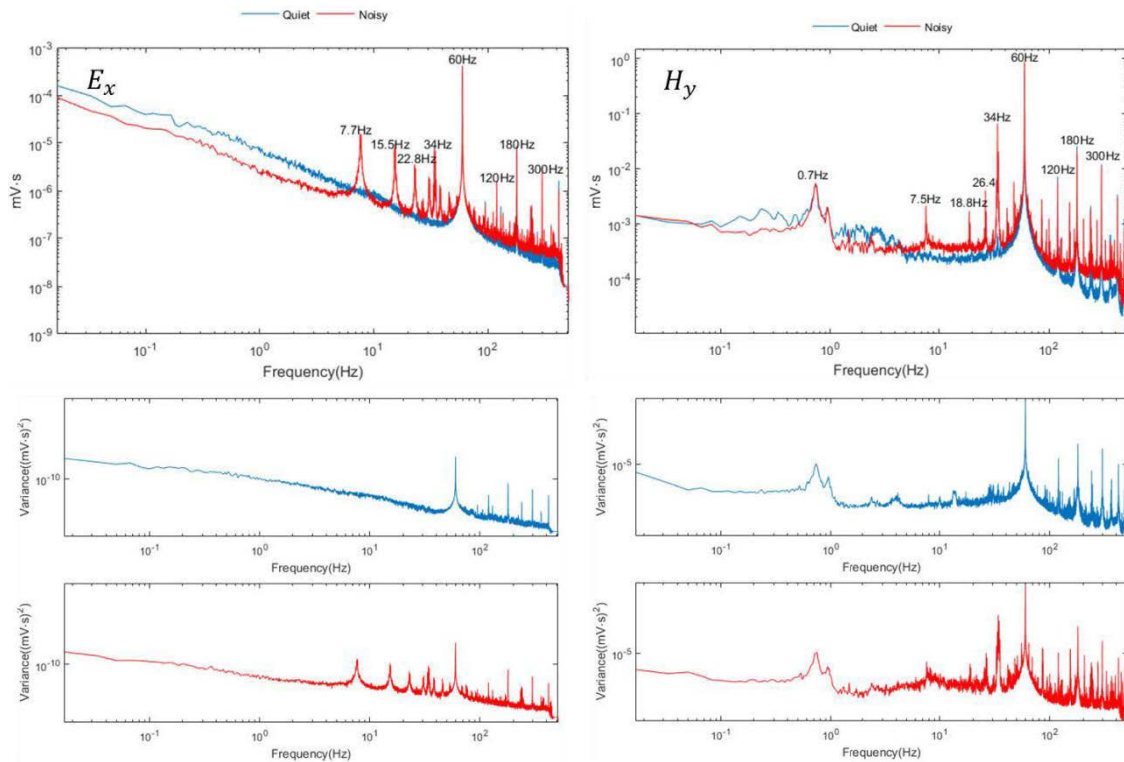


Figure 3.13 Average spectra and variance of the electric field component E_x (left column) and the magnetic component H_y (right column) at site #2 (blue line is the average spectrum of segments from quiet period of time; red line is the average spectrum of segments from quiet period of time).

3.6.2 Analysis with the CWT

We have chosen the CWT to analyze the two segments for its ability to do time-frequency analysis. In this section we choose the Morlet wavelet, which is a symmetry wavelet formed by multiplying an exponential with a Gaussian window.

Figure 3.14 shows the time-frequency representations of the two segments of electric field component E_x and magnetic field component H_y from site #1. In the frequency (vertical axis) and time (horizontal axis) systems, it clearly indicates when a signal at a certain frequency appears. For the electric field component E_x , only the event of 0.01 Hz has been observed in both segments. However, more events can be found in the CWT results of the two segments of H_y . For the quiet segment, there are three

The acquisition site #5 is located near a drilling site. For E_x , events are observed at 0.01 Hz, 0.03 Hz, and 60 Hz in both segments; but for H_y , only the 60 Hz event is presented. Energy of events observed in noisy segment is higher than those observed in the quiet segment.

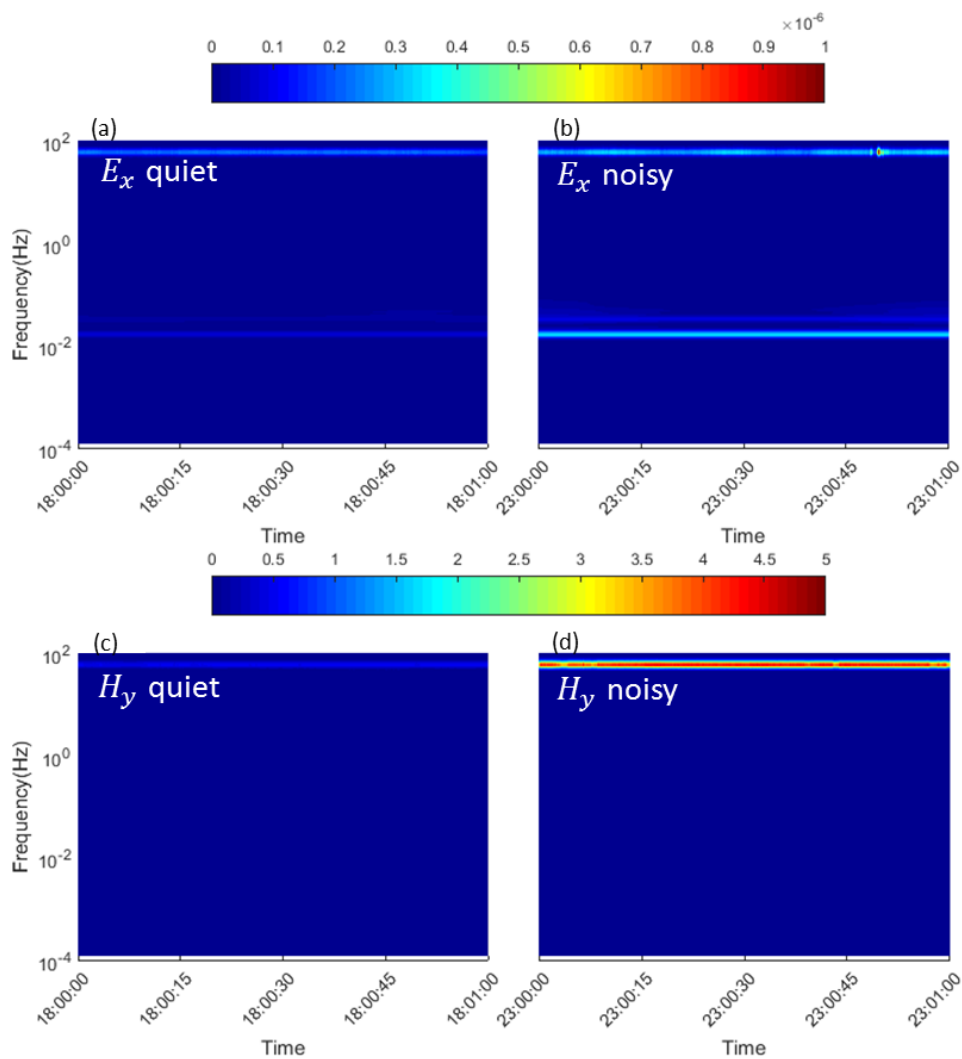


Figure 3.18 Time-frequency representation of the two segments of the electric field component E_x and the magnetic component H_y from site #5.

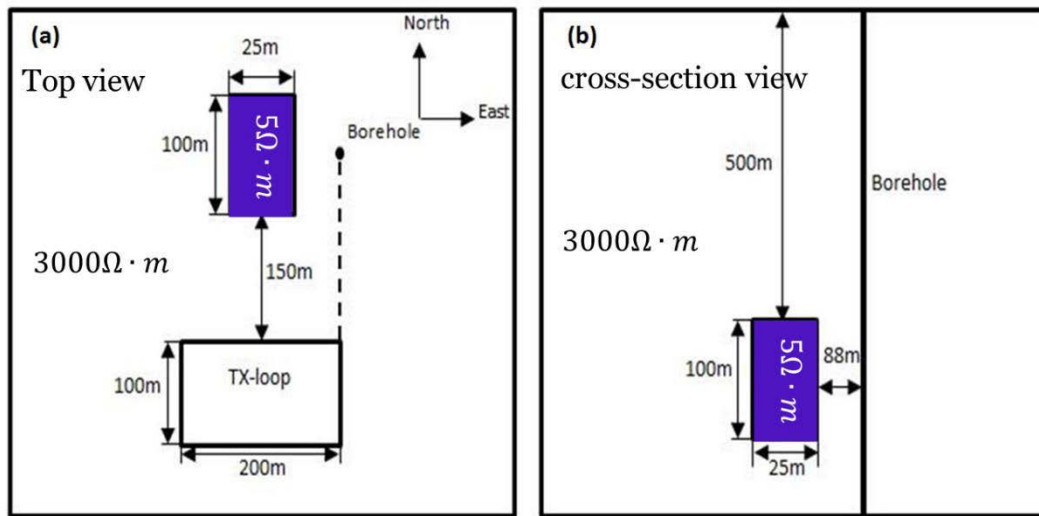


Figure 4.3 The 3D model used to generate synthetic data.

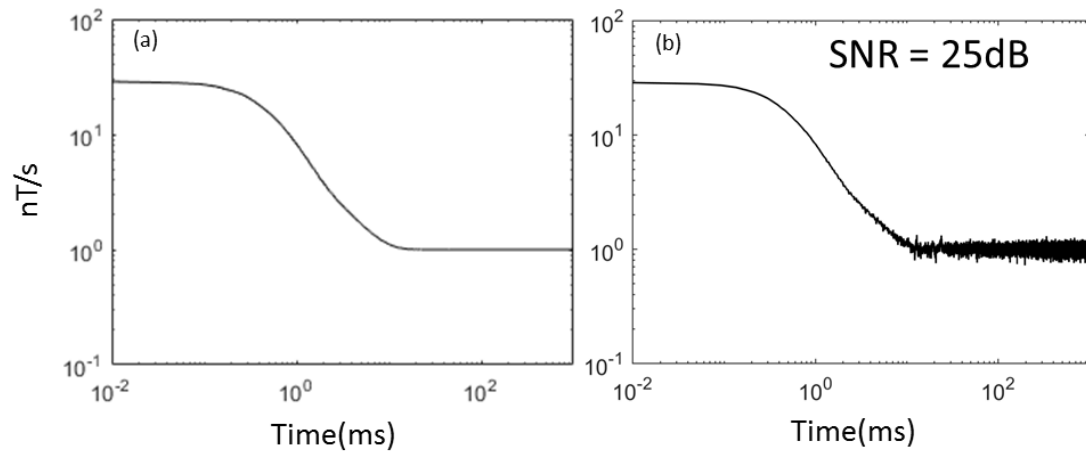


Figure 4.4 The BHEM noise-free signal (a) generated by Loki from the model in Figure 4.3 and the corresponding noisy signal (b).

noise to a satisfactory level (Figure 4.7 and Figure 4.8), especially for later time channels. There is a visible perturbation remained in processed data after the DWT. These noise residuals may affect the interpretation accuracy in future works. We therefore use the curve fitting technique (CFT) as a complementary method in dealing with the post-processing of simple data sets. Details of under what circumstances the curve fitting technique is used are explained in section 2.2.1.

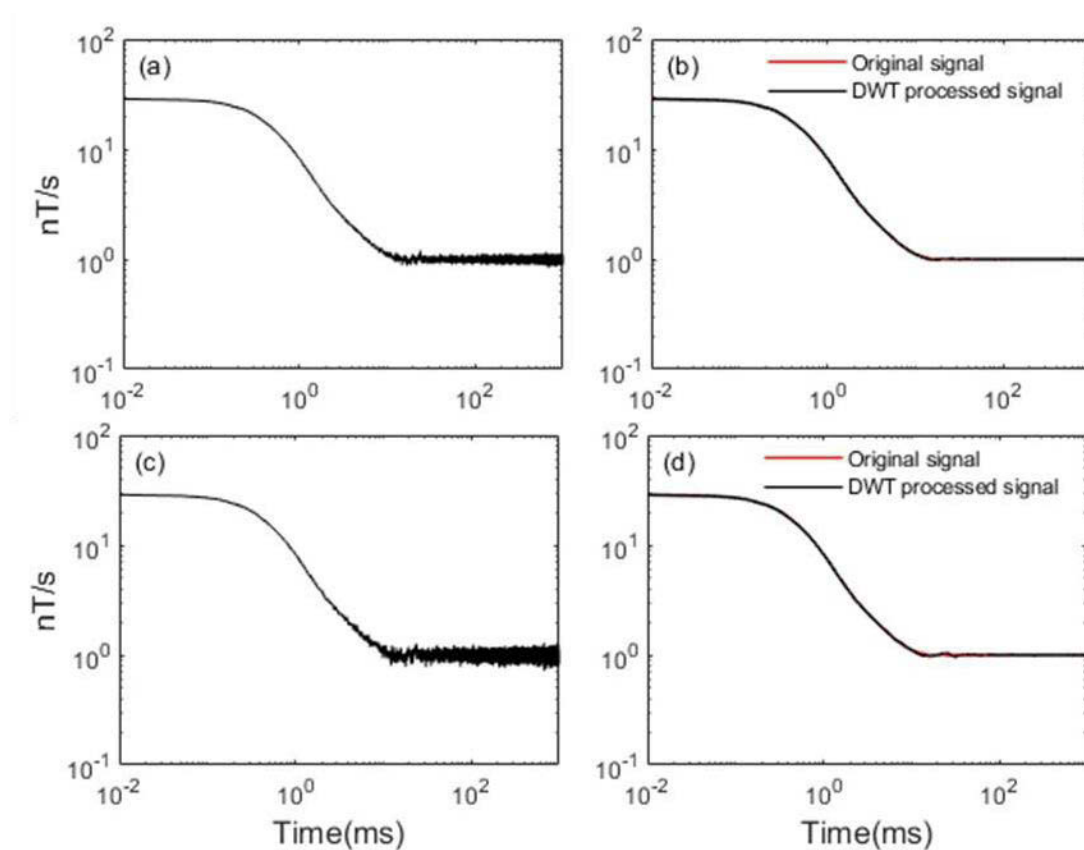


Figure 4.6 The synthetic noisy signals (a) and (c) at different noise level, the SNR after the DWT is increased from 30 dB to 52 dB (b), and from 25 dB to 47 dB (d), respectively.

APPENDIX I

RESULTS OF CHANNEL 2 (EY) AND CHANNEL 3 (HX)

I.1 Results of acquisition site #1

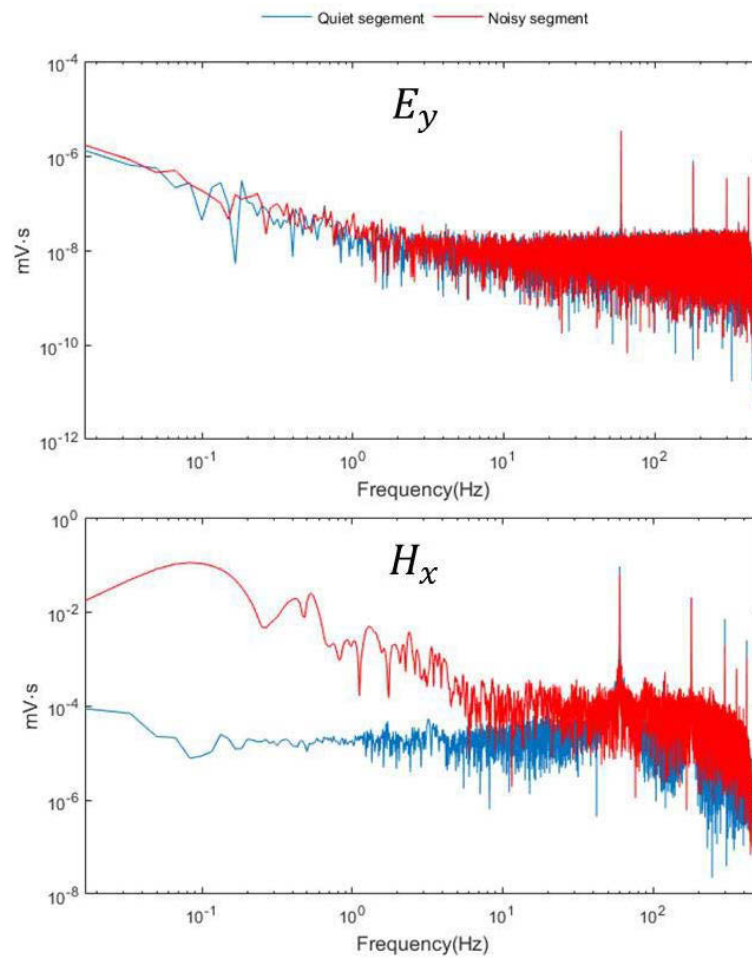


Figure I.1 FT results of the two segments of the electric field component E_y and the magnetic component H_x at site #1.

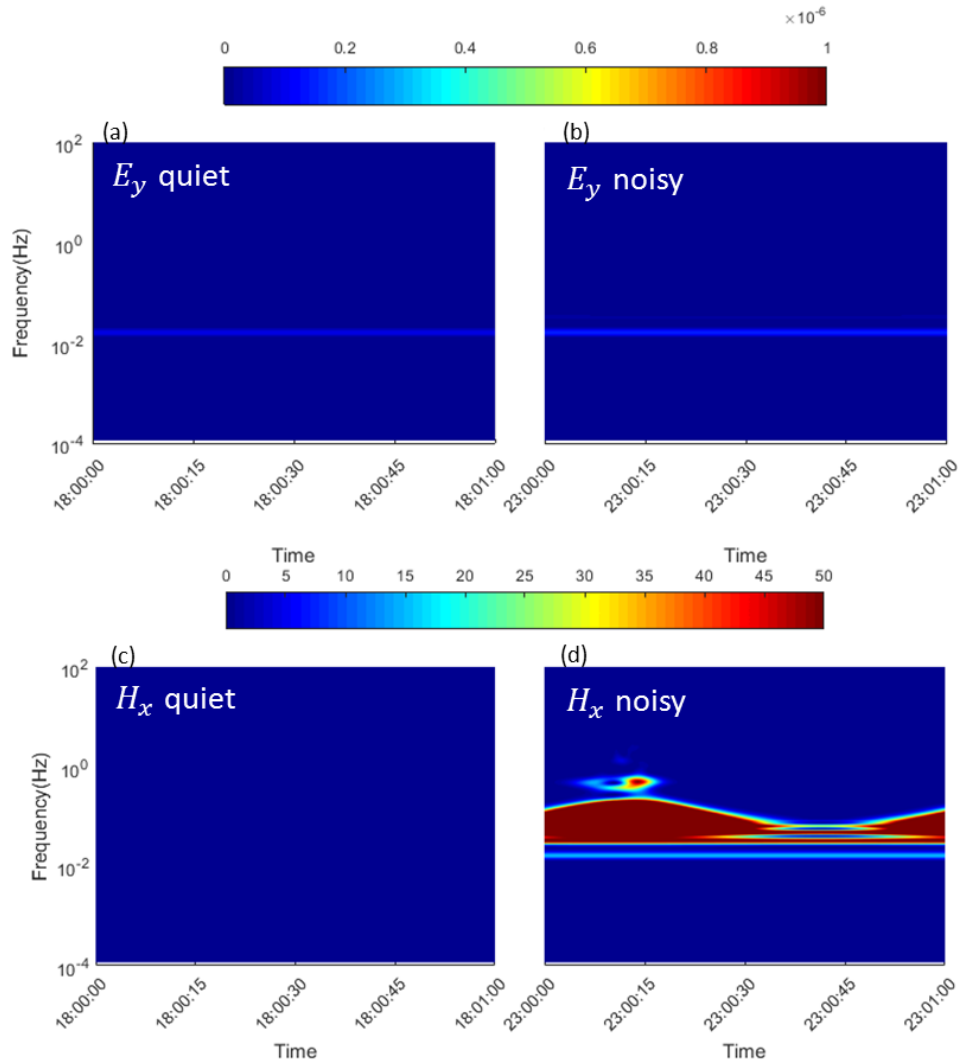


Figure I.2 Time-frequency representation of the two segments of the electric field component E_y and the magnetic component H_x from site #1.

I.2 Results of acquisition site #2

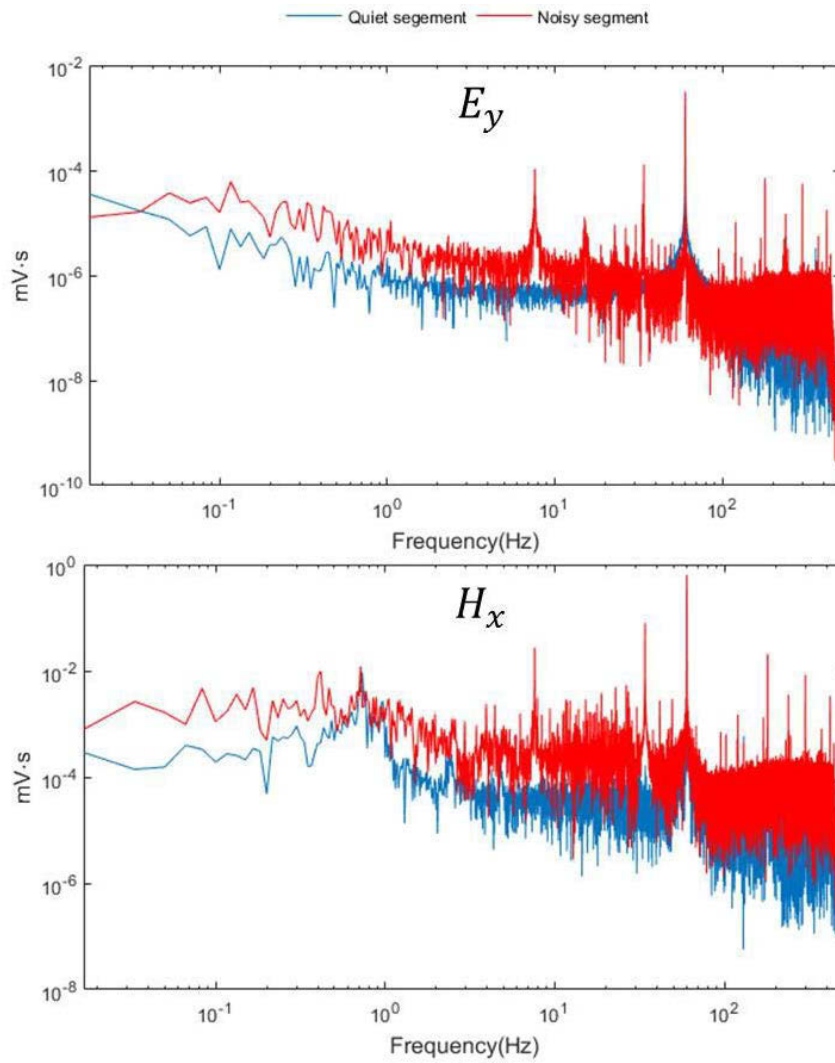


Figure I.3 FT results of the two segments of the electric field component E_y and the magnetic component H_x at site #2.

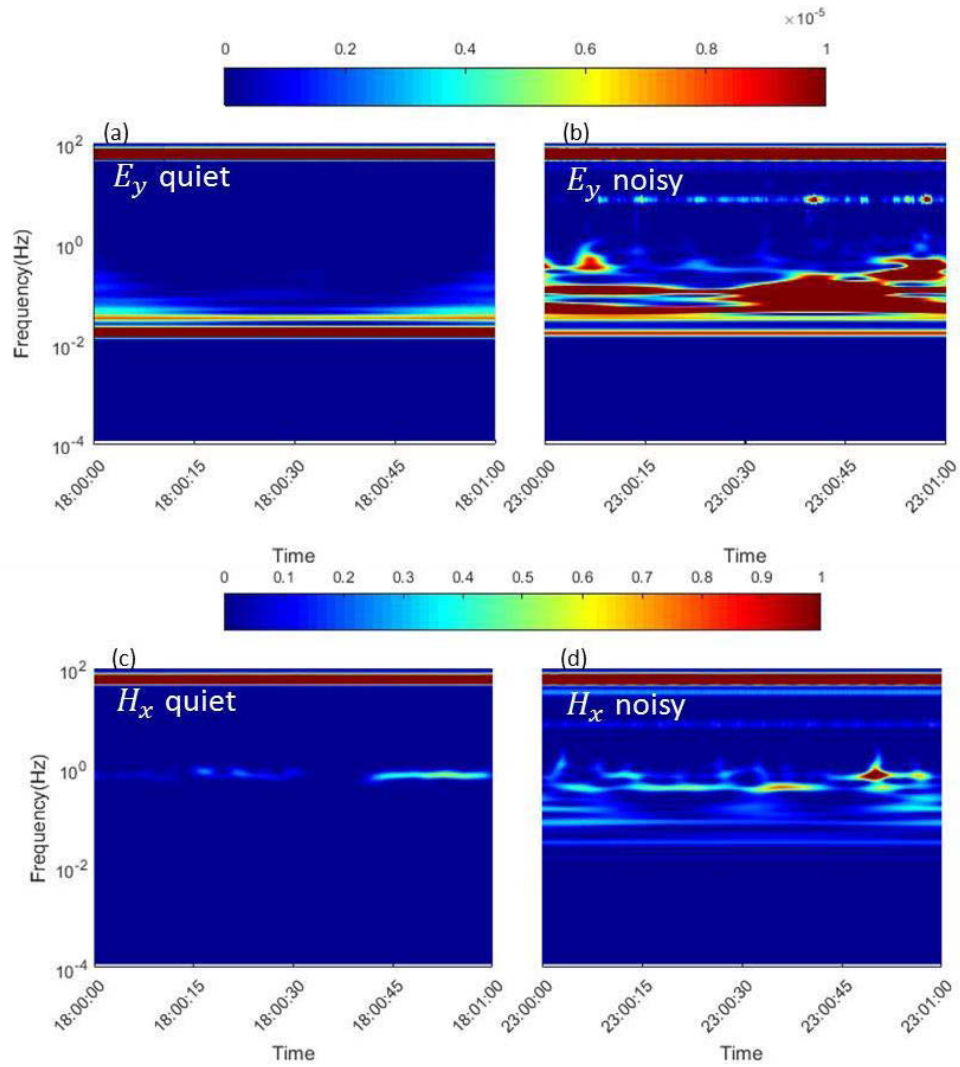


Figure I.4 Time-frequency representation of the two segments of the electric field component E_y and the magnetic component H_x from site #2.

I.3 Results of acquisition site #3

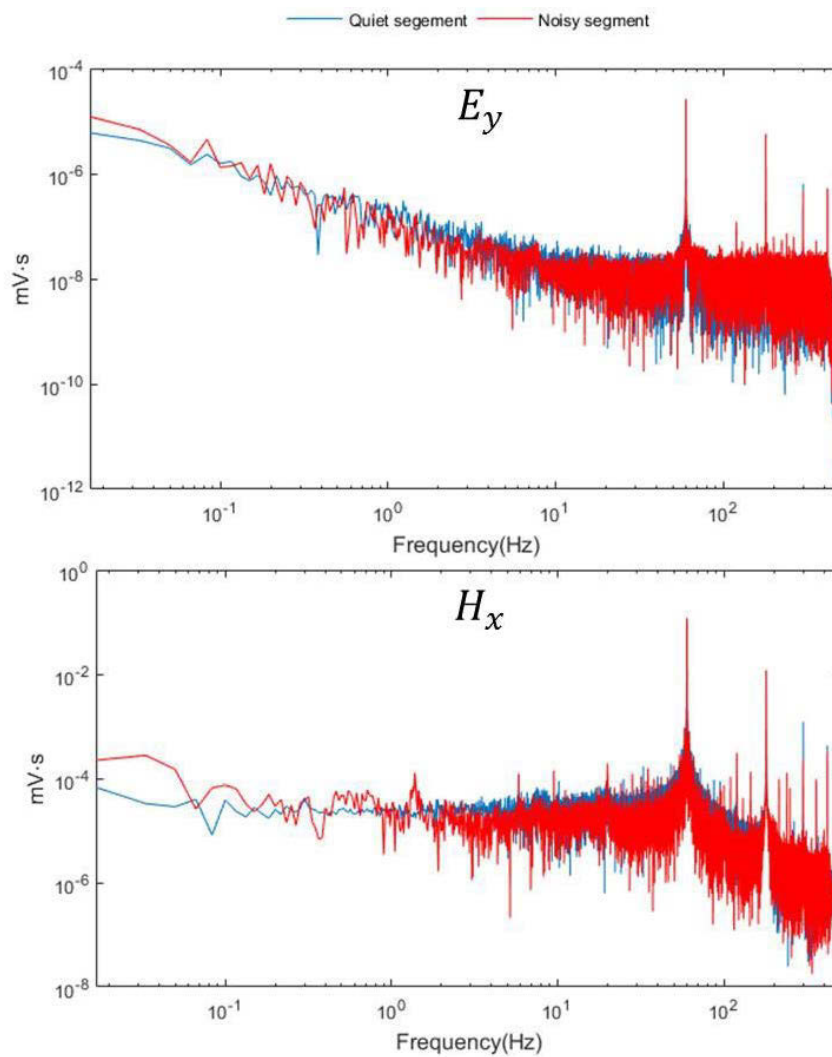


Figure I.5 FT results of the two segments of the electric field component E_y and the magnetic component H_x at site #3.

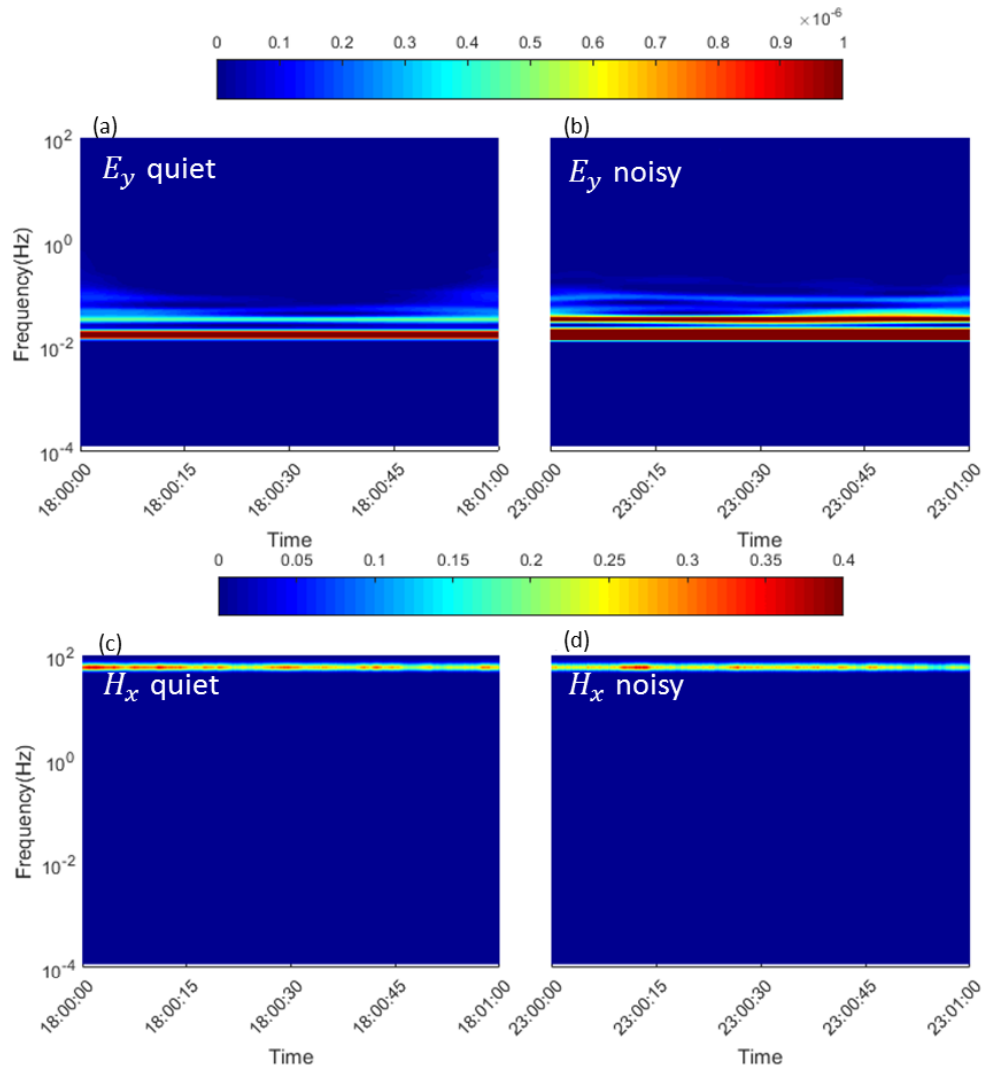


Figure I.6 Time-frequency representation of the two segments of the electric field component E_y and the magnetic component H_x from site #3.

I.4 Results of acquisition site #4

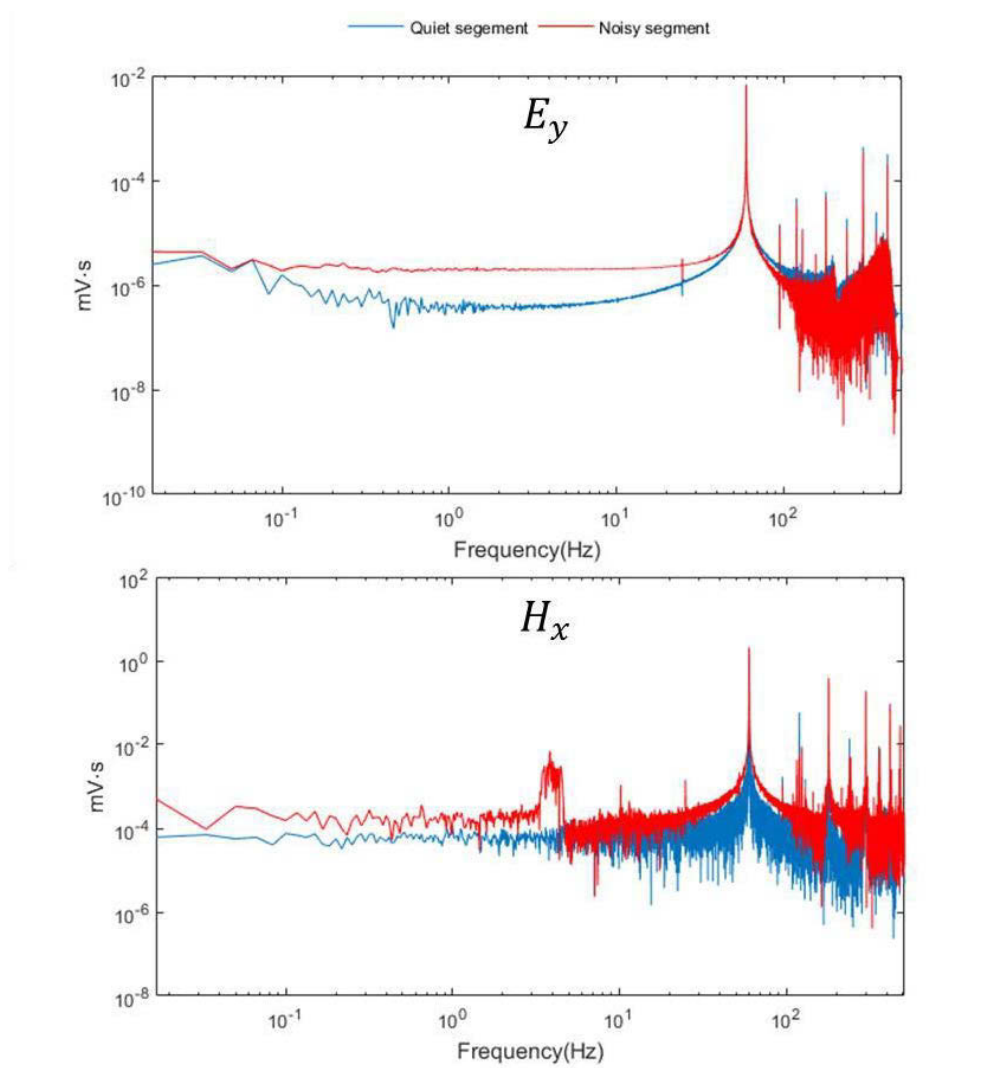


Figure I.7 FT results of the two segments of the electric field component E_y and the magnetic component H_x at site #4.

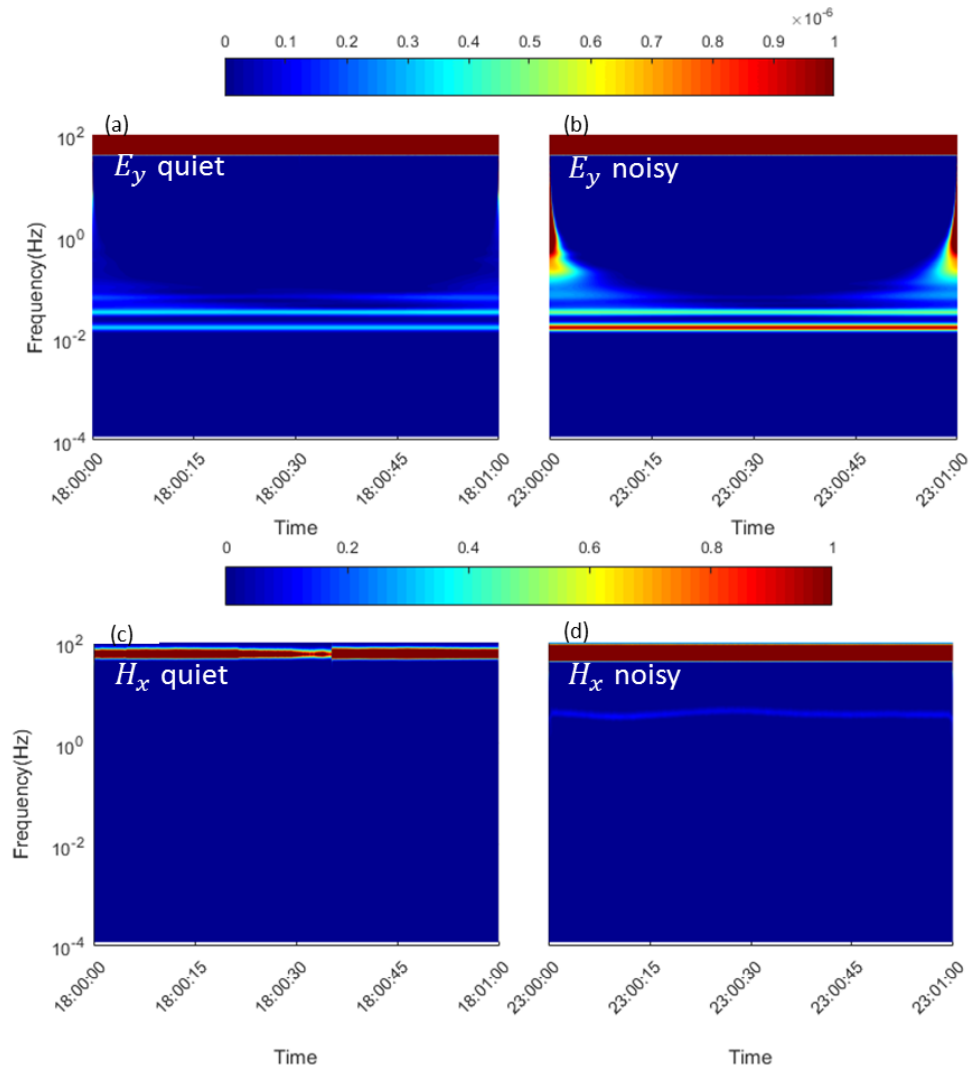


Figure I.8 Time-frequency representation of the two segments of the electric field component E_y and the magnetic component H_x from site #4.

I.5 Results of acquisition site #5

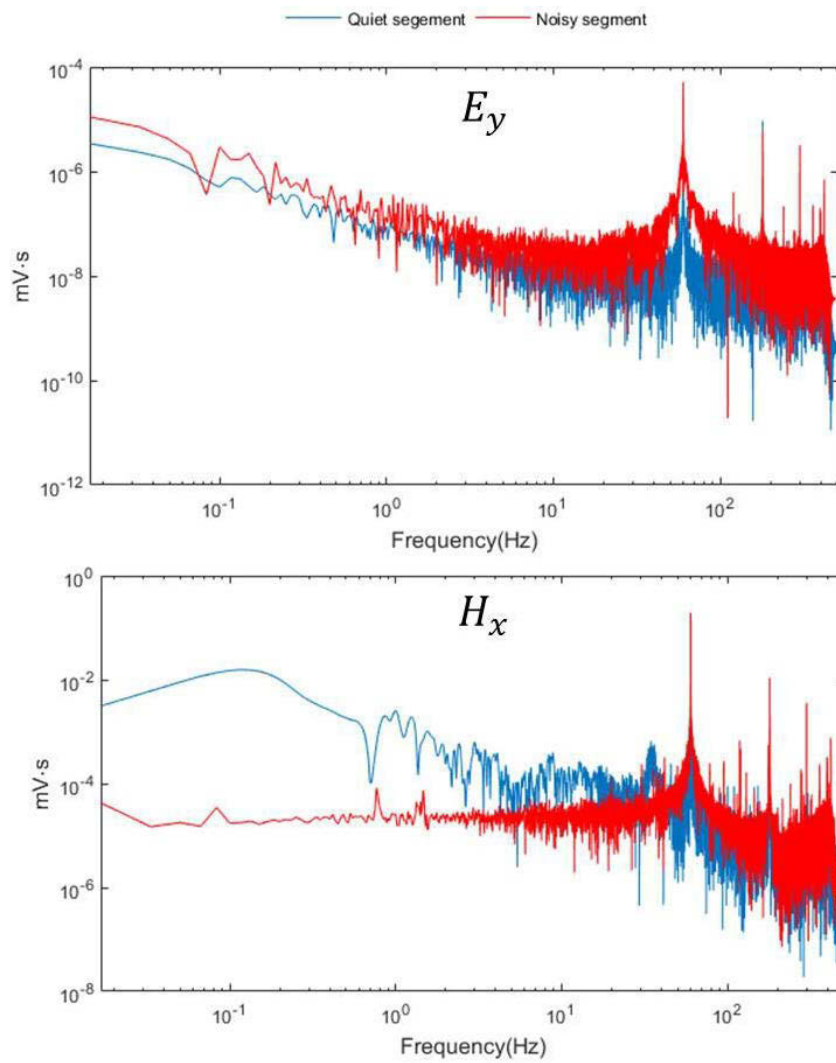


Figure I.9 FT results of the two segments of the electric field component E_y and the magnetic component H_x at site #5.